CHALMERS
UNIVERSITY OF TECHNOLOGY

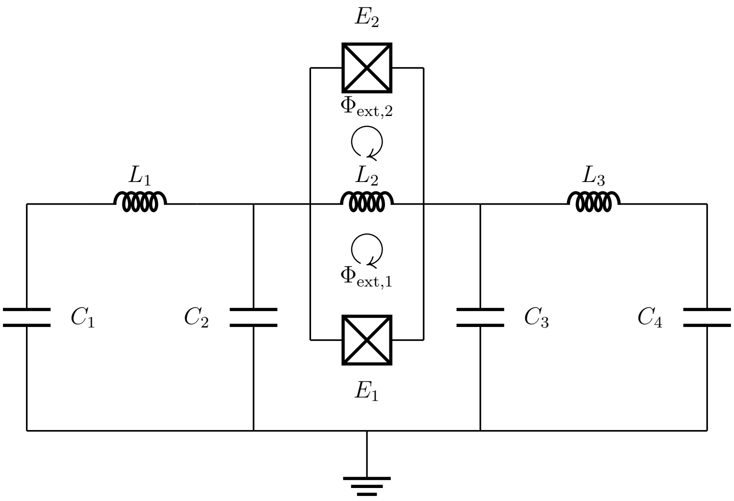

Toward Stabilization of the Quantum Pair-Cat State on Superconducting Circuits Platform

Master's thesis in Physics

JESPER LAGERBERG

DEPARTMENT OF MICROTECHNOLOGY AND NANOSCIENCE

CHALMERS UNIVERSITY OF TECHNOLOGY
Gothenburg, Sweden 2026
www.chalmers.se

Master's thesis 2026

Toward Stabilization of the Quantum Pair-Cat State on Superconducting Circuits Platform

JESPER LAGERBERG

Department of Microtechnology and Nanoscience
Applied Quantum Physics
Chalmers University of Technology
Gothenburg, Sweden 2026

Toward Stabilization of the Quantum Pair-Cat State on Superconducting Circuits Platform
JESPER LAGERBERG

Supervisor: Dr. Maryam Khanahmadi, Applied Quantum Physics
Examiner: Professor Göran Johansson, Applied Quantum Physics

Master's Thesis 2026
Department of Microtechnology and Nanoscience
Applied Quantum Physics
Chalmers University of Technology
SE-412 96 Gothenburg
Telephone +46 31 772 1000

Cover: Finalized circuit design, together with the external fluxes, used to generate pair-cat states.

Typeset in LaTeX
Printed by Chalmers Reproservice
Gothenburg, Sweden 2026

Toward Stabilization of the Quantum Pair-Cat State on Superconducting Circuits Platform
JESPER LAGERBERG
Department of Microtechnology and Nanoscience
Chalmers University of Technology

Abstract

In this thesis, we introduce a quantum circuit for stabilizing an error-correctable two-mode quantum cat state, known as the pair-cat state. Using Foster decomposition, we derive experimentally feasible circuit parameters that engineer a dominant fifth-order flux nonlinearity, yielding the effective Hamiltonian required for pair-cat state generation. We further present implementations of logical X rotations, showcasing the possibility of rotating around the Bloch sphere and encoding quantum information.

Keywords: pair-cat, non-Gaussian, quantum, superconducting.

Acknowledgements

I'd like to thank my supervisor Dr. Maryam Khanahmadi for many fruitful discussions.

Jesper Lagerberg, Gothenburg, June 2026

List of Acronyms

Below is the list of acronyms that have been used throughout this thesis listed in alphabetical order:

ATS	Asymmetrically Threaded SQUID
BCS	Bardeen-Cooper-Schrieffer
CVQC	Continuous Variables Quantum Computing
h.c.	Hermitian Conjugate
RWA	Rotating Wave Approximation
SGM(s)	State Generating Mode(s)
SQUID	Superconducting Quantum Interference Device

L_j

Nomenclature

Below is the nomenclature of indices, operators, parameters, and variables that have been used throughout this thesis.

Indices

a_i	Indices for the first and second state generating mode i
b	Index for the buffer mode
δ	Index labelling the photon number difference between the two state generating modes
n, m	Index labelling the number state
μ	Logical basis index ($\mu = 0, 1$) for pair-cat states
p	Mode index used in Foster synthesis
j	Jump-operator index in Lindblad master equation

Operators

$\hat{a}_i/\hat{a}_i^\dagger$	Annihilation/Creation operator of state generating mode i
$\hat{b}/\hat{b}^\dagger$	Annihilation/Creation operator of the buffer mode
$\hat{\Pi}$	Parity operator
$\hat{\delta}$	Photon number difference operator
$\hat{\mathcal{H}}$	Hamiltonian operator
$\hat{\rho}$	Density matrix operator
$\hat{\rho}_S$	Reduced density matrix
$\hat{X}$	Pauli X-operator
$\hat{Y}$	Pauli Y-operator
$\hat{Z}$	Pauli Z-operator
$\hat{L}_j$	Lindblad jump operator

$\hat{p}_n$	Canonical conjugate momenta operator
$\hat{\phi}_n$	Phase operator
$\hat{f}_p$	Flux operator contribution for mode p

Parameters

α	The coherent value. A complex number that specifies the coherent state. Used interchangeably with the pair-coherent value
$\mathcal{N}$	Normalization constant for a given state
ω_i	Eigenfrequency of mode i
ω_d	Drive frequency of the external magnetic flux
ω_X	Drive frequency applied on the buffer mode to generate the X-gate
$\hbar$	Planck's reduced constant
Φ_0	Magnetic flux quantum
E_J	Geometric energy of Josephson junction
E_Σ	Total geometric Josephson energy
E_Δ	Geometric energy difference between two Josephson junctions
κ	Dissipation rate
κ_b	Buffer mode decay rate
κ_{conf}	Confinement rate
G	Effective nonlinear coupling strength
$g_{2,2}$	Four-photon interaction strength
g_x	X-gate coupling strength
$\tilde{g}_x$	Effective X-gate coupling strength
ζ	Resonant drive strength on buffer mode
ζ_X	Coherent drive strength used for X-gate
ξ	Reduced pump strength
φ_p^{ZPF}	Zero-point fluctuation for mode p
L_i	Inductance of circuit inductor i
C_i	Capacitance of circuit capacitor i
Φ_{ext}	External magnetic flux

Variables

t	Time
$\epsilon(t)$	Flux-pump amplitude
E_{JJ}	Josephson junction energy
$Z(\omega)$	Impedance
$Y(\omega)$	Admittance
φ	Reduced phase difference
F	State fidelity
$\langle n\rangle$	Average photon number

Mathematical Functions

$I_\delta(x)$	Modified Bessel function of the first kind
$J_\delta(x)$	Bessel function of the first kind

Contents

List of Figures

List of Tables

1

Introduction

A key component of quantum technology are the coherent states $|\alpha\rangle = e^{-\frac{|\alpha|^2}{2}} \sum_n^\infty \frac{\alpha^n}{\sqrt{n!}} |n\rangle$ [1–4]. These states are characterised with the complex coherence value α and satisfies $|\alpha|^2 \approx \langle n \rangle$ for arbitrary occupation number n and their use cases ranges from quantum spectroscopy [1] to constructing codes used for fault tolerant quantum computing [2–4], often with a large overhead [5]. In continuous-variable quantum computing (CVQC) specifically can they be used to encode a qubit in an harmonic oscillator [6, 7]. Here the computational basis states, $|0\rangle_L = \mathcal{N}_+ (|\alpha\rangle + |-\alpha\rangle)$ and $|1\rangle_L = \mathcal{N}_- (|\alpha\rangle - |-\alpha\rangle)$, are often referred to as the even and odd two-legged cat state since they contain the photon numbers with even and odd parity respectively, and encoded as a superposition of coherent states which are sufficiently for away from each other, such that the overlap is approximately zero [4, 8]. These states are, however, prone to amplitude damping, displacement, and dephasing errors but can be corrected by applying a continuously driven two-photon dissipation process [4, 9, 10]. However, as no cavity is perfectly isolated is there a risk for a spontaneous photon gain or loss to occur which converts the even two-legged cat state to the odd two-legged cat state and vice versa, a process that cannot easily be autonomously corrected [9]. This process can be corrected by instead encoding the coherent states into a four-legged cat state with computational basis states $|0\rangle_L = \mathcal{N}_{4+} (|\alpha\rangle + |-\alpha\rangle + |i\alpha\rangle + |-i\alpha\rangle)$ and $|1\rangle_L = \mathcal{N}_{4-} (|\alpha\rangle + |-\alpha\rangle - |i\alpha\rangle - |-i\alpha\rangle)$, in which both the zero logical, and one logical state has an even parity, and correction against spontaneous photon gains/loss can be implemented by continuously measuring the parity using the parity operator $\hat{\Pi} = (-1)^{\hat{a}^\dagger \hat{a}}$ [9, 10]. The parity operator, however, does not commute with the stabilizing dissipation process of the four-legged cat state, except at certain discrete time-points, and as a result is it not possible to correct against spontaneous photon loss and dephasing errors simultaneously [7].

The problem of correcting spontaneous photon loss/gain can be solved by utilizing a pair-cat state instead of the four-legged or two-legged cat state [7, 10]. A pair-cat state is defined similarly to a two-legged cat state but instead of using a single mode does it require two modes with the same coherence parameter. As such is the computational basis state defined as $|0\rangle_L = \mathcal{N}_0 (|\alpha_\delta\rangle + |i\alpha_\delta\rangle)$ and $|1\rangle_L = \mathcal{N}_1 (|\alpha_\delta\rangle - |i\alpha_\delta\rangle)$ where $|\alpha_\delta\rangle = \mathcal{N} \sum_n^\infty \frac{\alpha^{2n+\delta}}{\sqrt{n!(n+\delta)!}} |n, n+\delta\rangle$, where δ is the photon number difference between the two modes. Since the photon number difference is the same between the two nodes for both computational states, can we correct against spontaneous photon loss/gain by measuring the photon number difference using the photon number difference operator, $\hat{\delta} = \hat{a}_2^\dagger \hat{a}_2 - \hat{a}_1^\dagger \hat{a}_1$, to check if any spontaneous photon loss/gain has occurred. This operator has one clear advantage over the parity operator, it commutes with the stabilizing dissipation process of the pair-cat state, allowing us to measure the photon number difference while the stabilizing dissipation process is active [7, 10]. There exists, therefore a need of designing a circuit that can implement the stabilizing process of a pair-cat state; and in this thesis, building on the work done by Campagne-Ibarcq's group [11] for four-legged cat qubits, we suggest a superconducting circuit design, in which by using a buffer mode, we can implement a four-photon dissipation process that stabilizes a continuous variable quantum computing qubit encoded using the pair-cat states.

2

Theory

In this chapter, we formally introduce the idea of a pair-cat state and circuit that may be used to generate the state, introducing the required mathematics along the way.

2.1 Introduction to Superconducting Circuits

It is well known that the Hamiltonian, $\hat{\mathcal{H}}$, of the electromagnetic field in a vacuum can be described using the harmonic oscillator,

$$\hat{\mathcal{H}} = \hbar\omega\left(\hat{a}^\dagger\hat{a} + \frac{1}{2}\right) \tag{2.1}$$

where ω is the frequency of the photons, $\hbar$ is Planck's reduced constant, and $\hat{a}^\dagger, \hat{a}$ are the creation and annihilation operators of the electromagnetic field respectively and satisfies the bosonic commutation relation, $\left[\hat{a}_n, \hat{a}_m^\dagger\right] = \delta_{nm}$ [12]. Note that for the rest of the thesis will we choose units such that $\hbar = 1$. It is also well known that the same Hamiltonian can be constructed using a superconducting LC-resonators [13].

For two LC-resonators with eigenfrequencies ω_a and ω_b, we get that the Hamiltonian, up to a constant term, takes the form $\hat{\mathcal{H}} = \omega_a\hat{a}^\dagger\hat{a} + \omega_b\hat{b}^\dagger\hat{b}$, and we observe no interaction between the two modes. A circuit element which facilitates an interaction between the modes is therefore needed, such as the Josephson junction [14], and is in our circuit depicted as a box with a cross in it.

A Josephson junction is constructed by placing a thin insulator between two superconductors [13–15]. In classical physics, no electrons and therefore current, is expected to flow through the insulator, but for superconductors where the resistance is zero and the conductivity is perfect may the electrons condense into a single Bardeen-Cooper-Schrieffer (BCS) ground state, characterized with an amplitude and a phase which allows for electrons in pairs to tunnel from one side to the other [13]. The condensation process into a single ground state only occurs at superconducting temperatures, when a net attractive interaction between electrons allows them to form a bound state, known as a Cooper pair [16]. These Cooper pairs behaves as composite bosons and follow Bose statistics [17], allowing the pairs to occupy the same quantum state and causes the field operator to have a non-zero expectation value that scales with the number of Cooper pairs [18,19]. If sufficiently many Cooper pairs are formed then the field operator in one of the superconductors will overlap with the field operator in the other superconductor causing tunnelling between the insulator separating the superconductors depending on the phase difference, ϕ, according to

$$I(t) = I_c \sin(\phi(t)) \tag{2.2}$$

$$V(t) = \frac{\dot{\phi}(t)}{2q_e} \tag{2.3}$$

where I_c is the critical current and q_e is the charge of the electron [13]. The energy contribution of the Josephson junction over time is

$$E_{JJ} = -E_J \cos\left(\frac{2\pi}{\Phi_0}\phi(t)\right) \tag{2.4}$$

where Φ_0 is the magnetic flux quantum and E_J is the Josephson energy of the junction which depends on the geometry of said junction [13]. Furthermore, the phase difference $\phi(t)$ can be expressed using the previously established annihilation and creation operators; allowing for non-linear interactions between multiple modes.

2.2 Coherent States and Pair-Cat States

Noting that both the linear resonators and the non-linear interaction terms can be expressed as a function of the annihilation and creation operators is it apt to represent the states of our circuit as a superposition of the eigenstates for the annihilation operator.

The coherent state, $|\alpha\rangle$, is defined to be the eigenstate of the annihilation operator, *i.e.* $\hat{a}|\alpha\rangle = \alpha|\alpha\rangle$, and is in the Fock space expressed as

$$|\alpha\rangle = e^{-\frac{|\alpha|^2}{2}} \sum_{n=0}^{\infty} \frac{\alpha^n}{\sqrt{n!}}|n\rangle \tag{2.5}$$

where α is the coherence parameter [20]. Note that two coherent states $|\alpha\rangle$ and $|\beta\rangle$ are not orthogonal as

$$\langle\alpha|\beta\rangle = e^{\alpha^*\beta - \frac{|\alpha|^2+|\beta|^2}{2}} \neq 0. \tag{2.6}$$

That being said can we often treat two coherent states as orthogonal given the difference between the two coherence numbers α and β is large [21]. One way to construct a large distance between the coherence numbers is to let $\beta = -\alpha$ and increase the size of α. One would then get $\langle\alpha| - \alpha\rangle = e^{-2|\alpha|^2} \approx 0$ for large α. However, almost zero is not zero. In order to properly describe two orthogonal states, one can implement the two-legged cat state.

The general idea of a two-legged cat state is to use two coherent states with coherence values of α and $-\alpha$ and express two new state as a superposition of these two coherent states [21]. For instance, consider the even two-legged cat state, $|\psi^+\rangle$, as

$$|\psi^+\rangle = \mathcal{N}_+\left(|\alpha\rangle + |-\alpha\rangle\right) \tag{2.7}$$

and the odd two-legged cat state, $|\psi^-\rangle$,

$$|\psi^-\rangle = \mathcal{N}_- \left(|\alpha\rangle - |-\alpha\rangle\right) \tag{2.8}$$

where $\mathcal{N}_+ = \left(2 + 2e^{-2|\alpha|^2}\right)^{-1/2}$ and $\mathcal{N}_- = \left(2 - 2e^{-2|\alpha|^2}\right)^{-1/2}$. In the Fock basis, the even two-legged cat state takes the form

$$|\psi^+\rangle = \mathcal{N}_+^{\text{fock}} \sum_{n=0}^{\infty} \frac{\alpha^{2n}}{\sqrt{(2n)!}} |2n\rangle \tag{2.9}$$

and the odd two-legged cat state takes the form

$$|\psi^-\rangle = \mathcal{N}_-^{\text{fock}} \sum_{n=0}^{\infty} \frac{\alpha^{2n+1}}{\sqrt{(2n+1)!}} |2n+1\rangle \tag{2.10}$$

with the normalization constants $\mathcal{N}_\pm^{\text{fock}}$. Since for non-zero α, $\langle\psi^+|\psi^-\rangle = 0$, one might be tempted to use $|\psi^\pm\rangle$ as the logical basis states for quantum computation. These codes however, cannot autonomously protect against spontaneous photon loss/gain as a spontaneous photon loss/gain will convert $|\psi^-\rangle$ to $|\psi^+\rangle$ or vice versa and therefore remain in the code subspace.

In order to autonomously correct spontaneous photon loss/gain one can introduce the four-legged cat state and stabilize it through a four-photon driven dissipation process that can protect against dephasing errors [7,9]. These four-legged cat states can be encoded into the logical basis states $|0\rangle_L$ and $|1\rangle_L$ as

$$|0\rangle_L = \mathcal{N}_{4L,0} \left(|\alpha\rangle + |-\alpha\rangle + |i\alpha\rangle + |-i\alpha\rangle\right) = \mathcal{N}_{4L,0}^{\text{fock}} \sum_{n=0}^{\infty} \frac{\alpha^{4n}}{\sqrt{(4n)!}} |4n\rangle \tag{2.11}$$

and

$$|1\rangle_L = \mathcal{N}_{4L,1} \left(|\alpha\rangle + |-\alpha\rangle - |i\alpha\rangle - |-i\alpha\rangle\right) = \mathcal{N}_{4L,1}^{\text{fock}} \sum_{n=0}^{\infty} \frac{\alpha^{4n+2}}{\sqrt{(4n+2)!}} |4n+2\rangle. \tag{2.12}$$

These states can be corrected against spontaneous photon loss/gain by measuring the parity of the state using the parity operator $\hat{\Pi} = (-1)^{\hat{a}^\dagger \hat{a}}$. Note however, that we cannot protect against dephasing and spontaneous photon loss/gain errors simultaneously as the parity operator only commutes with the stabilizing dissipation given by the jump operator $\hat{L}_{4L} = \hat{a}^4 - \alpha^4$ at specific points in time [7]. The jump operator and its role in stabilizing states is explained in depth in Chapter 2.3. A code that can protect against dephasing and a single spontaneous photon loss/gain simultaneously is the code utilizing pair-cat states instead [7].

A pair-cat state is constructed similar to the two-legged cat state, but with pair-coherent states instead [7]. These pair-coherent states (first introduced by Barut and Girardello [22]) require two modes a_1 and a_2, in contrast to the one mode required for coherent states, and is defined as $\hat{a}_1\hat{a}_2|\alpha_\delta\rangle = \alpha^2|\alpha_\delta\rangle$ where $\hat{a}_1$ and $\hat{a}_2$ are the annihilation operators for their corresponding mode and δ is the photon number difference between the two modes [7]. The pair-coherent state can then be described in the Fock basis as

$$|\alpha_\delta\rangle = \frac{1}{\sqrt{I_\delta\left(2|\alpha|^2\right)}} \sum_{n=0}^{\infty} \frac{\alpha^{2n+\delta}}{\sqrt{n!(n+\delta)!}} |n, n+\delta\rangle \tag{2.13}$$

where $I_\delta(\cdot)$ is the modified Bessel function of the first kind. We can then define the even and odd pair-cat state in a similar manner to how we defined the even and odd two-legged cat states

$$|\psi^+_{\alpha_\delta}\rangle = \mathcal{N}_{+\delta}\left(|\alpha_\delta\rangle + (-i)^\delta |i\alpha_\delta\rangle\right) \tag{2.14}$$

and

$$|\psi^-_{\alpha_\delta}\rangle = \mathcal{N}_{-\delta}\left(|\alpha_\delta\rangle - (-i)^\delta |i\alpha_\delta\rangle\right) \tag{2.15}$$

where $\mathcal{N}_{+\delta}$ is the normalisation constant for the even pair-cat state and $\mathcal{N}_{-\delta}$ is the normalisation constant for the odd pair-cat state. We can also, assuming that we as before have $\langle\alpha_\delta|i\alpha_\delta\rangle \approx 0$, define the logical basis states $|0\rangle_L = |\psi^+_{\alpha_\delta}\rangle$ and $|1\rangle_L = |\psi^-_{\alpha_\delta}\rangle$ for any arbitrary α and any arbitrary integer δ as

$$|\mu_{\alpha_\delta}\rangle_L = \mathcal{N}_{\mu,\delta} \sum_{n=0}^{\infty} \frac{\alpha^{4n+2\mu+\delta}}{\sqrt{(2n+\mu)!\,(2n+\mu+\delta)!}} |2n+\mu, 2n+\mu+\delta\rangle \tag{2.16}$$

where $\mu \in \{0, 1\}$, and $\mathcal{N}_{\mu,\delta}$ is the corresponding normalization constant [7]. The normalization constant can be expressed explicitly as

$$\mathcal{N}_{\mu,\delta} = \sqrt{\frac{2}{I_\delta\left(2|\alpha|^2\right) + (-1)^\mu J_\delta\left(2|\alpha|^2\right)}} \tag{2.17}$$

where J_δ is the Bessel function of first kind. The pair-cat states are useful as the code subspace all have the same δ-value, a value that is easily predictable as initializing the states from vacuum gives δ the value of 0 [23]. Ergo, by measuring the photon number difference (PND), δ, using $\hat{\delta} = \hat{a}_2^\dagger \hat{a}_2 - \hat{a}_1^\dagger \hat{a}_1$ can we correct against spontaneous photon loss/gain. Importantly, this correction can be implemented at the same time as the stabilizing dissipation process that protect it against dephasing errors as the PND-operator commutes with the stabilizing dissipation given by the jump operator $\hat{L} = \hat{a}_1^2 \hat{a}_2^2 - \alpha^4$ for all points in time [7].

That the dissipation process stabilizes the state is shown in Chapter 2.3.

2.3 Dynamics of a Quantum System

The state that describes a quantum system is called the wave function, $|\psi\rangle$, and for our system of pair-cat states take the general form

$$|\psi\rangle = c_0|\alpha_\delta\rangle + c_1|i\alpha_\delta\rangle \tag{2.18}$$

where $|c_0|^2 + |c_1|^2 = 1$ and corresponds to the density matrix

$$\hat{\rho} = |\psi\rangle\langle\psi| = |c_0|^2 |\alpha_\delta\rangle\langle\alpha_\delta| + c_0 c_1^* |\alpha_\delta\rangle\langle i\alpha_\delta| + c_0^* c_1 |i\alpha_\delta\rangle\langle\alpha_\delta| + |c_1|^2 |i\alpha_\delta\rangle\langle i\alpha_\delta|. \tag{2.19}$$

In particular, what is presented in Equation 2.18 is known as a pure state as the corresponding density matrix can be described as a cross product of a single wave function [24]. Mixed states can arise when entangling two states, a process that is necessary in order to achieve efficient quantum computations that cannot be performed on a classical computer [25]. To see why an entangled state cannot necessarily be described as a pure state, consider two observers Alice and Bob that each measure the spin of a particle. These spins can either be measured to be up, $|\uparrow\rangle$, or down, $|\downarrow\rangle$ and let us assume that both states are equally likely for both Alice's and Bob's particle. Now let us also assume that if we have a process in which if Alice's particle is in state $|\uparrow\rangle$ then Bob's particle immediately collapses to $|\downarrow\rangle$ regardless of what spin it originally had, but if Alice's particle is in $|\downarrow\rangle$ then Bob's particle is unaffected. We can then introduce the density operator, $\hat{\rho}$, that describes this entangled quantum state as

$$\hat{\rho} = \frac{1}{4}|\downarrow_A\downarrow_B\rangle\langle\downarrow_A\downarrow_B| + \frac{1}{4}|\downarrow_A\uparrow_B\rangle\langle\downarrow_A\uparrow_B| + \frac{1}{2}|\uparrow_A\downarrow_B\rangle\langle\uparrow_A\downarrow_B| \tag{2.20}$$

where A and B denotes Alice's and Bob's particle respectively. Note that the state in Equation 2.20 is a mixed state as the density matrix cannot be written as a cross product of a single wave function [24]. In order to properly describe the time-evolution of the quantum system is it therefore apt to consider the time-evolution of the density matrix.

2.3.1 Time-evolution of an Isolated Quantum System

The time-evolution of a quantum system can be described by the time-evolution of the density matrix. Which using Schrödinger's equation, $i\frac{\mathrm{d}}{\mathrm{d}t}|\psi(t)\rangle = \hat{\mathcal{H}}|\psi(t)\rangle$, for an arbitrary state $|\psi(t)\rangle$, we get that the time-evolution for the density matrix is

$$\frac{\mathrm{d}}{\mathrm{d}t}\hat{\rho} = -i\hat{\mathcal{H}}|\psi(t)\rangle\langle\psi(t)| + |\psi(t)\rangle\frac{\mathrm{d}}{\mathrm{d}t}\langle\psi(t)| = -i\left[\hat{\mathcal{H}}, \hat{\rho}\right]. \tag{2.21}$$

The time-evolution of the density matrix should stabilize a linear combination of pair-coherent states $|\alpha_\delta\rangle$, and should therefore satisfy $\frac{\mathrm{d}}{\mathrm{d}t}\hat{\rho} = 0$ for $\hat{\rho} = \sum_{\alpha_\delta,\alpha'_\delta} C_{\alpha_\delta\alpha'_\delta}|\alpha_\delta\rangle\langle\alpha'_\delta|$, with $C_{\alpha_\delta\alpha'_\delta} \in \mathbb{C}$. Ergo, we want $\hat{\mathcal{H}}|\alpha_\delta\rangle\langle\alpha'_\delta| = |\alpha_\delta\rangle\langle\alpha'_\delta|\hat{\mathcal{H}}$. Recall that $\hat{a}_1\hat{a}_2|\alpha_\delta\rangle = \alpha^2|\alpha_\delta\rangle$ where $\hat{a}_1$ and $\hat{a}_2$ are the annihilation operators for the different modes. Then in order for the density matrix to remain unchanged after applying the Hamiltonian, we need said Hamiltonian to be on the form $\hat{\mathcal{H}} = \sum_{n=1}^{\infty} g_{n,n}\hat{a}_1^n\hat{a}_2^n + \text{h.c.}$. Furthermore, since we want to stabilize the logical qubit states, presented in Equation 2.16, and these states have a parity structure analogous to the cat-state, which means the Hamiltonian should not consists of any operators that can break the parity structure, *i.e.* $g_{2m+1,2m+1} = 0$ for $m \in \mathbb{N}$.

Consider then the simplest case of $\hat{\mathcal{H}} = g_{2,2}\hat{a}_1^2\hat{a}_2^2 + g_{2,2}^*\hat{a}_1^{\dagger^2}\hat{a}_2^{\dagger^2}$ then the time-evolution of the term $|\alpha_\delta\rangle\langle\alpha'_\delta|$ takes the form

$$\begin{aligned}\frac{\mathrm{d}}{\mathrm{d}t}\left(|\alpha_\delta\rangle\langle\alpha'_\delta|\right) &= -i\left[g_{2,2}\hat{a}_1^2\hat{a}_2^2 + g_{2,2}^*\hat{a}_1^{\dagger^2}\hat{a}_2^{\dagger^2}, |\alpha_\delta\rangle\langle\alpha'_\delta|\right] \\ &= -i\left(g_{2,2}\alpha^4 - g_{2,2}^*\alpha'^{*^4} + g_{2,2}^*\hat{a}_1^{\dagger^2}\hat{a}_2^{\dagger^2}|\alpha_\delta\rangle\langle\alpha'_\delta| - g_{2,2}|\alpha_\delta\rangle\langle\alpha'_\delta|\hat{a}_1^2\hat{a}_2^2\right)\end{aligned} \tag{2.22}$$

which is not 0 for any value of α and α'. There is thereby a need to engineer a dissipation channel that removes the unwanted operator terms $g_{2,2}^{*}\hat{a}_1^{\dagger^2}\hat{a}_2^{\dagger^2}|\alpha_\delta\rangle\langle\alpha'_\delta| - g_{2,2}|\alpha_\delta\rangle\langle\alpha'_\delta|\hat{a}_1^2\hat{a}_2^2$ such that there exists some α and α' for which the time-evolution of density matrix is 0.

2.3.2 Time-evolution of an Open Quantum System

The total Hamiltonian for a system is $\hat{\mathcal{H}} = \hat{\mathcal{H}}_S + \hat{\mathcal{H}}_B + \hat{\mathcal{H}}_I$ where $\hat{\mathcal{H}}_S$ is the Hamiltonian for a subsystem; $\hat{\mathcal{H}}_B$ is the Hamiltonian for the rest of the system, also known as the bath, and $\hat{\mathcal{H}}_I$ is the interaction Hamiltonian between the subsystem and the bath [26]. The total density matrix, $\hat{\rho}_{SB}$, then time-evolves as

$$\frac{\mathrm{d}}{\mathrm{d}t}\hat{\rho}_{SB} = -i\left[\hat{\mathcal{H}}, \hat{\rho}_{SB}\right]. \tag{2.23}$$

Furthermore, by assuming the Markovian approximation [26,27] and tracing out the bath from Equation 2.23 and following the calculation presented in [26] is it possible to obtain the time-evolution of the density matrix for the subsystem as a function of the subsystems Hamiltonian and its interaction with the bath. The time-evolution of the density matrix then takes the form

$$\frac{\mathrm{d}}{\mathrm{d}t}\hat{\rho}_S = -i\left[\hat{\mathcal{H}}, \hat{\rho}_S\right] + \sum_j \left(\hat{L}_j\hat{\rho}_S\hat{L}_j^\dagger - \frac{1}{2}\left\{\hat{L}_j^\dagger\hat{L}_j, \hat{\rho}_S\right\}\right) \tag{2.24}$$

where $\hat{L}_j$ are the jump operators, and describes how the bath acts on the system [26, 28–30]. If we have the same Hamiltonian as before but engineer a four-photon dissipation channel such that $\hat{L}_j = \sqrt{\kappa}\hat{a}_1^2\hat{a}_2^2$ with some dissipation rate κ; then the time-evolution of the density matrix becomes

$$\frac{\mathrm{d}}{\mathrm{d}t}\hat{\rho}_S = -i\left[g_{2,2}\hat{a}_1^2\hat{a}_2^2 + g_{2,2}^{*}\hat{a}_1^{\dagger^2}\hat{a}_2^{\dagger^2}, \hat{\rho}_S\right] + \kappa\left(\hat{a}_1^2\hat{a}_2^2\hat{\rho}_S\hat{a}_1^{\dagger^2}\hat{a}_2^{\dagger^2} - \frac{1}{2}\left\{\hat{a}_1^{\dagger^2}\hat{a}_2^{\dagger^2}\hat{a}_1^2\hat{a}_2^2, \hat{\rho}_S\right\}\right) \tag{2.25}$$

and $\frac{\mathrm{d}}{\mathrm{d}t}\left(|\alpha_\delta\rangle\langle\alpha'_\delta|\right)$ evaluates to

$$\begin{aligned}\frac{\mathrm{d}}{\mathrm{d}t}\left(|\alpha_\delta\rangle\langle\alpha'_\delta|\right) = &-i\left(g_{2,2}\alpha^4 - g_{2,2}^{*}\alpha'^{*^4} + g_{2,2}^{*}\hat{a}_1^{\dagger^2}\hat{a}_2^{\dagger^2}|\alpha_\delta\rangle\langle\alpha'_\delta| - g_{2,2}|\alpha_\delta\rangle\langle\alpha'_\delta|\hat{a}_1^2\hat{a}_2^2\right)\\ &+\frac{\kappa}{2}\left(2\alpha^4\alpha'^{*^4} - \alpha^4\hat{a}_1^{\dagger^2}\hat{a}_2^{\dagger^2}|\alpha_\delta\rangle\langle\alpha'_\delta| - \alpha'^{*^4}|\alpha_\delta\rangle\langle\alpha'_\delta|\hat{a}_1^2\hat{a}_2^2\right)\end{aligned} \tag{2.26}$$

and have the steady-state solutions

$$\alpha = \begin{cases} e^{i\frac{\pi}{4}}\sqrt[4]{\frac{2g_{2,2}^{*}}{\kappa}} \\ e^{i\frac{5\pi}{4}}\sqrt[4]{\frac{2g_{2,2}^{*}}{\kappa}} \\ e^{-i\frac{\pi}{4}}\sqrt[4]{\frac{2g_{2,2}^{*}}{\kappa}} \\ e^{-i\frac{5\pi}{4}}\sqrt[4]{\frac{2g_{2,2}^{*}}{\kappa}} \end{cases} \tag{2.27}$$

and the constraint $\alpha'^4 = \alpha^4$. Note that the photon number difference δ, does not affect the coherence value of the system. The stabilized density matrix of the system can then be expressed as

$$\hat{\rho}_S = C_{++}|\psi^+_{\alpha_\delta}\rangle\langle\psi^+_{\alpha_\delta}| + C_{+-}|\psi^+_{\alpha_\delta}\rangle\langle\psi^-_{\alpha_\delta}| + C_{-+}|\psi^-_{\alpha_\delta}\rangle\langle\psi^+_{\alpha_\delta}| + C_{--}|\psi^-_{\alpha_\delta}\rangle\langle\psi^-_{\alpha_\delta}| \qquad (2.28)$$

where $|\psi^+_{\alpha_\delta}\rangle$ and $|\psi^-_{\alpha_\delta}\rangle$ are defined as in Equations 2.14 and 2.15.

2.4 Constructing the Circuit

Campagne-Ibarcq's group [11], managed to engineer a near Kerr-free superconducting circuit that stabilizes the four-legged cat state. They achieved this by coupling three capacitor pads together in series with a normal inductor between the first two and an asymmetrically threaded SQUID (ATS) [31] between the second and third capacitor pad. This generated two modes, one state-generating mode (SGM) and one lossy buffer mode with which they could engineer the four-photon dissipation of the SGM. We extend this design by adding another inductor coupled with an additional capacitor pad to the capacitor pad that is only connected with the ATS (see Figure 2.1).

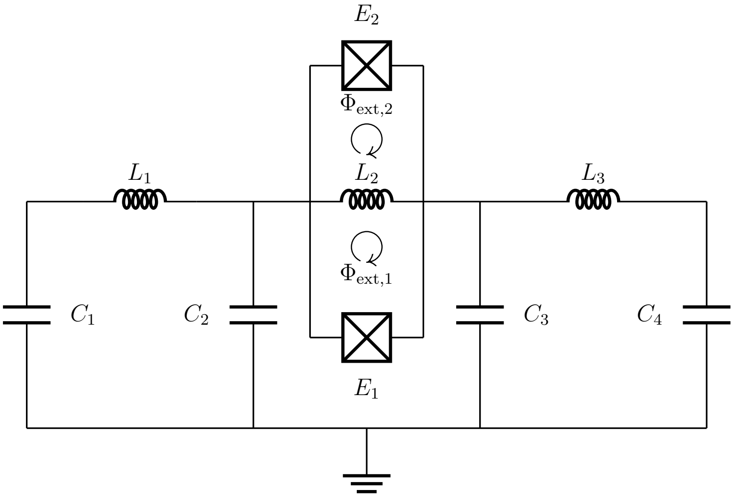

Figure 2.1: Our suggested circuit. Four capacitor pads are placed in a tower, with an inductor placed between the outer pair of capacitors, and an ATS in between the middle pair. The capacitor pads are connected to a ground plane.

Here E_{J_L} and E_{J_R} are the Josephson energies of the left and right Josephson junction respectively in the ATS, L_i and C_i are the inductance/capacitance of inductor/capacitor pad i, and $\Phi_{\text{ext},1}$ and $\Phi_{\text{ext},2}$ are the external magnetic fluxes that arises between two inductive elements [13].

By performing a Foster synthesis [32], is it possible to find a closed circuit that has the same impedance of the linear elements, of which the quantized eigenmodes are the same as for our original circuit [33]. As our Foster synthesis only treat the linear terms, are we going to

2.4.1 Foster Synthesis of the Circuit

A Foster synthesis is performed by applying a Laplace transformation on the time-domain of an arbitrary signal in the circuit and then constructing another circuit that yields the same response after a Laplace transformation [32]. After the Laplace transformation, we obtain the impedance, which for a capacitor is $Z_{\text{Cap}}(\omega) = \frac{1}{-iC\omega}$ and for an inductor $Z_{\text{Ind}}(\omega) = -iL\omega$, where ω is the frequency and C, and L are the capacitance and inductance respectively [34]. Furthermore, for two elements with impedances $Z_1(\omega)$ and $Z_2(\omega)$ can the effective impedance, $Z_{\text{eff}}(\omega)$ be calculated as $Z_{\text{eff}}(\omega) = Z_1(\omega) + Z_2(\omega)$ if the elements are placed in series, and $Z_{\text{eff}}(\omega) = \left(Z_1(\omega)^{-1} + Z_2(\omega)^{-1}\right)^{-1}$ if they are placed in parallel.

The synthesis will be performed from the point of view of the non-linear Josephson junctions, with the goal of rewriting the circuit into an equivalent one with three LC-circuits that generates three independent bosonic modes and a superconducting quantum interference device (SQUID). The first step of the process is to combine the left, central and right impedances into one, as seen in Figure 2.2.

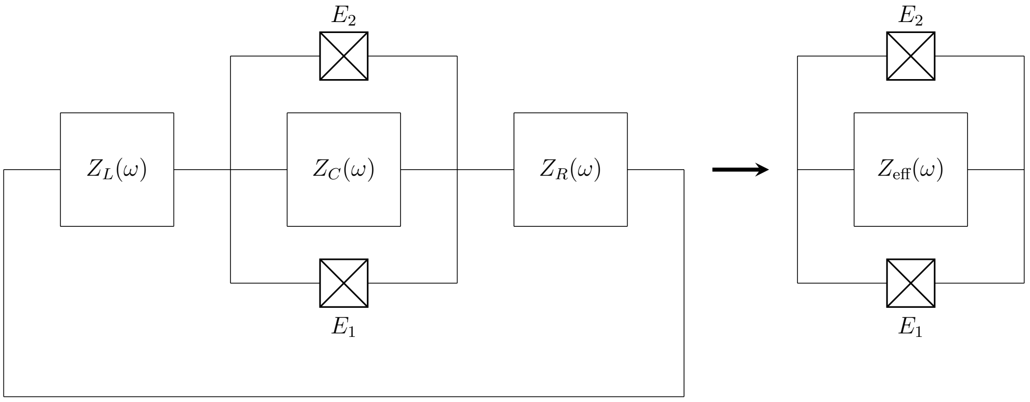

Figure 2.2: Schematic process of Foster synthesis. The three impedances $Z_L(\omega)$, $Z_C(\omega)$ and $Z_R(\omega)$ are combined into one single, effective impedance $Z_{\text{eff}}(\omega)$.

The left impedance, $Z_L(\omega)$ corresponds to the impedance of the leftmost part of the circuit in Figure 2.1, and is

$$\begin{aligned} Z_L(\omega) &= \left(\left(\frac{1}{-i\omega C_1} - i\omega L_1\right)^{-1} - i\omega C_2\right)^{-1} \\ &= i\frac{\omega^2 C_1 L_1 - 1}{(C_1 + C_2)\,\omega\left(\omega^2 \frac{C_1 C_2}{C_1 + C_2} L_1 - 1\right)} \end{aligned} \tag{2.29}$$

The central impedance, $Z_C(\omega)$, is simply the impedance of the inductor in the ATS and is

$$Z_C(\omega) = -i\omega L_2. \tag{2.30}$$

Finally the right impedance, $Z_R(\omega)$, corresponds to the impedance of the rightmost part of the circuit in Figure 2.1 and is

$$\begin{aligned} Z_R(\omega) &= \left(\left(\frac{1}{-i\omega C_4} - i\omega L_3\right)^{-1} - i\omega C_3\right)^{-1} \\ &= i\frac{\omega^2 C_4 L_3 - 1}{\left(C_3 + C_4\right)\omega\left(\omega^2 \frac{C_3 C_4}{C_3+C_4} L_3 - 1\right)}. \end{aligned} \tag{2.31}$$

The effective impedance of the circuit, $Z_{\text{eff}}(\omega)$, is then

$$\begin{aligned} Z_{\text{eff}}(\omega) &= \left(\left(Z_L(\omega) + Z_R(\omega)\right)^{-1} + Z_C(\omega)^{-1}\right)^{-1} \\ &= i\frac{P_5\omega^5 - P_3\omega^3 + P_1\omega}{Q_6\omega^6 - Q_4\omega^4 + Q_2\omega^2 - Q_0} = i\frac{P(\omega)}{Q(\omega)} \end{aligned} \tag{2.32}$$

with

$$\begin{cases} P_5 = \frac{C_1C_4(C_2+C_3)}{C_1+C_2+C_3+C_4} L_1L_2L_3 \\ P_3 = \frac{C_1(C_2+C_3+C_4)L_1+C_4(C_1+C_2+C_3)L_3}{C_1+C_2+C_3+C_4} L_2 \\ P_1 = L_2 \\ Q_6 = \frac{C_1C_2C_3C_4}{C_1+C_2+C_3+C_4} L_1L_2L_3 \\ Q_4 = \frac{C_1C_2(C_3+C_4)L_1L_2+C_1C_4(C_2+C_3)L_1L_3+C_3C_4(C_1+C_2)L_2L_3}{C_1+C_2+C_3+C_4} \\ Q_2 = \frac{C_1(C_2+C_3+C_4)L_1+(C_1+C_2)(C_3+C_4)L_2+C_4(C_1+C_2+C_3)L_3}{C_1+C_2+C_3+C_4} \\ Q_0 = 1 \end{cases}. \tag{2.33}$$

A circuit consisting of M LCR-oscillators in series has the impedance

$$Z(\omega) = \sum_{p=1}^{M}\left(-i\omega C_p + \frac{1}{-i\omega L_p} + \frac{1}{R_p}\right)^{-1} \tag{2.34}$$

where the imaginary parts of the poles are $\left(2R_pC_p\right)^{-1}$ and the real part of the poles, gives the resonance frequencies of the LC-circuits, $\omega_p = \left(L_pC_p\right)^{-1/2}$ [33]. Furthermore, the resistance and capacitance of LCR-oscillator p can be explicitly calculated as $R_p = \frac{1}{\Re\text{e}(Y(\omega_p))}$ and $C_p = \frac{1}{2}\Im\text{m}\left(\frac{\text{d}Y(\omega)}{\text{d}\omega}\right)\Big|_{\omega=\omega_p}$, with $Y(\omega) = Z(\omega)^{-1}$.

Note that superconductivity is characterized by a negligible electrical resistivity [13, 35, 36], which means no current should go through the arm with the resistor of the LCR-circuit and the contribution of R_p to the impedance should be 0, *i.e.*, $\frac{1}{R_p} \to 0$. We can ensure that $R_p \to \infty$ by choosing the values on the inductors and capacitors such that ω_p^2 is both real and positive.

The function in the denominator is that of a cubic equation, $Q(\sqrt{x}) = Q_6x^3 - Q_4x^2 + Q_2x - Q_0$, with $x = \omega^2$. As such can we ensure that all roots, x, are real by ensuring that the discriminant, Δ, of the function is larger than or equal to 0 [37]. This constraint then take the form

$$\Delta = -27\left(\frac{Q_0}{Q_6}\right)^2 + \left(18\frac{Q_4Q_2}{Q_6^2} - 4\left(\frac{Q_4}{Q_6}\right)^3\right)\frac{Q_0}{Q_6} + \frac{Q_4Q_2}{Q_6^2} - 4\left(\frac{Q_2}{Q_6}\right)^3 > 0 \tag{2.35}$$

and is the only constraint necessary on the circuit parameters. At first glance it might seem that Equation 2.35 allows for $\omega^2 = x < 0$ and therefore imaginary poles of the impedance, but the structure of $Q(\omega)$ does not allow for the real roots, x_p, to be negative. To see this, consider Vieta's formula for which the roots of the polynomial equation $Q_6x^3 - Q_4x^2 + Q_2x - Q_0 = 0$ satisfies

$$x_1 + x_2 + x_3 = \frac{Q_4}{Q_6} \tag{2.36}$$

$$x_1x_2 + x_1x_3 + x_2x_3 = \frac{Q_2}{Q_6} \tag{2.37}$$

$$x_1x_2x_3 = \frac{Q_0}{Q_6} \tag{2.38}$$

where x_1, x_2, and x_3 are the possible roots of the third degree polynomial [38]. Note that for our specific case is the right-hand side of Equation 2.36 through Equation 2.38 all real and positive. If (x_1, x_2, x_3) are all greater than 0, then Equations 2.36 through 2.38 are all trivially satisfied. If only one of the roots is less than 0, then the left-hand side of Equation 2.38 is less than 0, while the right-hand side is greater than 0 leading to a contradiction. We can therefore not have a root x_i that is less than 0 while the others are greater than 0. In the case where all roots are less than 0, the left-hand side of Equation 2.38 evaluate to a negative number, while the right-hand side is positive - leading to a contradiction.

In the specific case where two roots are less than 0, we consider $x_1 > 0$ without loss of generality; then Equation 2.36 gives the constraint that $x_1 > |x_2| + |x_3|$ and Equation 2.37 gives the constraint $|x_2||x_3| > x_1\left(|x_2| + |x_3|\right)$. The two constraints imply

$$|x_2||x_3| > \left(|x_2| + |x_3|\right)^2 = |x_2|^2 + 2|x_2||x_3| + |x_3|^2 \implies -|x_2||x_3| > |x_2|^2 + |x_3|^2 \tag{2.39}$$

which is not true for any x_2 or x_3. The only possible solutions of $Q(\sqrt{x})$ is then that the roots, x_p, are all positive real, which means that the roots ω_p are also therefore all real, and Equation 2.35 is therefore the only constraint we need the circuit parameters to satisfy in order to have no contribution from the resistance.

After a valid eigenfrequency is obtained can we calculate the corresponding capacitance, C_p, by taking half of the imaginary part of the derivative of the admittance [33]. We then get

$$\frac{\mathrm{d}Y(\omega)}{\mathrm{d}\omega} = -i\frac{\frac{\mathrm{d}P(\omega)}{\mathrm{d}\omega}Q(\omega) - \frac{\mathrm{d}Q(\omega)}{\mathrm{d}\omega}P(\omega)}{Q(\omega)^2}\frac{Q(\omega)^2}{P(\omega)^2} = -i\left(\frac{\frac{\mathrm{d}P(\omega)}{\mathrm{d}\omega}}{P(\omega)}\frac{i}{Z(\omega)} - \frac{\frac{\mathrm{d}Q(\omega)}{\mathrm{d}\omega}}{P(\omega)}\right) \tag{2.40}$$

and since we only evaluate ω when it is a pole of $Z(\omega)$, and both $P(\omega)$ and $\frac{\mathrm{d}P(\omega)}{\mathrm{d}\omega}$ are real for $\omega = \omega_p$, we obtain

$$C_p = \frac{1}{2}\Im\mathrm{m}\left(\frac{\mathrm{d}Y(\omega)}{\mathrm{d}\omega}\right)\Bigg|_{\omega=\omega_p} = \frac{1}{2}\left(\frac{\frac{\mathrm{d}Q(\omega)}{\mathrm{d}\omega}}{P(\omega)}\right)\Bigg|_{\omega=\omega_p} = \frac{3Q_6\omega_p^5 - 2Q_4\omega_p^3 + Q_2\omega_p}{P_5\omega_p^5 - P_3\omega_p^3 + P_1\omega_p} \tag{2.41}$$

from which we can obtain the strength of the inductance through $L_p = \left(\omega_p^2 C_p\right)^{-1}$. The result is the equivalent circuit of Figure 2.1 presented in Figure 2.3, in which three LC-resonators are placed in series as the central element between two parallel Josephson junctions. As a direct consequence of the Foster synthesis is the external flux between the junctions and the central elements the same as in the original circuit [11].

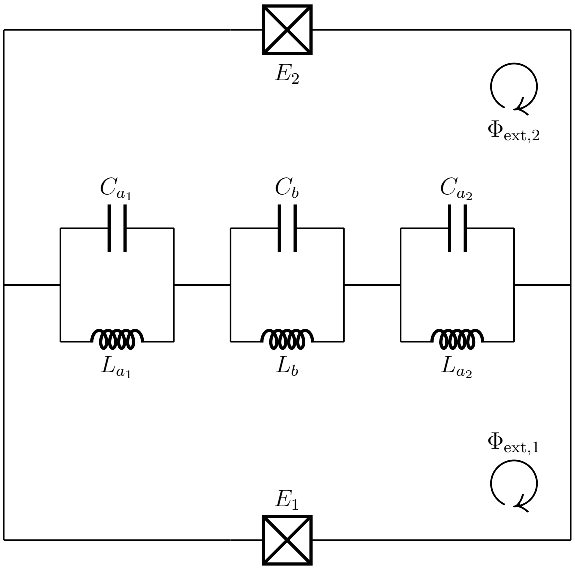

Figure 2.3: Equivalent circuit of our circuit that generates pair-cat states. Three LC-resonators are placed as the central elements between two parallel Josephson junctions with strength E_1 and E_2 respectively. Each component of the LC-resonators are denoted with either the indices a_1, a_2 or b. The indices a_1 and a_2 indicates the modes used to generate the pair-cat state, whilst the index b is the buffer mode. The external fluxes are unchanged as a consequence of the Foster synthesis.

In order to describe how this equivalent circuit give rise to the dynamics we want, is a derivation of its Hamiltonian required.

2.4.2 Hamiltonian of the Circuit

In order to properly describe the Hamiltonian and thereby the dynamics of the circuit, we need to describe how the current, $I(t)$, and voltage, $V(t)$, are distributed and changes over time [13]. If each element of the circuit corresponds to a branch, then the voltage and current over that specific branch is given by

$$V_{\text{branch}}(t) = \int_{\text{start of branch}}^{\text{end of branch}} \vec{E}(t) \cdot \mathrm{d}\vec{\ell} \tag{2.42}$$

$$I_{\text{branch}}(t) = \frac{1}{\mu_0} \oint_{\text{branch}} \vec{B}(t) \cdot \mathrm{d}\vec{\ell} \tag{2.43}$$

where μ is the vacuum permeability, $\vec{E}$ is the electric field inside the wire and $\vec{B}$ is the magnetic field outside the wire [13]. We can then introduce the branch flux, $\Phi_{\text{branch}}(t)$, and the branch charge, $Q_{\text{branch}}(t)$, as

$$\Phi_{\text{branch}}(t) = \int_{-\infty}^{t} \mathrm{d}t' V_{\text{branch}}(t') \tag{2.44}$$

$$Q_{\text{branch}}(t) = \int_{-\infty}^{t} \mathrm{d}t' I_{\text{branch}}(t'). \tag{2.45}$$

Importantly, the voltage of a capacitor is $V_{\text{Cap}}(t) = \frac{Q(t)}{C}$ and using Equation 2.45 together with $P(t) = V(t)I(t)$, where $P(t)$ is the power, and we get the energy stored in the capacitance is

$$E_{\text{Cap}}(t) = \int_{-\infty}^{t} \mathrm{d}t' \frac{Q(t')}{C} I(t') = \frac{1}{2} C \dot{\Phi}^2(t). \tag{2.46}$$

Similarly utilizing that the current in an inductor is given by $I_{\text{Ind}}(t) = \frac{\Phi(t)}{L}$ we find the energy of the inductor to be

$$E_{\text{Ind}}(t) = \frac{\Phi^2(t)}{2L}. \tag{2.47}$$

The obtained energy terms can be used to express the Lagrangian, $\mathcal{L}$, and solve the Euler-Lagrange equations, thus obtaining the time-evolution of the flux and the conjugate momenta, $p_n = \frac{\partial \mathcal{L}}{\partial \dot{\phi}_n}$, where ϕ_n is the phase difference between two modes [13, 39]. We can then promote the flux and conjugate momenta to quantum operators, by ensuring that they satisfy the canonical commutation relations $\left[\hat{\phi}_n, \hat{p}_m\right] = i\hbar\delta_{nm}$. These operators can be in turn expressed as a linear combination of the bosonic annihilation and creation operators, as they satisfy $\left[\hat{a}_n, \hat{a}_m^{\dagger}\right] = \delta_{nm}$ [13, 40].

For circuits whose linear components only consists of LC-resonators in series, such as our own, can we ignore the above laid procedure. Instead, we can use the admittance to directly obtain the flux operator of mode p as

$$\hat{\phi}_p = \sqrt{\frac{\hbar}{\omega_p \Im\mathrm{m}\left(\frac{\mathrm{d}Y(\omega)}{\mathrm{d}\omega}\right)\Big|_{\omega=\omega_p}}} \left(\hat{a}_p + \hat{a}_p^{\dagger}\right) = \hat{f}_p + \hat{f}_p^{\dagger} \tag{2.48}$$

and the contribution from the harmonic oscillators to the Hamiltonian becomes $\hat{\mathcal{H}}_0 = 2\sum_p \hat{f}_p^{\dagger} \left(L_p\right)^{-1} \hat{f}_p = \sum_p \omega_p \hat{a}_p^{\dagger} \hat{a}_p$ for $\hbar = 1$ [33]. The total Hamiltonian of the circuit can then be written as a sum of the linear Hamiltonian, $\hat{\mathcal{H}}_0$, and the contribution from the SQUID.

The energy contribution from a single Josephson junction is $-E_J \cos(\varphi(t))$ where E_J is the Josephson energy and φ is the reduced phase difference defined as $\varphi(t) = \frac{2\pi}{\Phi_0}\phi(t)$ [14]. As such can we define the zero-point fluctuation, φ_p^{ZPF}, for mode p as

$\hat{\varphi}_p(t) = \varphi_p^{ZPF}\left(\hat{p} + \hat{p}^\dagger\right)$, which can be determined analytically as

$$\varphi_p^{ZPF} = \frac{2\pi}{\Phi_0}\sqrt{\frac{\hbar}{\omega_p \Im\mathrm{m}\left(\frac{\mathrm{d}Y(\omega)}{\mathrm{d}\omega}\right)\Big|_{\omega=\omega_p}}} \tag{2.49}$$

where Φ_0 is the magnetic flux quantum and we have kept $\hbar$ for clarity. Since φ is a phase difference are we free to define a point on the circuit on which $\varphi(t) = 0$. If we define this point to be before the central elements in the equivalent circuit, see Figure 2.4,

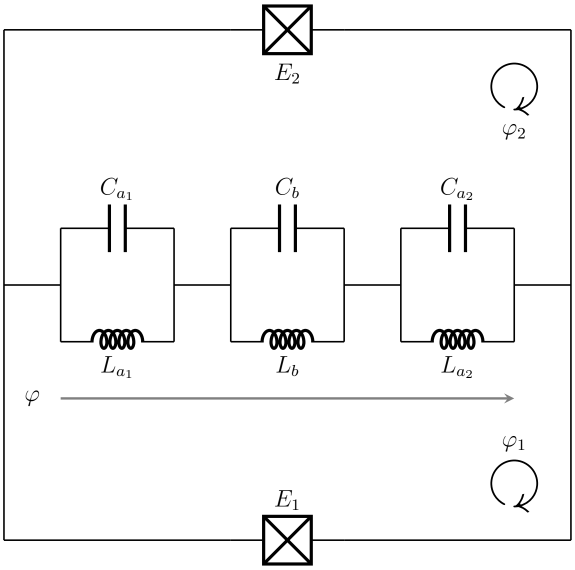

Figure 2.4: The equivalent circuit, but with added phase difference. The external magnetic fluxes are also removed and replaced with $\varphi_i = \frac{2\pi}{\Phi_0}\Phi_{\mathrm{ext,i}}$.

and we get that the energy contribution from the SQUID is

$$\begin{aligned}
E_{\mathrm{SQUID}} =& -E_1\cos(\hat{\varphi} + \varphi_1) - E_2\cos(\hat{\varphi} - \varphi_2) \\
=& -\left(E_1\cos\left(\hat{\varphi} + \frac{\varphi_\Sigma}{2} - \frac{\varphi_\Delta}{2}\right) + E_2\cos\left(\hat{\varphi} - \frac{\varphi_\Delta}{2} - \frac{\varphi_\Sigma}{2}\right)\right) \\
=& -E_1\left(\cos\left(\frac{\varphi_\Sigma}{2}\right)\cos\left(\hat{\varphi} - \frac{\varphi_\Delta}{2}\right) - \sin\left(\frac{\varphi_\Sigma}{2}\right)\sin\left(\hat{\varphi} - \frac{\varphi_\Delta}{2}\right)\right) \\
& -E_2\left(\cos\left(\frac{\varphi_\Sigma}{2}\right)\cos\left(\hat{\varphi} - \frac{\varphi_\Delta}{2}\right) + \sin\left(\frac{\varphi_\Sigma}{2}\right)\sin\left(\hat{\varphi} - \frac{\varphi_\Delta}{2}\right)\right) \\
=& -E_\Sigma\cos\left(\frac{\varphi_\Sigma}{2}\right)\cos\left(\hat{\varphi} - \frac{\varphi_\Delta}{2}\right) - E_\Delta\sin\left(\frac{\varphi_\Sigma}{2}\right)\sin\left(\hat{\varphi} - \frac{\varphi_\Delta}{2}\right)
\end{aligned} \tag{2.50}$$

where $\varphi_\Sigma = \varphi_1 + \varphi_2$, $\varphi_\Delta = \varphi_2 - \varphi_1$, $E_\Sigma = E_1 + E_2$, $E_\Delta = E_2 - E_1$,

$$\hat{\varphi} = \varphi_{a_1}^{ZPF}\left(\hat{a}_1^\dagger + \hat{a}_1\right) + \varphi_b^{ZPF}\left(\hat{b}^\dagger + \hat{b}\right) + \varphi_{a_2}^{ZPF}\left(\hat{a}_2^\dagger + \hat{a}_2\right) \tag{2.51}$$

and $\varphi_i = \frac{2\pi}{\Phi_0}\Phi_{\mathrm{ext},i}$. Here we define the operators $\hat{a}_1$ and $\hat{a}_2$ to be the annihilation operators for the SGMs and $\hat{b}$ to be the annihilation operator for the buffer mode.

If we then operate the external flux between the arms of the ATS in such a way that

$$\begin{cases} \frac{2\pi}{\Phi_0}\left(\Phi_{\text{ext},2} - \Phi_{\text{ext},1}\right) = -\pi \\ \frac{2\pi}{\Phi_0}\left(\Phi_{\text{ext},1} + \Phi_{\text{ext},2} + 2\eta\cos(\omega_d t)\right) = -\pi + 2\xi\cos(\omega_d t) \end{cases} \tag{2.52}$$

for some amplitude η and some drive frequency ω_d, and we get the following Hamiltonian

$$\begin{aligned} \hat{\mathcal{H}} =& \omega_{a_1}\hat{a}_1^\dagger\hat{a}_1 + \omega_b\hat{b}^\dagger\hat{b} + \omega_{a_2}\hat{a}_2^\dagger\hat{a}_2 \\ &+ E_\Sigma \sin\left(\xi\cos\left(\omega_d t\right)\right)\sin\left(\hat{\varphi}\right) - E_\Delta\cos\left(\xi\cos\left(\omega_d t\right)\right)\cos\left(\hat{\varphi}\right). \end{aligned} \tag{2.53}$$

From here on will we assume that the strength of the Josephson energies satisfy $E_1 = E_2 = E_\Sigma/2$. Expanding the cosine in Equation 2.53 as $\cos(\omega_d t) = \frac{e^{i\omega_d t}+e^{-i\omega_d t}}{2}$ and performing a Taylor expansion of the sine term, and we get that for the leading order of ξ

$$\hat{\mathcal{H}}_{\text{toy}} = \omega_{a_1}\hat{a}_1^\dagger\hat{a}_1 + \omega_b\hat{b}^\dagger\hat{b} + \omega_{a_2}\hat{a}_2^\dagger\hat{a}_2 + \frac{E_\Sigma\xi}{2}\left(e^{i\omega_d t} + e^{-i\omega_d t}\right)\left(\hat{\varphi} - \mathcal{O}\left(\hat{\varphi}^3\right)\right) \tag{2.54}$$

in which we can choose what terms is on resonance by modifying the drive frequency ω_d. From the argument presented in Chapter 2.3, we want the Hamiltonian to create two photons in the two SGM simultaneously. We can ensure that two photons are created simultaneously in each mode by driving the buffer mode with a resonant drive of strength ζ at the same time the drive frequency of the magnetic flux is operating at $\omega_d = 2\omega_{a_1} - \omega_b + 2\omega_{a_2}$. Rotating the Hamiltonian into the interaction picture and performing the rotating wave approximation (RWA) [41], we get the leading order of the Hamiltonian to be

$$\hat{\mathcal{H}}_{\text{RWA}} = G\hat{a}_1^{\dagger^2}\hat{b}\hat{a}_2^{\dagger^2} + \zeta^*\hat{b}^\dagger + \text{h.c.} \tag{2.55}$$

with $G = \frac{\xi}{2}E_\Sigma e^{-\frac{\left|\left|\varphi^{ZPF}\right|\right|^2}{2}}\frac{\left(\varphi_{a_1}^{ZPF}\right)^2\varphi_b^{ZPF}\left(\varphi_{a_2}^{ZPF}\right)^2}{2!1!2!}$, see Appendix A.1 for the derivation.

The RWA Hamiltonian gives the interaction we want. This can be seen by considering what happens if we act with the Hamiltonian on the vacuum state $|n_{a_1}, n_b, n_{a_2}\rangle = |0,0,0\rangle$. The Hamiltonian then only populates the buffer mode with strength ζ^*, and as more time passes does the photon in the buffer mode, corresponding to state $|0,1,0\rangle$ turn into two photons in each of the SGM, *i.e.* $|0,1,0\rangle \to |2,0,2\rangle$. Now, due to the resonant drive of the buffer mode might we also occasionally get two photons in the buffer mode, but by ensuring that we have a sufficiently large dissipation rate of the buffer mode to the bath, κ_b, and sufficiently large coupling strength G is the chance of this occurring negligible.

The reason we want low population in the buffer mode is so we can approximate the buffer mode as a two-level system and adiabatically remove it, see Appendix A.2 for the derivation, and engineer a joint two-photon dissipation channel. After the adiabatic removal of the buffer mode, does the time-evolution of the density matrix take the form

$$\begin{aligned} \frac{\mathrm{d}}{\mathrm{d}t}\hat{\rho} =& -i\left[\frac{2G\zeta^* i}{\kappa_b}\hat{a}_1^2\hat{a}_2^2 - \frac{2G\zeta i}{\kappa_b}\hat{a}_1^{\dagger^2}\hat{a}_2^{\dagger^2}, \hat{\rho}\right] \\ &+ \frac{4G^2}{\kappa_b}\left(\hat{a}_1^2\hat{a}_2^2\hat{\rho}\hat{a}_1^{\dagger^2}\hat{a}_2^{\dagger^2} - \frac{1}{2}\left\{\hat{a}_1^{\dagger^2}\hat{a}_2^{\dagger^2}\hat{a}_1^2\hat{a}_2^2, \hat{\rho}\right\}\right) \end{aligned} \tag{2.56}$$

with the resulting equation being on the same form as Equation 2.25 with $g_{2,2} = \frac{2G\zeta^* i}{\kappa_b}$ and $\kappa = \frac{4G^2}{\kappa_b}$. The solutions then take the form

$$\alpha = \begin{cases} e^{i\frac{\pi}{4}}\sqrt[4]{\frac{\zeta}{G}} \\ e^{i\frac{5\pi}{4}}\sqrt[4]{\frac{\zeta}{G}} \\ e^{-i\frac{\pi}{4}}\sqrt[4]{\frac{\zeta}{G}} \\ e^{-i\frac{5\pi}{4}}\sqrt[4]{\frac{\zeta}{G}} \end{cases} . \tag{2.57}$$

We have now a circuit that generate the steady-states, but the question remains on how to choose the parameters in order to maximize the fidelity and the confinement rate towards the manifold spanned by our pair-cat states.

2.5 Calculating the Confinement Rates

We have previously shown that the zero-point fluctuations and eigenfrequencies are directly related to the geometric parameters of the circuit. As such will we work with the Hamiltonian directly when calculating the local convergence rate, κ_{conf}, to the manifold spanned by the pair-cat states. Note that from here one κ_{conf} will be referred to as the confinement rate. The calculation for the confinement rate will differ depending on whether the coherence value of the state, $|\alpha|$ is zero or not.

2.5.1 Confinement Rate for a General Non-Zero Coherence Value

Consider our Hamiltonian in the rotating wave approximation

$$\hat{\mathcal{H}} = G\left(\hat{a}_1^2\hat{a}_2^2 - {\alpha^*}^4\right)\hat{b}^\dagger + \text{h.c.} \tag{2.58}$$

where $\alpha^* = e^{\frac{i\pi}{4}}\sqrt[4]{\frac{\zeta^*}{G}}$. Using the Langevin equations [42], we get

$$\begin{cases} \dot{\hat{a}}_1 & = -2iG\hat{a}_1^\dagger{\hat{a}_2^\dagger}^2\hat{b} \\ \dot{\hat{b}} & = -iG\left(\hat{a}_1^2\hat{a}_2^2 - {\alpha^*}^4\right) - \frac{\kappa_b}{2}\hat{b} + \sqrt{\kappa_b}\hat{b}_{in} \\ \dot{\hat{a}}_2 & = -2iG{\hat{a}_1^\dagger}^2\hat{a}_2^\dagger\hat{b} \end{cases} \tag{2.59}$$

where $\hat{b}_{in}$ is the incoming bath field and the dot $(\cdot)$ denotes the time-derivative. If we furthermore assume the semiclassical approximation [43], in which we replace each operator with its expectation value and assume $\langle\hat{b}_{in}\rangle = 0$, we get

$$\begin{cases} \dot{a}_1 & = -2iGa_1^*{a_2^*}^2 b \\ \dot{b} & = -iG\left(a_1^2 a_2^2 - {\alpha^*}^4\right) - \frac{\kappa_b}{2}b \\ \dot{a}_2 & = -2iG{a_1^*}^2 a_2^* b \end{cases} \tag{2.60}$$

with stable points at

$$(a_1, b, a_2) = \left(0, \frac{2iG}{\kappa_b}{\alpha^*}^4, 0\right) \quad (a_1, b, a_2) = \left(\beta\alpha^*, 0, \frac{\alpha^*}{\beta}\right) \tag{2.61}$$

for $\beta \in \mathbb{C}_{/\{0\}}$. As we want to stabilize the pair-cat state with photons in the SGMs and an empty buffer mode will we ignore the dynamics around $(a_1, b, a_2) = \left(0, \frac{2iG}{\kappa_b}\alpha^{*^4}, 0\right)$ and focus on the other stable points.

The linearized dynamics at the stable points can be expressed as $\delta\,(a_1, b, a_2) = (a_1, b, a_2) - (a_{1_0}, b_0, a_{2_0})$ where (a_{1_0}, b_0, a_{2_0}) are the stable points. Which straightforwardly imply, $(a_1, b, a_2) = \delta\,(a_1, b, a_2) + (a_{1_0}, b_0, a_{2_0})$. For demonstrative purposes will we present the calculation for the linearized dynamics around the stable point of the a_1 mode and only present the results for the other modes.

Consider the a_1-mode. We then get

$$\begin{aligned}\dot{\delta a_1} = \dot{a_1} - \dot{a_{1_0}} &= -2iGa_1^* a_2^{*^2} b = -2iG\left(\delta a_1^* + \beta\alpha^*\right)\left(\delta a_2^* + \frac{\alpha^*}{\beta}\right)^2 \delta b \\ &\approx -2iG\frac{\alpha^{*^3}}{\beta}\delta b.\end{aligned} \tag{2.62}$$

We then get

$$\begin{cases}\dot{\delta a_1} = -2iG\frac{\alpha^3}{\beta^*}\delta b \\ \dot{\delta b} = -2iG\frac{\alpha^{*^3}}{\beta}\delta a_1 - 2iG\beta\alpha^{*^3}\delta a_2 - \frac{\kappa_b}{2}\delta b \\ \dot{\delta a_2} = -2iG\beta^*\alpha^3\delta b\end{cases}. \tag{2.63}$$

Furthermore, if we let $\delta a_j = x_{a_j} + iy_{a_j}$, for $j \in \{1, 2\}$ and $\delta b = x_b + iy_b$, then assuming β and α are both real, can we describe the linearized dynamics as a block matrix equation

$$\dot{v} = \begin{pmatrix} D & M \\ -M & D \end{pmatrix} v \tag{2.64}$$

where $v = \left(x_{a_1}, x_b, x_{a_2}, y_{a_1}, y_b, y_{a_2}\right)^T$ and

$$M = \begin{pmatrix} 0 & 2G\frac{\alpha^3}{\beta} & 0 \\ 2G\frac{\alpha^3}{\beta} & 0 & 2G\beta\alpha^3 \\ 0 & 2G\beta\alpha^3 & 0 \end{pmatrix} \quad D = \begin{pmatrix} 0 & 0 & 0 \\ 0 & -\frac{\kappa_b}{2} & 0 \\ 0 & 0 & 0 \end{pmatrix}.$$

Let $A = 2G\frac{\alpha^3}{\beta}$, $B = 2G\beta\alpha^3$. Then the characteristic polynomial is given by

$$\chi(\lambda) = \det\begin{pmatrix} \lambda - D & -M \\ M & \lambda - D \end{pmatrix} = \lambda^2\left(\left(\lambda + \frac{\kappa_b}{2}\right)\lambda + A^2 + B^2\right)^2 \tag{2.65}$$

and has the solutions

$$\begin{cases}\lambda_{1,2} = 0 \\ \lambda_{3,4} = -\frac{\kappa_b}{4}\left(1 - \sqrt{1 - \frac{64G^2\alpha^6(\beta^2+\beta^{-2})}{\kappa_b^2}}\right) = \lambda_- \\ \lambda_{5,6} = -\frac{\kappa_b}{4}\left(1 + \sqrt{1 - \frac{64G^2\alpha^6(\beta^2+\beta^{-2})}{\kappa_b^2}}\right) = \lambda_+\end{cases}. \tag{2.66}$$

Note that the real part of the eigenvalues are non-positive. As such can the fluctuations $\delta\left(a_1, b, a_2\right)$ are either constant or exponentially suppressed for all values of G, κ_b and α.

The solutions can then be divided into two regimes; the *underdamped* regime and the *overdamped* regime depending on whether the eigenvalues are real or complex [44]. The transition point occurs when

$$\frac{64G^2\alpha^6\left(\beta^2+\beta^{-2}\right)}{\kappa_b^2}=1. \tag{2.67}$$

In the case where $\kappa_b^2 > 64G^2\alpha^6\left(\beta^2+\beta^{-2}\right)$, we lie in the overdamped regime as the buffer decay is too strong and the confinement rate, κ_{conf}, is governed by the eigenvalue of least magnitude [44].

$$\kappa_{\text{conf}}\Big|^{\alpha\neq 0}_{\kappa_b^2>64G^2\alpha^6(\beta^2+\beta^{-2})}=-2\lambda_-=\frac{\kappa_b}{2}\left(1+\sqrt{1-\frac{64G^2\alpha^6\left(\beta^2+\beta^{-2}\right)}{\kappa_b^2}}\right). \tag{2.68}$$

A Taylor expansion of first order yields

$$\kappa_{\text{conf}}\Big|^{\alpha\neq 0}_{\kappa_b^2>64G^2\alpha^6(\beta^2+\beta^{-2})}=\frac{16G^2\alpha^6\left(\beta^2+\beta^{-2}\right)}{\kappa_b} \tag{2.69}$$

which, assuming we prepare our pair-cat state from vacuum, in turn yield

$$\kappa_{\text{conf}}\Big|^{\alpha\neq 0}_{\kappa_b^2>128G^2\alpha^6}=\frac{32G^2|\alpha|^6}{\kappa_b} \tag{2.70}$$

as the photon number difference between the modes are 0 [23].

In the case where $\kappa_b^2 < 64G^2|\alpha|^6\left(\beta^2+\beta^{-2}\right)$ are we in the underdamped regime as the buffer decay is too weak to remove all photons in the buffer mode. The confinement rate is then given by the shared real part of λ_+ and λ_- [44]. The confinement rate is then

$$\kappa_{\text{conf}}\Big|^{|\alpha|\neq 0}_{\kappa_b^2<64G^2|\alpha|^6(\beta^2+\beta^{-2})}=-2\Re\text{e}\left(\lambda_\pm\right)=\frac{\kappa_b}{2}. \tag{2.71}$$

There is therefore a maximum decay rate of $\frac{\kappa_b}{2}$ we want to reach, and the circuit parameters should be chosen such that

$$G\geq\sqrt{\frac{\kappa_b^2}{128|\alpha|^6}}. \tag{2.72}$$

This calculation of course, assumes that $|\alpha|\neq 0$. However, if we initialize a pure Fock state $|n_{a_1}, n_b, n_{a_2}\rangle$, or a holonomic gate is used then $|\alpha| = 0$ [45], and the calculated confinement rate no longer holds. The confinement rate would then need to be calculated another way.

2.5.2 Confinement Rate for a Coherence Value of 0

Consider the time-evolution of the density matrix in the RWA when no resonant drive is applied on the buffer mode, $\zeta = 0$,

$$\frac{\mathrm{d}}{\mathrm{d}t}\hat{\rho} = -i\left[G\left(\hat{a}_1^2\hat{a}_2^2\hat{b}^\dagger + \hat{a}_1^{\dagger 2}\hat{a}_2^{\dagger 2}\hat{b}\right), \hat{\rho}\right] + \kappa_b\left(\hat{b}\hat{\rho}\hat{b}^\dagger - \frac{1}{2}\left\{\hat{b}^\dagger\hat{b}, \hat{\rho}\right\}\right) \tag{2.73}$$

or in Liouvillian form

$$\frac{\mathrm{d}}{\mathrm{d}t}\hat{\rho} = \hat{\mathcal{L}}\hat{\rho} = \left(\mathbf{1}\otimes\mathbf{G}^* + \mathbf{G}\otimes\mathbf{1} + \kappa_b\mathbf{b}\otimes\mathbf{b}^*\right)\hat{\rho} \tag{2.74}$$

where

$$\mathbf{G} = -iG\left(\hat{a}_1^2\hat{a}_2^2\hat{b}^\dagger + \hat{a}_1^{\dagger 2}\hat{a}_2^{\dagger 2}\hat{b}\right) - \frac{\kappa_b}{2}\hat{b}^\dagger\hat{b} \tag{2.75}$$

and $\mathbf{1}$ is the unitary matrix [44].

If we let n_{a_1}, n_b, and n_{a_2} be the population in mode a_1, b, and a_2 respectively and consider the Fock state $|n_{a_1}, n_b, n_{a_2}\rangle$. Then for any $n \in \mathbb{N}$, can we immediately see that the states $|0,0,0\rangle$, $|n,0,0\rangle$, $|n,0,1\rangle$, $|1,0,1\rangle$, $|0,0,n\rangle$, $|1,0,n\rangle$ are steady states of Equation 2.73. Let $\mathcal{L}_0$ be the space spanned by these steady states. Then one can leave $\mathcal{L}_0$ by applying the operator $\hat{a}_1^\dagger\hat{a}_2^\dagger$ simultaneously. Consider for instance acting the operator $\hat{a}_1^\dagger\hat{a}_2^\dagger$ on state $|1,0,1\rangle$ then we obtain state $|2,0,2\rangle$ and exit the $\mathcal{L}_0$-space. However, this state will turn into $|0,1,0\rangle$ due to the presence of $G\hat{a}_1^2\hat{a}_2^2\hat{b}^\dagger$, which in turn will collapse into $|0,0,0\rangle$ due to the strong dissipation. We can then define the first excitation manifold, $\mathcal{L}_1$, as the smallest subspace invariant under the interaction dynamics $\mathbf{G}$, and contains all states obtained by a single simultaneous excitation of the storage modes from $\mathcal{L}_0$ and whose states are not already in $\mathcal{L}_0$. For instance the states $|2,0,2\rangle$, and $|0,1,0\rangle$ belong to $\mathcal{L}_1$, but $|1,0,1\rangle$ does not. We can also define the second excitation manifold, $\mathcal{L}_2$ in a similar manner.

It is then possible to estimate the space $\mathcal{L}$ the Liouvillian acts on as

$$\mathcal{L} = \bigoplus_{r,s=0}^{\ell} \mathcal{L}_r \otimes \mathcal{L}_s \tag{2.76}$$

with $\ell \to \infty$ yielding the exact space. Furthermore, note that $\mathbf{G}\mathcal{L}_i \subset \mathcal{L}_i$, $\mathbf{b}\mathcal{L}_i \subset \mathcal{L}_{i-1}$ with $\mathbf{G}\mathcal{L}_0 = 0$ and $\mathbf{b}\mathcal{L}_0 = 0$; which implies that $\mathcal{L}$ can be expressed as a block upper triangular matrix and we only need to consider the eigenvalues of $\mathbf{G}$ over the excitation manifolds [44]. Furthermore, it can be shown that $\mathbf{G}$ over the excitation manifold decomposes into independent invariant subspaces $\mathcal{V}_{n,m}^{(\ell)} = \mathrm{Span}\left(|n-2k, k, m-2k\rangle, k \in \{0,\ldots,\ell\}\right)$, when $\mathbf{G}$ acts on $\mathcal{L}_\ell$. These subspaces also satisfy one or more of the following equalities $n - 2\ell = 0$, $n - 2\ell = 1$, $m - 2\ell = 0$, or $m - 2\ell = 1$ by construction of the excitation manifolds.

Consider a state $|n,0,m\rangle \in \mathcal{L}_\ell$. The action of $\mathbf{G}$ on $|n,0,m\rangle$ is then

$$\mathbf{G}|n,0,m\rangle = -iG\sqrt{nm(n-1)(m-1)}\;|n-2,1,m-2\rangle. \tag{2.77}$$

Similarly,

$$\begin{aligned}\mathbf{G}|n-2,1,m-2\rangle =& - iG\sqrt{2(n-2)_2(m-2)_2}|n-4,2,m-4\rangle \\ & - iG\sqrt{(n)_2(m)_2}\;|n,0,m\rangle \\ & - \frac{\kappa_b}{2}|n-2,1,m-2\rangle.\end{aligned} \tag{2.78}$$

where $(x)_2 = x(x-1)$ and is known as a falling factorial [46]. For a general state $|n-2k,k,m-2k\rangle \in \mathcal{L}_\ell$ where $0<k<\ell$, we have

$$\begin{aligned}\mathbf{G}|n-2k,k,m-2k\rangle =& - iGN_k^{(n,m)}|n-2(k+1),k+1,m-2(k+1)\rangle \\ & - iGN_{k-1}^{(n,m)}|n-2(k-1),k-1,m-2(k-1)\rangle \\ & - \frac{\kappa_b}{2}k|n-2k,k,m-2k\rangle.\end{aligned} \tag{2.79}$$

where $N_k^{(n,m)} = \sqrt{(k+1)(n-2k)_2(m-2k)_2}$. Finally, for the case where $k=\ell$, we have

$$\begin{aligned}\mathbf{G}|n-2\ell,\ell,m-2\ell\rangle =& - iGN_{\ell-1}^{(n,m)}|n-2(\ell-1),\ell-1,m-2(\ell-1)\rangle \\ & - \frac{\kappa_b}{2}\ell|n-2\ell,\ell,m-2\ell\rangle.\end{aligned} \tag{2.80}$$

Hence $\mathbf{G}$ leaves the subspace $\mathcal{V}_{n,m}^{(\ell)}$ invariant. It remains to show that no coupling exists between distinct subspaces $\mathcal{V}_{n,m}^{(\ell)}$ and $\mathcal{V}_{n',m'}^{(\ell)}$ with $(n,m)\neq(n',m')$.

Suppose there exists a non-zero matrix element connecting $|n_{a_1},n_b,n_{a_2}\rangle$ to a state in $\mathcal{V}_{n',m'}^{(\ell)}$. By construction of the interaction term, such a coupling would require the simultaneous application of the operators $\hat{a}_1^2\hat{a}_2^2\hat{b}^\dagger$ or $\hat{a}_1^{\dagger 2}\hat{a}_2^{\dagger 2}\hat{b}$, which change the occupation numbers according to

$$(n_{a_1},n_b,n_{a_2}) \mapsto (n_{a_1}\pm 2, n_b \mp 1, n_{a_2}\pm 2) \in \mathcal{V}_{n,m}^{(\ell)}. \tag{2.81}$$

Thus, any path generated by repeated application of $\mathbf{G}$ starting in $\mathcal{V}_{n,m}^{(\ell)}$ remains entirely within $\mathcal{V}_{n,m}^{(\ell)}$, and cannot reach $\mathcal{V}_{n',m'}^{(\ell)}$. This establishes that all subspaces $\mathcal{V}_{n,m}^{(\ell)}$ are mutually invariant and dynamically disconnected.

Finally, since each invariant subspace $\mathcal{V}_{n,m}^{(\ell)}$ is $(\ell+1)$-dimensional, the restriction of $\mathbf{G}$ to $\mathcal{L}_\ell$ decomposes into a direct sum of independent $(\ell+1)\times(\ell+1)$ tridiagonal matrices,

$$\mathbf{G}\Big|_{\mathcal{L}_\ell} \simeq \bigoplus_{n,m}\mathbf{G}_{n,m}^{(\ell)}, \tag{2.82}$$

with

$$\mathbf{G}_{n,m}^{(\ell)} = \begin{pmatrix} 0 & -iGN_0^{(n,m)} & 0 & \cdots & 0 \\ -iGN_0^{(n,m)} & -\frac{\kappa_b}{2} & -iGN_1^{(n,m)} & \cdots & 0 \\ 0 & -iGN_1^{(n,m)} & -\kappa_b & \cdots & 0 \\ \vdots & \vdots & \vdots & \ddots & -iGN_{\ell-1}^{(n,m)} \\ 0 & 0 & 0 & -iGN_{\ell-1}^{(n,m)} & -\frac{\kappa_b}{2}\ell \end{pmatrix}. \tag{2.83}$$

Note that the confinement rate will be $\kappa_{\text{conf}} = -2\Re\text{e}\left(\lambda_{\min}\right)$ where $\lambda_{\min}$ is the eigenvalue with the smallest non-zero real part in absolute value [44]. Also note that for the matrix presented in Equation 2.83 does the terms increase monotonically with n, m and k, which increases the size of the eigenvalue. The term with the lowest eigenvalue is then the lowest possible combination of n, m that lies on an excitation manifold, and is $(n, m) = (2, 2)$ which corresponds to the space $\mathcal{V}_{2,2}^{(1)} \subset \mathcal{L}_1$.

Rather then decomposing into a tridiagonal matrix does the restriction of $\mathbf{G}$ to $\mathcal{L}_1$ decompose it into a direct sum of independent 2×2 matrices

$$\mathbf{G}\Big|_{\mathcal{L}_1} \simeq \bigoplus_{n,m} \mathbf{G}_{n,m}^{(1)}, \tag{2.84}$$

with

$$\mathbf{G}_{n,m}^{(1)} = \begin{pmatrix} 0 & -iG\sqrt{nm(n-1)(m-1)} \\ -iG\sqrt{nm(n-1)(m-1)} & -\frac{\kappa_b}{2} \end{pmatrix}. \tag{2.85}$$

To obtain the eigenvalues for $\mathbf{G}$ over $\mathcal{L}_1$, we then only need to consider the eigenvalues of Equation 2.85, which are

$$\lambda_{\pm}^{n,m} = -\frac{\kappa_b}{4}\left(1 \pm \sqrt{1 - \frac{16nm(n-1)(m-1)G^2}{\kappa_b^2}}\right). \tag{2.86}$$

Specifically for $(n, m) = (2, 2)$ we have

$$\lambda_{\pm}^{2,2} = -\frac{\kappa_b}{4}\left(1 \pm \sqrt{1 - \frac{64G^2}{\kappa_b^2}}\right). \tag{2.87}$$

In the overdamped regime, where $\kappa_b > 8G$, we have a confinement rate of

$$\kappa_{\text{conf}}\Big|_{\kappa_b > 8G}^{|\alpha|=0} = \frac{\kappa_b}{4}\left(1 - \sqrt{1 - \frac{64G^2}{\kappa_b^2}}\right) \tag{2.88}$$

which saturates at $\kappa_{\text{conf}} = \frac{\kappa_b}{2}$ as $G \to \frac{\kappa_b}{8}$. In the underdamped regime, where $8G > \kappa_b$, we obtain

$$\kappa_{\text{conf}}\Big|_{\kappa_b < 8G}^{|\alpha|=0} = -2\Re\text{e}\left(\lambda_{\pm}\right) = \frac{\kappa_b}{2}. \tag{2.89}$$

The circuit parameters should therefore be chosen such that $G > \frac{\kappa_b}{8}$, as that both maximizes the confinement rate for when $|\alpha| = 0$ and satisfies Equation 2.72 for $|\alpha| \geq \frac{1}{\sqrt[6]{2}} \approx 0.89$.

2.6 Quantum Computing Gate Set

In quantum computing, a gate set said to be universal if any universal operation can be approximated to an arbitrary degree using only the gates from said set [47]. Finding one of these set is however not enough for quantum computing to be justified, as we also need the code that we want to simulate to not be efficiently computable on a classical computer. In other words, we want our set to fail the Gottesmann-Knill theorem [25]. What this means in practice is that we need at least one gate that does not belong in the Clifford group, which is the normalizer of the group consisting of Pauli matrices [48]. To construct a universal gate set can we, as a starting point, use the gates presented in [7] and can be seen in Table 2.1.

Hamiltonian X-gate	$\hat{\mathcal{H}}_X = g_x \left(\hat{a}_1^\dagger \hat{a}_2^\dagger + \hat{a}_1 \hat{a}_2\right)$
Hamiltonian XX-gate	$\hat{\mathcal{H}}_{XX} = g_{XX} \left(\hat{a}_1^\dagger \hat{c}_1^\dagger \hat{a}_2^\dagger \hat{c}_2^\dagger + \hat{a}_1 \hat{c}_1 \hat{a}_2 \hat{c}_2\right)$
Holonomic Z-gate	$\alpha \to 0 \to \alpha e^{i\phi} \to \alpha.$

Table 2.1: Suggested gate set.

Here the letters a and c denotes different qubits and the indexed numbers denote the different state generating modes (SGM) of the qubit. Please note that the two qubit gate is outside the scope of the Thesis, but is presented here for convenience. The first two gates were first presented in [9], and the third gate in [45], all for a single cat state and extended by Albert *et al.* in [7] for pair-cat states. Note that the Holonomic gate will not affect the dynamics of the system, unless the qubit is initialized in a superposition of $|0\rangle_L$ and $|1\rangle_L$ as $|0\rangle_L$ then picks up a relative phase of $2\theta_2$ with regards to $|1\rangle$ through the Berry phase [45]. Regardless, whichever gate is used does the state rotate around the Bloch sphere.

2.6.1 Bloch Sphere

The Bloch sphere is a geometrical representation of a two-level quantum state [47], and is presented in Figure 2.5.

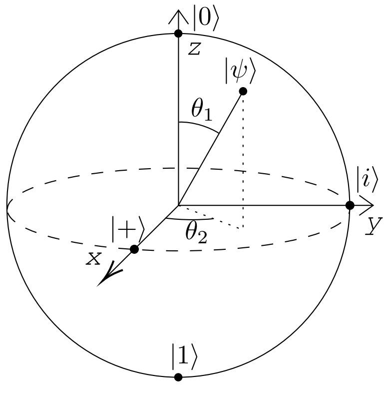

Figure 2.5: Sketch of the Bloch sphere. A two level quantum state $|\psi\rangle$ is completely determined by the angles θ_1 and θ_2 according to $|\psi\rangle = \cos\left(\frac{\theta_1}{2}\right)|0\rangle + e^{i\theta_2}\sin\left(\frac{\theta_1}{2}\right)|1\rangle$.

The state is completely determined by $|\psi\rangle = \cos\left(\frac{\theta_1}{2}\right)|0\rangle + e^{i\theta_2}\sin\left(\frac{\theta_1}{2}\right)|1\rangle$ where $\langle 0|1\rangle = 0$. We can then define a gate for a rotation around each of the principal axis. If we define $|0\rangle = \begin{pmatrix}1\\0\end{pmatrix}$ and $|1\rangle = \begin{pmatrix}0\\1\end{pmatrix}$ then we can define the following gates

$$\hat{X} = |0\rangle\langle 1| + |1\rangle\langle 0| = \begin{pmatrix}0 & 1\\1 & 0\end{pmatrix} \tag{2.90}$$

$$\hat{Y} = i|1\rangle\langle 0| - i|0\rangle\langle 1| = \begin{pmatrix}0 & -i\\i & 0\end{pmatrix} \tag{2.91}$$

$$\hat{Z} = |0\rangle\langle 0| - |1\rangle\langle 1| = \begin{pmatrix}1 & 0\\0 & -1\end{pmatrix} \tag{2.92}$$

These have the eigenstate $|\pm\rangle = \frac{|0\rangle \pm |1\rangle}{\sqrt{2}}$ for the $\hat{X}$-matrix, $|\pm i\rangle = \frac{|0\rangle \pm i|1\rangle}{\sqrt{2}}$ for the $\hat{Y}$-matrix and $|1\rangle$ and $|0\rangle$ for the $\hat{Z}$-matrix.

Applying for instance a X-gate on the qubit rotates the state depend on the time the gate is active and its strength according to

$$\hat{R}_x(t)|\psi\rangle = e^{i\frac{\tilde{g}_x}{2}t\hat{X}}|\psi\rangle \tag{2.93}$$

where $|\psi\rangle$ is the qubits initial state, t is the time the gate is active and $\tilde{g}_x$ is the strength of the gate [47]. The time it takes for the gate to implement a whole rotation is $t_{\text{rot}} = \frac{2\pi}{\tilde{g}_x}$.

Consider for instance the X-gate presented in Table 2.1. If we want to apply the X-rotation, then we want the resulting code to still be in the code subspace spanned by $|\alpha_\delta\rangle$ and $|i\alpha_\delta\rangle$, but the new time-evolution of the density matrix would be on the form

$$\begin{aligned}\frac{\mathrm{d}}{\mathrm{d}t}\hat{\rho} = & -i\left[g_{2,2}\hat{a}_1^2\hat{a}_2^2 - g_{2,2}^*\hat{a}_1^{\dagger^2}\hat{a}_2^{\dagger^2} + g_x\hat{a}_1^\dagger\hat{a}_2^\dagger + g_x\hat{a}_1\hat{a}_2, \hat{\rho}\right] \\ & + \frac{\kappa}{2}\left(2\hat{a}_1^2\hat{a}_2^2\hat{\rho}\hat{a}_1^{\dagger^2}\hat{a}_2^{\dagger^2} - \left\{\hat{a}_1^{\dagger^2}\hat{a}_2^{\dagger^2}\hat{a}_1^2\hat{a}_2^2, \hat{\rho}\right\}\right)\end{aligned} \tag{2.94}$$

then if g_x is comparable or much larger than $g_{2,2}$ we would stabilize another state entirely and work against our stabilization process.

2.6.2 Proving the X-gate

The X-gate can be engineered by driving the buffer mode with a frequency of $\omega_X = \omega_{a_1} - \omega_b + \omega_{a_2}$; the derivation of which can be found in Appendix B. This subchapter proves that the gate works and for which values of α it does work.

To prove that

$$\hat{\mathcal{H}}_X = g_x\left(\hat{a}_1^\dagger\hat{a}_2^\dagger + \hat{a}_1\hat{a}_2\right) \tag{2.95}$$

acts as an X-gate on our code subspace can we define the projector of said code subspace [7]. The projector of our code subspace is

$$\hat{P} = |\psi_{\alpha_\delta}^+\rangle\langle\psi_{\alpha_\delta}^+| + |\psi_{\alpha_\delta}^-\rangle\langle\psi_{\alpha_\delta}^-| = \hat{P}^\dagger. \tag{2.96}$$

Projecting our $\hat{a}_1\hat{a}_2$ operator onto the code subspace, we get

$$\hat{P}\hat{a}_1\hat{a}_2\hat{P} = \frac{|\alpha|^2}{\sqrt{\left(I_\delta\left(2|\alpha|^2\right)\right)^2 - \left(J_\delta\left(2|\alpha|^2\right)\right)^2}}\left(I_\delta\left(2|\alpha|^2\right)\hat{X} + iJ_\delta\left(2|\alpha|^2\right)\hat{Y}\right) \tag{2.97}$$

which means that for a real g_x the effect the X-gate has on the code is described by the following equation

$$\begin{aligned} g_x\hat{P}\left(\hat{a}_1^\dagger\hat{a}_2^\dagger + \hat{a}_1\hat{a}_2\right)\hat{P}^\dagger = \frac{g_x}{\sqrt{N_X}}&\left(\left(\Re\mathrm{e}\left(\alpha\right)^2 - \Im\mathrm{m}\left(\alpha\right)^2\right)I_\delta\left(2|\alpha|^2\right)\hat{X}\right.\\ &\left.-2\Re\mathrm{e}(\alpha)\Im\mathrm{m}(\alpha)J_\delta\left(2|\alpha|^2\right)\hat{Y}\right) \end{aligned} \tag{2.98}$$

where

$$N_X = \frac{\left(I_\delta\left(2|\alpha|^2\right)\right)^2 - \left(J_\delta\left(2|\alpha|^2\right)\right)^2}{4}. \tag{2.99}$$

Note that rotations purely around the X-axis only occur for either purely real or purely imaginary α and it does so with an effective gate strength $\tilde{g}_x$ where

$$|\tilde{g}_x| = \frac{2g_x|\alpha|^2}{\sqrt{\left(I_\delta\left(2|\alpha|^2\right)\right)^2 - \left(J_\delta\left(2|\alpha|^2\right)\right)^2}}I_\delta\left(2|\alpha|^2\right) \tag{2.100}$$

or in the large $|\alpha|$ limit; $|\tilde{g}_x| = 2g_x|\alpha|^2$.

3

Results

In this chapter, are the results presented. We will first show the result for the induced joint two photon decay, and then show how the strength of the circuit parameters and the strength of the resonant drive of the buffer mode affect the fidelity of the generated. Afterwards, will we show the state preparation of both the RWA and using the full Hamiltonian as well as the X-gate for the RWA. The X-gate has not been implemented for the full Hamiltonian but a quick discussion will be held on how to effectively realize the gate in a future work.

3.1 Induced Joint Two Photon Decay

Recall the effective time-evolution of the density matrix for our system, presented in Equation 2.56, and rewritten here for convenience

$$\begin{aligned}\frac{\mathrm{d}}{\mathrm{d}t}\hat{\rho} = &-i\left[\frac{2G\zeta^* i}{\kappa_b}\hat{a}_1^2\hat{a}_2^2 - \frac{2G\zeta i}{\kappa_b}\hat{a}_1^{\dagger^2}\hat{a}_2^{\dagger^2}, \hat{\rho}\right] \\ &+ \frac{4G^2}{\kappa_b}\left(\hat{a}_1^2\hat{a}_2^2\hat{\rho}\hat{a}_1^{\dagger^2}\hat{a}_2^{\dagger^2} - \frac{1}{2}\left\{\hat{a}_1^{\dagger^2}\hat{a}_2^{\dagger^2}\hat{a}_1^2\hat{a}_2^2, \hat{\rho}\right\}\right),\end{aligned} \tag{3.1}$$

then if the resonant drive on the buffer mode is turned off, *i.e.* $\zeta = 0$, we only have the joint two-photon dissipator left. The new time-evolution of the system is then

$$\frac{\mathrm{d}}{\mathrm{d}t}\hat{\rho} = \frac{4G^2}{\kappa_b}\left(\hat{L}\hat{\rho}\hat{L}^\dagger - \frac{1}{2}\left\{\hat{L}^\dagger\hat{L}, \hat{\rho}\right\}\right) \tag{3.2}$$

where $\hat{L} = \hat{a}_1^2\hat{a}_2^2$ and describes the dissipation [30]. For a state prepared in Fock state $|n, 0, m\rangle$, we expect the induced photon decay to continue until either $n - 2 < 0$ or $m - 2 < 0$. Here the central index corresponds to the buffer mode, the leftmost index to the a_1 mode and the rightmost index to the a_2 mode.

Consider for instance what happens when we initialize a state in $|2, 0, 2\rangle$, and uses the parameters presented in Table 3.1.

Table 3.1: Parameters used when modelling the decay rate of the state initialized in $|2,0,2\rangle$. The resonant drive on the buffer mode, ζ, was turned off during the simulation.

$\varphi_{a_1}^{ZPF}$	0.38	ω_{a_1}	4.08 GHz $\times 2\pi$
φ_{b}^{ZPF}	0.39	ω_{b}	7.90 GHz $\times 2\pi$
$\varphi_{a_2}^{ZPF}$	0.58	ω_{a_2}	5.21 GHz $\times 2\pi$
E_{J_1}	5.60 GHz $\times h$	E_{J_2}	5.60 GHz $\times h$
κ_b	2.40 MHz $\times 2\pi$	$\lvert\zeta\rvert$	-

In order to show the decay was the projection of the initial state against the $|2,2\rangle$ and $|0,0\rangle$ Fock states plotted. Here we ignore the central index as we are only interested in the decay of the two state-generating modes. The result of which is shown in Figure 3.1. The confinement rate was then obtained by fitting the data against $P_{22} = e^{-\kappa_{\text{conf}} t}$, where P_{22} is the projection against the $|2,2\rangle$ state. The result of the fitting, together with the analytical solution is presented in Figure 3.2.

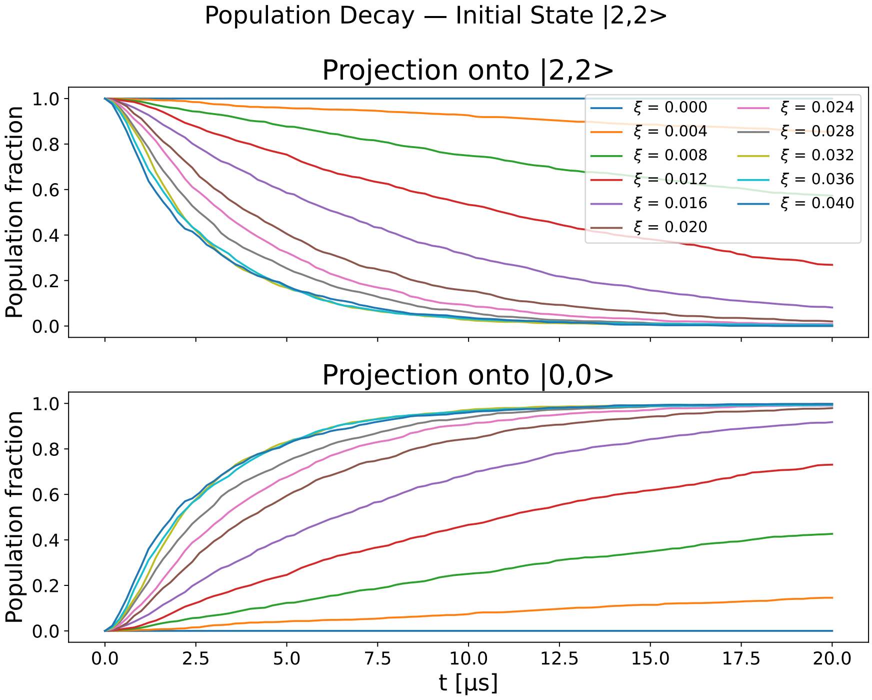

Figure 3.1: Population decay. The state is initialized with two photons in each mode. No photon decay occur when the magnetic flux between the arms of the ATS is turned off. As the flux gets stronger, we observe a stronger decay and it is likelier and likelier to measure no photons in the cavity.

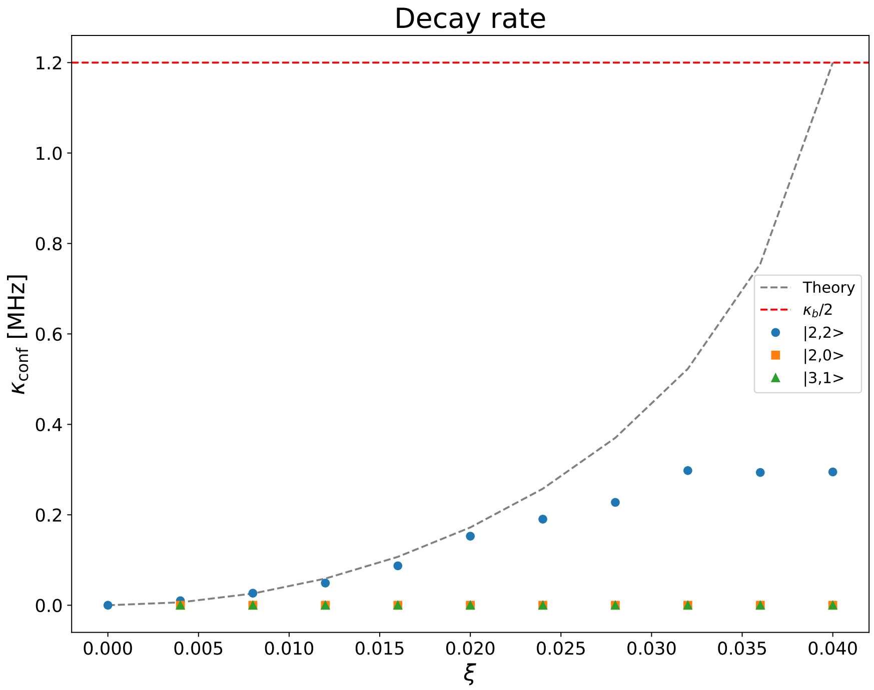

Figure 3.2: Fitted decay rate when initialized in different Fock states. The blue dots corresponds to the fitted decay rate for when the state was initialized in $|2, 0, 2\rangle$, the orange squares when the state was initialized in $|2, 0, 0\rangle$ and the green triangles when the state was initialized in $|3, 0, 1\rangle$. The grey line is the analytically obtained decay rate for $|2, 0, 2\rangle$ and the red dashed line is the theoretical maximum value of $\kappa_b/2$. The fastest confinement rate is obtained at $\xi = 0.032$, but deviate from the theory.

The fitted decay rate in Figure 3.2, when the state is initialized in Fock state $|2, 0, 2\rangle$ matches the analytical decay rate in the beginning, but starts to deviate more and more as the strength of the external magnetic flux increases. One explanation is that the RWA is not a good description for our system when using strong pumps, even if it can give some idea on how the system acts. This is not entirely unexpected since the leading order of the RWA is on the fifth order and there may exist near resonant terms on a lower order, which can influence the result. However, the interaction Hamiltonian, $G\left(\hat{a}_1^2\hat{a}_2^2\hat{b}^\dagger + \text{h.c.}\right)$ is key to initialize the pair-cat states. As such should the pump strength chosen to be as strong as possible, while still allowing the RWA to give a good description of the system. From Figure 3.2 can we observe that the RWA fail to describe the system when $\xi > 0.25$ and as such was a pump strength of $\xi = 0.02485$ chosen for the following results.

For the process where we initialized the state as $|2, 0, 0\rangle$ and $|3, 0, 1\rangle$, we observe no decay. This is expected since both $|2, 0, 0\rangle$ and $|3, 0, 1\rangle$ belong in $\mathcal{L}_0$ while $|2, 0, 2\rangle$ belong in $\mathcal{L}_1$.

The larger Fock state we initialize our system in, the faster the observed decay rate is. This is because of Equation 3.2, and we get that the $\{\hat{L}^\dagger\hat{L},\hat{\rho}\}$ term dominates when $\hat{\rho}$ is initialized in $\hat{\rho}=|n,0,m\rangle\langle n,0,m|$ for large values of n and m. For large values of n and m and for stronger Josephson energies, we also observe ”kicks” in the decay as the old mode gets repopulated. A possible explanation is that for the larger Josephson energies the term in front of the sine of the fluctuations, $E_\Sigma \sin\left(\xi\cos(\omega_d t)\right)$, become too large and we get an effective drive on the buffer mode which invalidates the adiabatic removal of the buffer mode. Another possible explanation is that for both the larger n and m as well as the larger Josephson energies does additional near-resonance terms no longer become negligible and might affect the dynamic of the system in terms of a feedback loop, but further studies need to be performed in order to observe what causes the ”kicks”.

The result for the population decay of the state initialized in $|2,0,0\rangle$, $|2,0,2\rangle$, $|3,0,1\rangle$, $|3,0,2\rangle$, $|3,0,3\rangle$, $|4,0,4\rangle$, $|5,0,2\rangle$, $|5,0,3\rangle$, $|5,0,4\rangle$, $|5,0,5\rangle$, $|6,0,6\rangle$, $|7,0,2\rangle$, $|7,0,3\rangle$, $|7,0,4\rangle$, $|7,0,5\rangle$, $|7,0,6\rangle$, $|7,0,7\rangle$, and $|8,0,8\rangle$ is presented in Appendix C.

3.2 Plotting the Fidelity

Even if the induced joint two photon decay for $|\alpha|=0$ is not maximized, can we still achieve the maximized confinement rate towards the spanned manifold for non-zero α as long as $G\geq\frac{\kappa_b}{\sqrt{128|\alpha|^6}}$. Furthermore, maximizing the joint two photon decay for $\alpha=0$, hinders what value of $|\alpha|$ we can safely construct using our circuit. Consider the case where we desire a pair-cat state with a pair-coherence value of $|\alpha|=2$; then since $|\alpha|\approx\sqrt[4]{\frac{\zeta}{G}}$ can we apply a resonant drive on the buffer mode with strength $|\zeta|\approx 16G$. This occurs at the same time as the coupling strength G satisfies $G\geq\frac{\kappa_b}{8}$ and we get $|\zeta|\geq 2\kappa_b$. The buffer mode then risks getting repopulated faster than it empties and the approximation of adiabatically removing the buffer mode no longer holds. This may potentially yield issues when implementing the holonomic Z-gate but more studies need to performed in order to establish any potential issues.

In order for the adiabatic removal of the buffer mode to remain valid, we suggest to construct the circuit such that it satisfies $\frac{\kappa_b}{8}\gg G>\frac{\kappa_b}{\sqrt{128|\alpha|^6}}$, as it then maximizes the decay rate for the pair-cat states while also allowing for $\kappa_b\gg|\zeta|$ to hold. For $|\alpha|\geq 1.95$, have we plotted the fidelity of the resulting states in Figure 3.3, together with our suggested maximum and minimum limit.

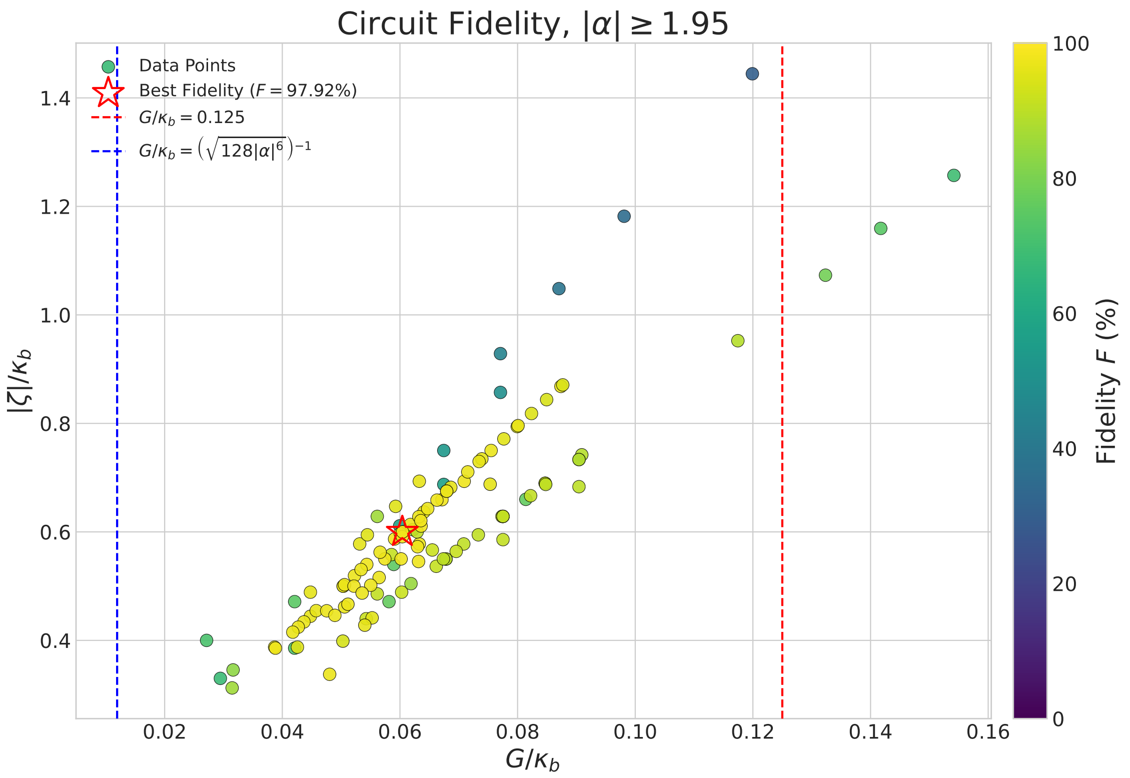

Figure 3.3: The fidelity for different circuit parameters, resonant drive, and decay rate of the buffer mode that all result in giving a pair-cat state of $|\alpha| \geq 2$. The brighter the data point the greater the fidelity. The highest fidelity is 97.92% and marked by a star. The blue dashed line correspond to the lowest vale of $\frac{G}{\kappa_b}$ that maximizes the confinement rate of the pair-cat state when $|\alpha| \geq 1.95$. The red dashed line corresponds to the lowest value of $\frac{G}{\kappa_b}$ that maximizes the confinement rate when $|\alpha| = 0$. The states with the highest fidelities lies in the middle section of the two dashed lines.

The state with the highest fidelities all lie in the predicted regime. With the highest fidelity state having the parameters presented in Table 3.2.

Table 3.2: Parameters used obtaining the state with the highest fidelity. The pump strength of the magnetic fluxes was chosen to be $|\epsilon(t)| = 0.02485$. The coherence value is $|\alpha| = 2$ with a fidelity of 97.92%.

$\varphi_{a_1}^{ZPF}$	0.36	ω_{a_1}	4.11 GHz $\times 2\pi$
φ_{b}^{ZPF}	0.34	ω_{b}	6.18 GHz $\times 2\pi$
$\varphi_{a_2}^{ZPF}$	0.39	ω_{a_2}	4.40 GHz $\times 2\pi$
E_{J_1}	3.96 GHz $\times h$	E_{J_2}	3.96 GHz $\times h$
κ_b	2.25 MHz $\times 2\pi$	$\|\zeta\|$	1.35 MHz $\times 2\pi$

3.3 Plotting the stabilization Time

All the states need some time to get initialized. In order to get as many simulations as possible, we want to minimize the stabilization time. For each data point simulated was the stabilization time recorded and plotted against the coherence parameter, $|\alpha|$, see Figure 3.4, and the reduced gate strength, $\frac{G}{\kappa_b}$, see Figure 3.5. We also plotted the estimated stabilization time against the reduced Josephson energies $\frac{E_{\Sigma}\xi}{\kappa_b}$, see Figure 3.6. For all of the above mentioned plots were only the states with a fidelity between 96% to 98% considered.

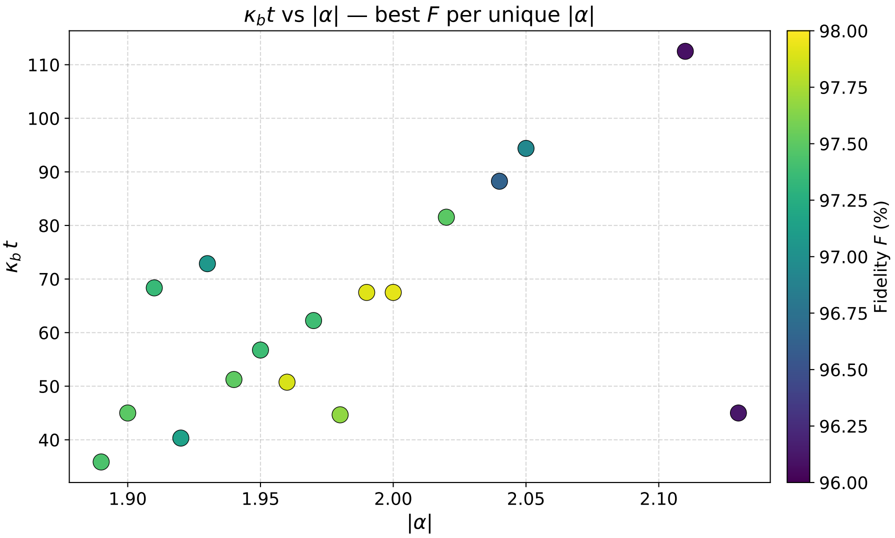

Figure 3.4: Plot of the estimated dimensionless stabilization time against the coherence value. If two states had been prepared in a pair-cat state with coherence value α_0 then only the state with the best fidelity was chosen. Furthermore, only fidelities between 96% and 98% were considered. The dimensionless time varies between 35 to 115, with a linear dependence on the pair-coherence value.

From Figure 3.4 can we observe a general linear increase in estimated stabilization time, proportional to the absolute value of the pair-coherence value. The fidelity does not seem to be affecting the estimated stabilization time.

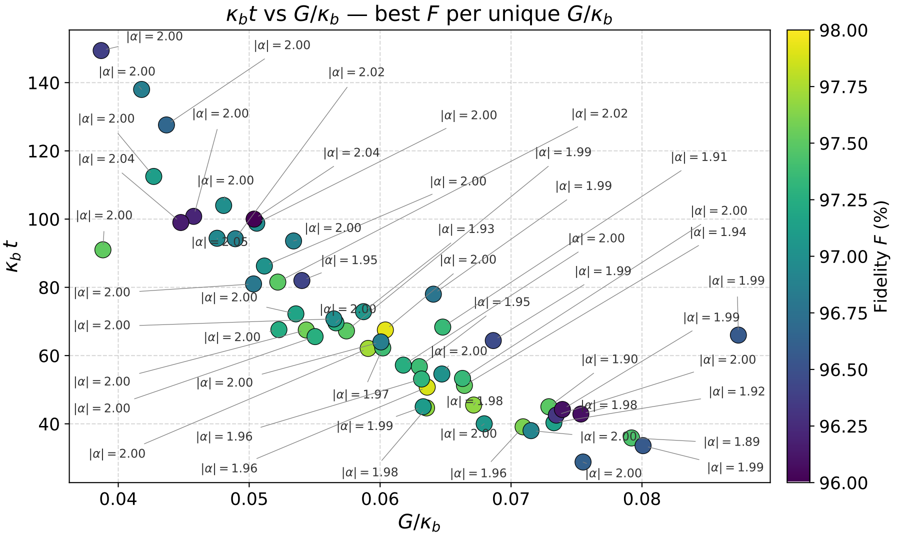

Figure 3.5: Plot of the estimated dimensionless stabilization time vs the reduced gate strength used. If two states were initialized with the same reduced gate strength, then the state with the highest fidelity was chosen. Furthermore, only fidelities between 96% and 98% were considered. The dimensionless time varies between 30 to 150 with the estimated dimensionless stabilization decreasing with the increased gate strength.

We observe a decrease in estimated stabilization time for larger values of the reduced gate strength. For low values of ξ is $G \propto E_\Sigma \xi$ and we should expect faster stabilization time for stronger Josephson junctions. The result is presented in Figure 3.6.

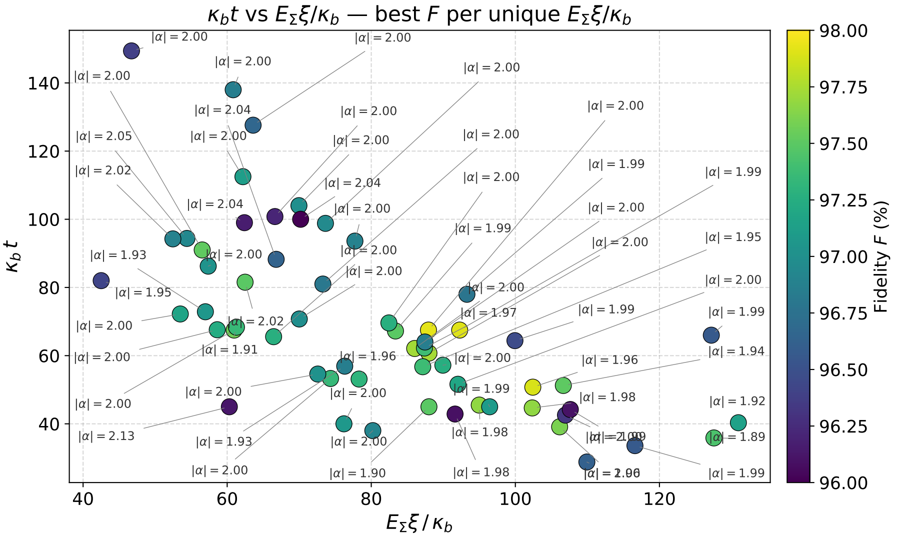

Figure 3.6: The estimated dimensionless stabilization time plotted against the reduced strength of the Josephson junctions. For stronger Josephson junctions, we observe a faster estimated stabilization time.

From Figure 3.6 can we observe that the dimensionless stabilization time reduces with the reduced strength of the Josephson junction, but not as fast as it does with the reduced gate strength, see Figure 3.5. Increasing E_Σ reduces the stabilization time, but a more effective method is increasing the zero-point fluctuations as the gate strength is given by

$$G = \frac{E_\Sigma \xi}{2} e^{-\frac{\left\|\varphi^{ZPF}\right\|^2}{2}} \frac{\left(\varphi_{a_1}^{ZPF}\right)^2 \varphi_b^{ZPF} \left(\varphi_{a_2}^{ZPF}\right)^2}{2!1!2!} \tag{3.3}$$

and have a maxima at $\left(\varphi_{a_1}^{ZPF}, \varphi_b^{ZPF}, \varphi_{a_2}^{ZPF}\right) = \left(\sqrt{2}, 1, \sqrt{2}\right)$. This, however, can affect the fidelity of the state as if we exit the stable region of the zero-point fluctuations, the fidelity can plummet quite quickly, see Figure 3.7.

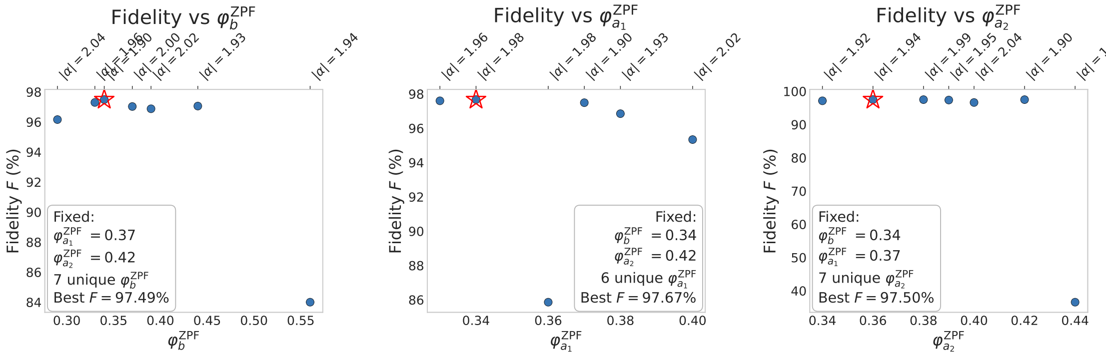

Figure 3.7: Comparison of the fidelity when slightly changing the zero-point fluctuation for the different modes. Each point plotted is also simulated with a different ζ value in order to obtain a similar coherent state. The decay rate is also different in order to keep the effective decay rate $\frac{4G^2}{\kappa_b}$ constant. The fidelity remains mostly unchanged when changing the zero-point fluctuations; but for large zero-point fluctuations does it quickly deteriorate.

3.4 State stabilization and Operation

The quantum states need to both be initialized and operated. In this section will we present the result for the state stabilization in both the rotating picture and for the full Hamiltonian. We will also present the the X-gate in the rotating frame, and discuss how it can be extended for the full Hamiltonian.

3.4.1 Using the Rotating Wave Approximation

Initializing the state using the parameters presented in Table 3.2, we obtain populations presented in Figure 3.8.

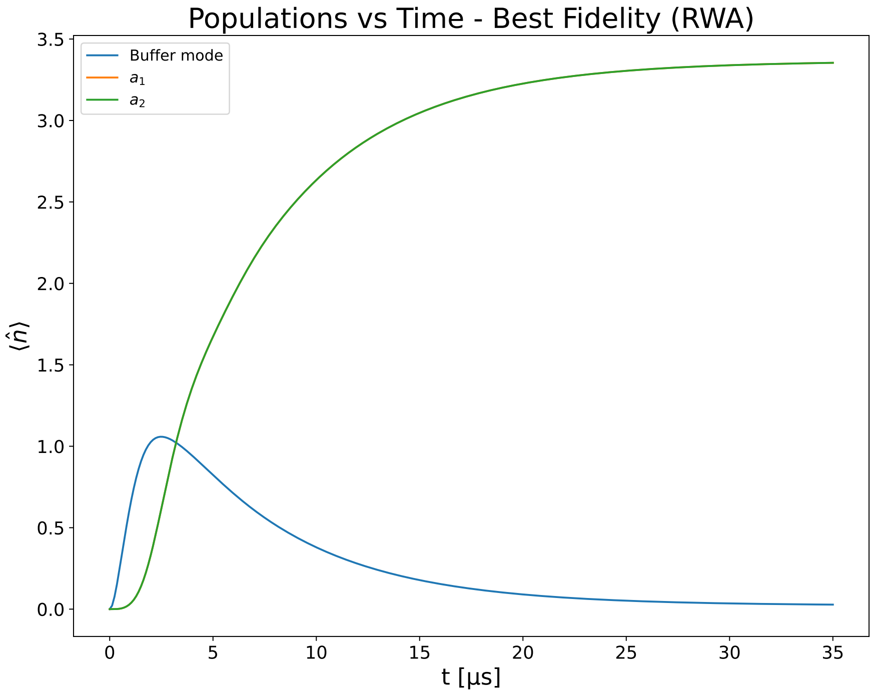

Figure 3.8: Population plot of the different modes for the state with the highest fidelity, using the RWA. The a_1 mode has the same population as the a_2 mode at all times. The a_2 mode is therefore plotted over the population of the a_1 mode, hiding the population of the mode in this graph. The buffer mode population increases rapidly in the beginning, and maximizes with an average population of 1.058 photons, at 2.45 µs after the stabilization process has begun, before starting to decay. The population of the state generating modes follow an exponential increase and reaches the steady state after an estimated 30 µs with the average population of 3.53.

The state has a fidelity of 98.14%, with a pair-coherence value of $|\alpha| = 1.90$.

If we instead use the parameters presented in Table 3.1, with $|\zeta| = 1.91$ MHz, we obtain the population plot presented in Figure 3.9.

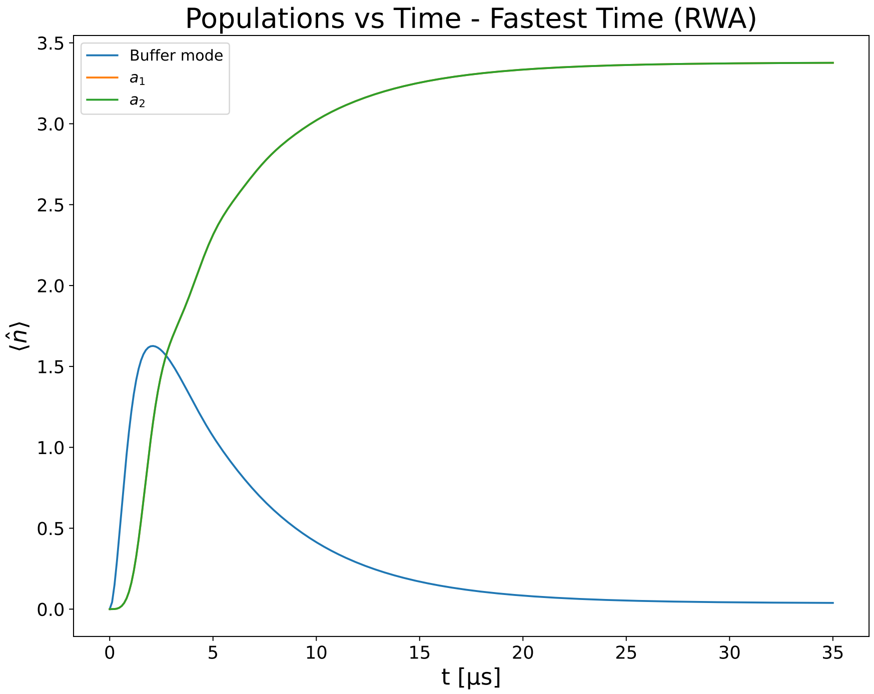

Figure 3.9: Population plot of the different modes for the state with the fastest estimated stabilization time, using the RWA. The a_1 mode has the same population as the a_2 mode at all times. The a_2 mode is therefore plotted over the population of the a_1 mode, hiding the population of the mode in this graph. The buffer mode population increases rapidly in the beginning, and maximizes with an average population of 1.627 photons, at 2.10 μs after the stabilization process has begun, before starting to decay. The population of the state generating modes follow an exponential increase and reaches the steady state after an estimated 24 μs with the average population of 3.38.

The RWA then predicts a state with pair-coherence parameter of $|\alpha| = 1.91$ and a fidelity of 98.13%.

However it is not enough to only initialize the state, but we also need to perform rotations. For instance consider applying the X-gate rotation with a gate strength $|g_x| = 0.27$ MHz on a state fully initialized in the even pair-cat state with $|\alpha| = 1.90$; see Figure 3.10.

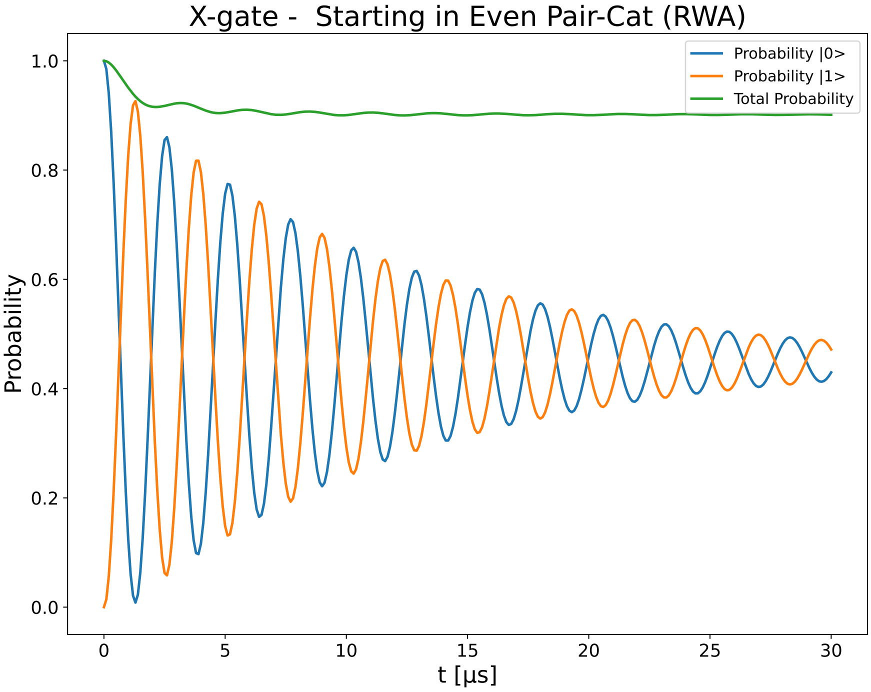

Figure 3.10: X-gate rotation of a state initialized in the even pair-cat state. A rotation occur when the probability to measure the odd pair-cat state ($|1\rangle$) reaches its peak and the probability to measure the even pair-cat state ($|0\rangle$) reaches the bottom. The total probability of measuring either state $|0\rangle$ or $|1\rangle$ is also included. A total probability of less than 1 means we have obtained a mixed state. A single rotation takes 1.30 µs and leaves the state with a fidelity of 93.74%.

A single rotation takes 1.30 µs and if we turn off the gate after 1.30 µs, we obtain the odd pair-cat state with a fidelity of 93.74%, as seen in Figure 3.11. The total state is $|\psi\rangle = 0.0032|0\rangle + (0.0033 - 1i)\,|1\rangle$ with a fidelity of 99.07%.

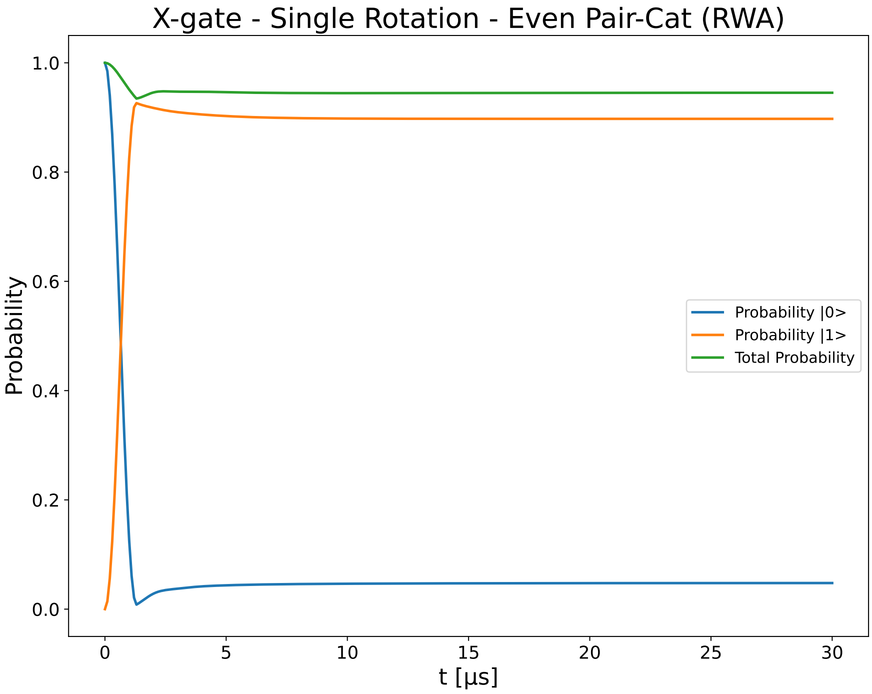

Figure 3.11: Probability to measure either the even pair-cat state ($|0\rangle$) or the odd pair-cat state ($|1\rangle$), when the X-gate is active in 1.30 µs. The total probability of measuring either state $|0\rangle$ or $|1\rangle$ is also included. A total probability of less than 1 means that we have a mixed state. The final state is $|\psi\rangle = 0.0033|0\rangle + (-0.0198 - 0.9998i)\,|1\rangle$ with a fidelity of 99.07%.

If the gate and the state stabilization process is initiated at the same time then we obtain the result presented in Figure 3.12.

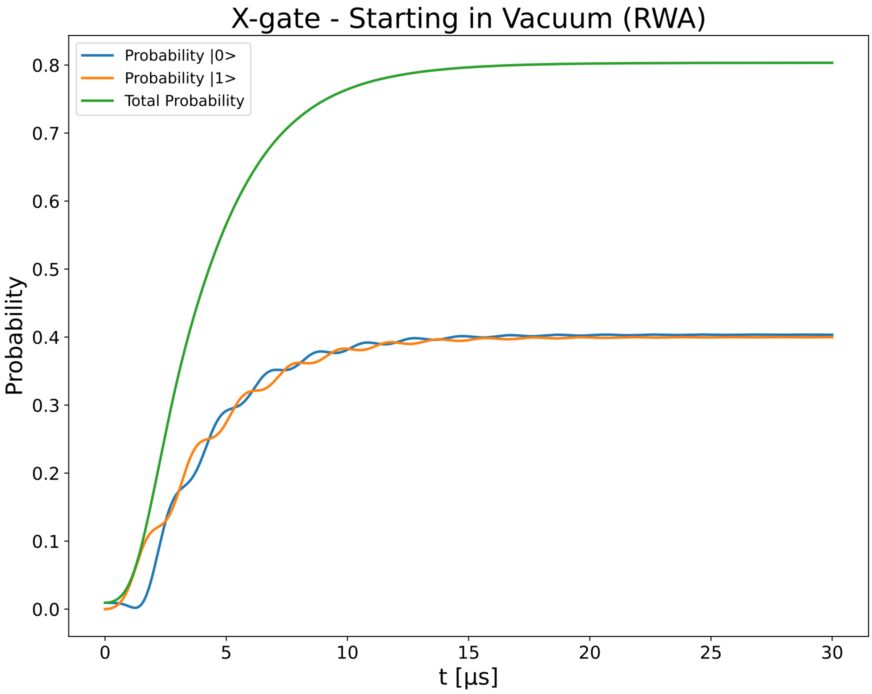

Figure 3.12: X-gate rotation together with the stabilization process on the vacuum state. A rotation occur when the probability to measure the odd pair-cat state ($|1\rangle$) reaches its peak and the probability to measure the even pair-cat state ($|0\rangle$) reaches the bottom. The total probability of measuring either state $|0\rangle$ or $|1\rangle$ is also included. A total probability of less than 1 mean that we have a mixed state. The stabilization is the dominating process and the X-gate has managed to turn the steady-state into a mixed state. The final state has a fidelity of 46.31%.

Turning the gate off after once again 1.30 µs, we obtain the result presented in Figure

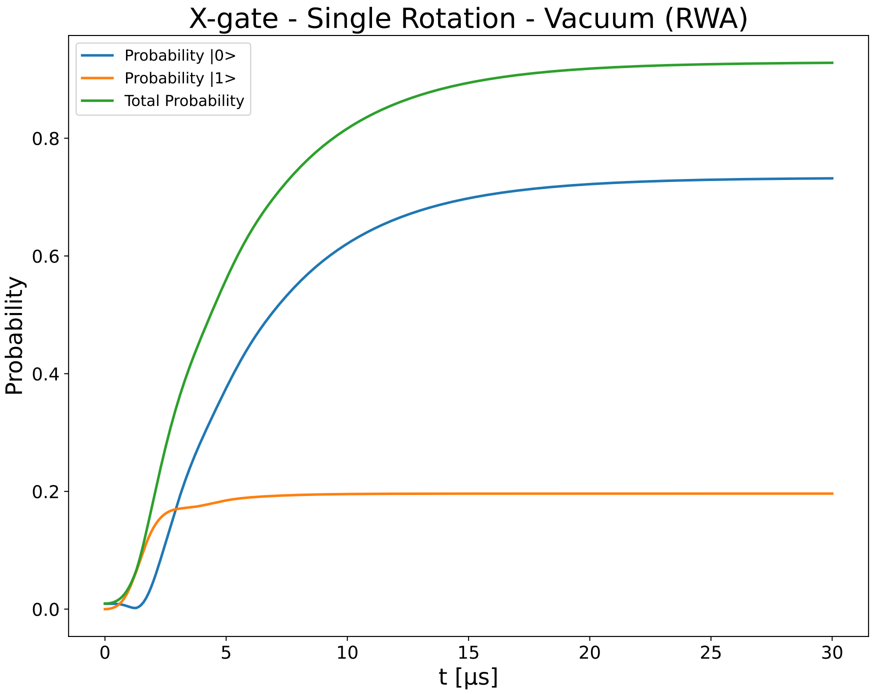

Figure 3.13: X-gate rotation together with the stabilization process. The X-gate is turned off after 1.30 µs. The final state is $|\psi\rangle = 0.9652|0\rangle + 0.2614i|1\rangle$, with a fidelity of 89.70%. The stabilization process, converts a photon from the buffer mode into the two photons in each mode of the state-generation modes, with no coupling to the odd pair-cat state. The result, is then what we observe in the graph, with it initializing the even pair-cat again.

As the fidelity is better, and we have a slow stabilization process, we suggest to first initialize the state in the even pair-cat state and then apply the X-gate in order to perform rotations around the X-axis.

The X-gate works as a proof of concept in the rotating frame but is hard to implement in the full Hamiltonian. Recall the definition of g_x

$$g_x = \frac{\varphi_{a_1}^{ZPF}\varphi_b^{ZPF}\varphi_{a_2}^{ZPF}}{2\left(\omega_{a_1}+\omega_{a_2}-2\omega_b\right)} E_\Sigma \xi \zeta_X e^{-\frac{\left\|\varphi^{ZPF}\right\|^2}{2}}. \tag{3.4}$$

To achieve the gate presented in Figures 3.10 and 3.12, we apply a coherent drive on the buffer mode with $\zeta_X = 269.7$ MHz; which can be hard to implement. Fortunately, there exists other parameters we can change to obtain a larger value of g_x and achieve a faster gate. The key to realize what parameters to increase is to recall the time-evolution of the density matrix presented in Equation 2.94, but rewritten here for convenience

$$\begin{aligned}\frac{\mathrm{d}}{\mathrm{d}t}\hat{\rho} =& -i\left[g_{2,2}\hat{a}_1^2\hat{a}_2^2 - g_{2,2}^*\hat{a}_1^{\dagger^2}\hat{a}_2^{\dagger^2} + g_x\hat{a}_1^\dagger\hat{a}_2^\dagger + g_x\hat{a}_1\hat{a}_2, \hat{\rho}\right] \\ &+ \frac{\kappa}{2}\left(2\hat{a}_1^2\hat{a}_2^2\hat{\rho}\hat{a}_1^{\dagger^2}\hat{a}_2^{\dagger^2} - \left\{\hat{a}_1^{\dagger^2}\hat{a}_2^{\dagger^2}\hat{a}_1^2\hat{a}_2^2, \hat{\rho}\right\}\right).\end{aligned} \tag{3.5}$$

Then in order to stabilize the pair-cat state we need $|g_{2,2}| \gg |g_x|$, where $g_{2,2} = \frac{2G\zeta^* i}{\kappa_b}$, then since both g_x and $|g_{2,2}|$ increase linearly with E_Σ and φ_b^{ZPF} can we increase those two values more than we decrease ζ_X to increase, or fix the ratio of $\frac{|g_{2,2}|}{g_x}$ while we at the same time shorten the rotation time $t_{\text{rot}} = \frac{2\pi}{\tilde{g}_x}$.

3.4.2 Using the Full Hamiltonian

The state generation for the highest fidelity can be observed in Figure 3.14, and uses the same parameters presented in Table 3.2.

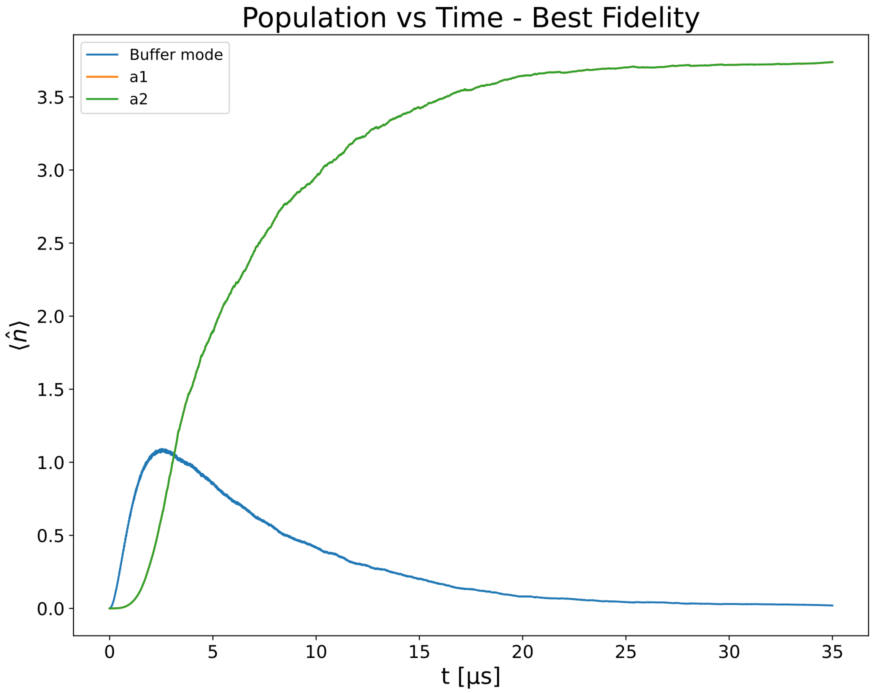

Figure 3.14: Population plot of the different modes when the state is initialized. The a_1 mode has the same population as the a_2 mode at all times. The a_2 mode is therefore plotted over the population of the a_1 mode, hiding the population of the mode in this graph. The buffer mode population increases rapidly in the beginning, and maximizes with an average population of 1.09 photons, at 2.52 µs after the stabilization process has begun, before starting to decay. The population of the state generating modes follow an exponential increase and reaches the steady state after an estimated 30 µs with the average population of 3.74.

The state has a fidelity of 97.92%, which is slightly lower than what the RWA predicts in Figure 3.8. Furthermore, does the RWA predict a pair-coherence value of $|\alpha| = 1.90$ while the full Hamiltonian predicts a pair-coherence value of $|\alpha| = 2.00$. A similar decrease in fidelity and increase in the pair-coherence value can be seen for the state with the parameters for the fastest found stabilization time, see Figure 3.15.

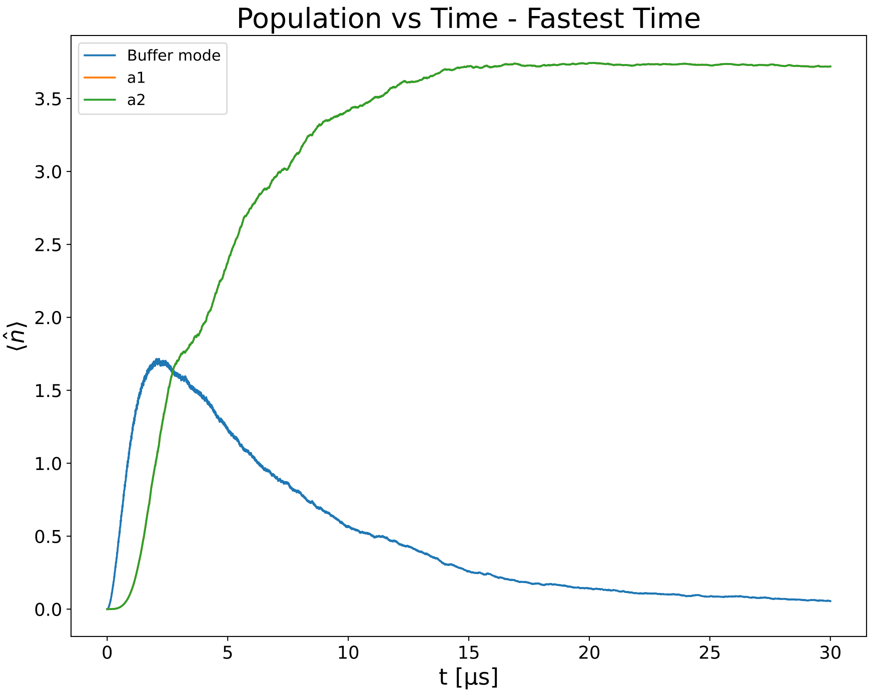

Figure 3.15: Population plot of the different modes when the state is initialized using the parameters that gave the fastest stabilization time. The a_1 mode has the same population as the a_2 mode at all times. The a_2 mode is therefore plotted over the population of the a_1 mode, hiding the population of the mode in this graph. The buffer mode population increases rapidly in the beginning, and maximizes with an average population of 1.72 photons, at 2.15 μs after the stabilization process has begun, before starting to decay. The population of the state generating modes follow an exponential increase and reaches the steady state after an estimated 14 μs with the average population of 3.72.

Here we also observe a drop in fidelity, while also observing an increase of the pair-coherent value. For the full Hamiltonian we obtain $|\alpha| = 1.99$, with a fidelity of 96.56%.

A reason for the discrepancy between the full Hamiltonian and the Hamiltonian in the rotating picture, is that the rotating wave approximation cannot fully describe the system. For instance, in the full picture we have additional terms of $\sin(\epsilon(t))\varphi_b^{ZPF}\left(\hat{b}^\dagger + \hat{b}\right)$ and equivalent terms for the other modes, that cannot be captured in the rotating picture. These terms, if near resonance, could contribute to an effective drive on each of the mode and result in a state with a larger pair-coherence value. This can also explain the faster estimated stabilization time for the result presented in Figure 3.15 compared to when using the RWA, see Figure 3.9.

4

Conclusion & Outlook

We have demonstrated that that it is possible to generate pair-cat states with $|\alpha| \geq 1.95$ and a high fidelity of 97.72%. These states however, have a long stabilization time. We have also shown that we can induce a joint two-photon decay, and that it is challenging to maximize the joint two-photon decay rate while stabilizing a pair-cat state at the same time. For holonomic gates, which require $|\alpha| = 0$ during the process is the confinement rate not maximized, and more studies is required in order to establish if this causes any trouble for the gate. Furthermore, have we shown that the pair-coherence value $|\alpha|$ can be modified by tuning the strength of the resonant drive $|\zeta|$, as $|\alpha| \propto \sqrt[4]{\frac{\zeta}{G}}$. Finally, the nature of the circuit only allows for certain combinations of eigenfrequencies and zero-point fluctuations since the impedance of the circuit is only allowed to have real roots.

The stabilization time can be sped up but at the cost of the fidelity. Furthermore, we have shown that the X-gate can be implemented in the RWA, but for the full Hamiltonian would we require a large coherent drive on the buffer mode which might not be feasible. Both the problem of the slow stabilization time and the large coherent drive on the buffer mode for the X-gate can be solved by increasing the energy of the Josephson junctions. This however, comes at the cost of the fidelity. Another possible way to increase the stabilization time might be to implement a counter-adiabatic drive, which might be of interest to implement in future studies.

Additionally, might it be of interest to implement the holonomic Z-gate in future studies. Enabling the encoding and manipulation of arbitrary quantum information within the pair-cat logical basis.

Furthermore, in future studies might it also be relevant to simulate the effect of noise since that is not present in these studies. Additionally, the confinement rate assumes the RWA is valid, but near-resonant terms may contribute and explain the deviated confinement rate from the measured confinement rate. In future studies, might it therefore be of interest to extend the RWA to the second or third order and compare the new theoretical value to the measured data.

Bibliography

[1] M. Kira, S. W. Koch, R. P. Smith, A. E. Hunter, and S. T. Cundiff. Quantum spectroscopy with Schrödinger-cat states. *Nature Physics*, 7(10):799–804, October 2011.

[2] A. P. Lund, T. C. Ralph, and H. L. Haselgrove. Fault-tolerant linear optical quantum computing with small-amplitude coherent states. *Physical Review Letters*, 100(3):030503, January 2008. arXiv:0707.0327 [quant-ph].

[3] Andrew M. Steane and Ben Ibinson. Fault-Tolerant Logical Gate Networks for CSS Codes. *Physical Review A*, 72(5):052335, November 2005. arXiv:quant-ph/0311014.

[4] Kosuke Fukui and Shuntaro Takeda. Building a large-scale quantum computer with continuous-variable optical technologies. *Journal of Physics B: Atomic, Molecular and Optical Physics*, 55(1):012001, January 2022.

[5] Demid V. Sychev, Alexander E. Ulanov, Anastasia A. Pushkina, Matthew W. Richards, Ilya A. Fedorov, and Alexander I. Lvovsky. Enlargement of optical Schrödinger's cat states. *Nature Photonics*, 11(6):379–382, June 2017.

[6] Daniel Gottesman, Alexei Kitaev, and John Preskill. Encoding a qubit in an oscillator. *Physical Review A*, 64(1):012310, June 2001.

[7] Victor V Albert, Shantanu O Mundhada, Alexander Grimm, Steven Touzard, Michel H Devoret, and Liang Jiang. Pair-cat codes: autonomous error-correction with low-order nonlinearity. *Quantum Science and Technology*, 4(3):035007, June 2019.

[8] Zaki Leghtas, Gerhard Kirchmair, Brian Vlastakis, Robert J. Schoelkopf, Michel H. Devoret, and Mazyar Mirrahimi. Hardware-Efficient Autonomous Quantum Memory Protection. *Physical Review Letters*, 111(12):120501, September 2013.

[9] Mazyar Mirrahimi, Zaki Leghtas, Victor V Albert, Steven Touzard, Robert J Schoelkopf, Liang Jiang, and Michel H Devoret. Dynamically protected cat-

qubits: a new paradigm for universal quantum computation. *New Journal of Physics*, 16(4):045014, April 2014.

[10] Ming Yuan, Qian Xu, and Liang Jiang. Construction of bias-preserving operations for pair-cat codes. *Physical Review A*, 106(6):062422, December 2022.

[11] A. Vanselow, B. Beauseigneur, L. Lattier, M. Villiers, A. Denis, P. Morfin, Z. Leghtas, and P. Campagne-Ibarcq. Dissipating Quartets of Excitations in a Superconducting Circuit. *Physical Review X*, 16(1):011032, February 2026.

[12] Navin A. R. Bhat and J. E. Sipe. Hamiltonian treatment of the electromagnetic field in dispersive and absorptive structured media. *Physical Review A*, 73(6):063808, June 2006.

[13] S.E. Rasmussen, K.S. Christensen, S.P. Pedersen, L.B. Kristensen, T. Bækkegaard, N.J.S. Loft, and N.T. Zinner. Superconducting Circuit Companion—an Introduction with Worked Examples. *PRX Quantum*, 2(4):040204, December 2021.

[14] B.D. Josephson. Possible new effects in superconductive tunnelling. *Physics Letters*, 1(7):251–253, July 1962.

[15] A. A. Golubov, M. Yu. Kupriyanov, and E. Il'ichev. The current-phase relation in Josephson junctions. *Reviews of Modern Physics*, 76(2):411–469, April 2004.

[16] Leon N. Cooper. Bound Electron Pairs in a Degenerate Fermi Gas. *Physical Review*, 104(4):1189–1190, November 1956.

[17] M. R. Schafroth. Superconductivity of a Charged Ideal Bose Gas. *Physical Review*, 100(2):463–475, October 1955.

[18] Oliver Penrose and Lars Onsager. Bose-Einstein Condensation and Liquid Helium. *Physical Review*, 104(3):576–584, November 1956.

[19] Carlos Ramírez and Chumin Wang. Towards a theory of superconductivity based on collective Cooper pairs. *Journal of Physics and Chemistry of Solids*, 72(5):395–397, May 2011.

[20] Roy J. Glauber. Coherent and Incoherent States of the Radiation Field. *Physical Review*, 131(6):2766–2788, September 1963.

[21] C. C. Gerry and P. L. Knight. Quantum superpositions and Schrödinger cat states in quantum optics. *American Journal of Physics*, 65(10):964–974, October 1997.

[22] A. O. Barut and L. Girardello. New "Coherent" States associated with non-

compact groups. *Communications in Mathematical Physics*, 21(1):41–55, March 1971.

[23] G. S. Agarwal. Nonclassical statistics of fields in pair coherent states. *Journal of the Optical Society of America B*, 5(9):1940, September 1988.

[24] Karl Blum. *Density Matrix Theory and Applications.* Number 64 in Springer Series on Atomic, Optical, and Plasma Physics. Springer Berlin Heidelberg, Berlin, Heidelberg, 3rd ed. 2012 edition, 2012.

[25] Daniel Gottesman. The Heisenberg Representation of Quantum Computers, July 1998. arXiv:quant-ph/9807006.

[26] Carlos Alexandre Brasil, Felipe Fernandes Fanchini, and Reginaldo de Jesus Napolitano. A simple derivation of the Lindblad equation. 2011. Version Number: 2.

[27] Marco Merkli. Dynamics of Open Quantum Systems II, Markovian Approximation. *Quantum*, 6:616, January 2022.

[28] Daniel Manzano. A short introduction to the Lindblad master equation. *AIP Advances*, 10(2):025106, February 2020.

[29] E. Huffman, D. Banerjee, S. Chandrasekharan, and U.-J. Wiese. Real-time evolution of strongly coupled fermions driven by dissipation. *Annals of Physics*, 372:309–319, September 2016.

[30] Patrick M. Harrington, Erich J. Mueller, and Kater W. Murch. Engineered dissipation for quantum information science. *Nature Reviews Physics*, 4(10):660–671, August 2022.

[31] Raphaël Lescanne, Marius Villiers, Théau Peronnin, Alain Sarlette, Matthieu Delbecq, Benjamin Huard, Takis Kontos, Mazyar Mirrahimi, and Zaki Leghtas. Exponential suppression of bit-flips in a qubit encoded in an oscillator. *Nature Physics*, 16(5):509–513, May 2020.

[32] Ronald M. Foster. A Reactance Theorem. *Bell System Technical Journal*, 3(2):259–267, April 1924.

[33] Simon E. Nigg, Hanhee Paik, Brian Vlastakis, Gerhard Kirchmair, S. Shankar, Luigi Frunzio, M. H. Devoret, R. J. Schoelkopf, and S. M. Girvin. Black-Box Superconducting Circuit Quantization. *Physical Review Letters*, 108(24):240502, June 2012.

[34] Luca Callegaro. *Electrical impedance: principles, measurement, and applications.* Series in sensors. CRC Press, Boca Raton, online-ausg edition, 2013.

[35] Bertrand I. Halperin, Gil Refael, and Eugene Demler. RESISTANCE IN SUPERCONDUCTORS. *International Journal of Modern Physics B*, 24(20n21):4039–4080, August 2010.

[36] Charles Kittel. *Introduction to solid state physics.* Wiley, Hoboken, NJ, global edition, [9th edition] edition, 2018.

[37] Emil M. Prodanov. On the cubic equation with its Siebeck–Marden–Northshield triangle and the quartic equation with its tetrahedron. *Journal of Computational Science*, 73:102123, November 2023.

[38] Ėrnest B. Vinberg. *A course in algebra.* Number volume 56 in Graduate Studies in Mathematics. American Mathematical Society, Providence, Rhode Island, 2003.

[39] Romeo Ortega, Antonio Loría, Per Johan Nicklasson, and Hebertt J. Sira Ramírez. *Passivity-based Control of Euler-Lagrange Systems: Mechanical, Electrical and Electromechanical Applications.* Communications and Control Engineering. Springer, London, 1998.

[40] A. A. Clerk, M. H. Devoret, S. M. Girvin, Florian Marquardt, and R. J. Schoelkopf. Introduction to quantum noise, measurement, and amplification. *Reviews of Modern Physics*, 82(2):1155–1208, April 2010.

[41] Alexandru Petrescu, Camille Le Calonnec, Catherine Leroux, Agustin Di Paolo, Pranav Mundada, Sara Sussman, Andrei Vrajitoarea, Andrew A. Houck, and Alexandre Blais. Accurate Methods for the Analysis of Strong-Drive Effects in Parametric Gates. *Physical Review Applied*, 19(4), April 2023.

[42] Alexandre Blais, Arne L. Grimsmo, S.M. Girvin, and Andreas Wallraff. Circuit quantum electrodynamics. *Reviews of Modern Physics*, 93(2):025005, May 2021.

[43] M V Berry and K E Mount. Semiclassical approximations in wave mechanics. *Reports on Progress in Physics*, 35(1):315–397, January 1972.

[44] U. Réglade, A. Bocquet, R. Gautier, J. Cohen, A. Marquet, E. Albertinale, N. Pankratova, M. Hallén, F. Rautschke, L.-A. Sellem, P. Rouchon, A. Sarlette, M. Mirrahimi, P. Campagne-Ibarcq, R. Lescanne, S. Jezouin, and Z. Leghtas. Quantum control of a cat qubit with bit-flip times exceeding ten seconds. *Nature*, 629(8013):778–783, May 2024.

[45] Victor V. Albert, Chi Shu, Stefan Krastanov, Chao Shen, Ren-Bao Liu, Zhen-Biao Yang, Robert J. Schoelkopf, Mazyar Mirrahimi, Michel H. Devoret, and Liang Jiang. Holonomic Quantum Control with Continuous Variable Systems. *Physical Review Letters*, 116(14):140502, April 2016.

[46] Manjul Bhargava. The Factorial Function and Generalizations. *The American Mathematical Monthly*, 107(9):783–799, November 2000.

[47] Michael A. Nielsen and Isaac L. Chuang. *Quantum Computation and Quantum Information: 10th Anniversary Edition*. Cambridge University Press, 1 edition, June 2012.

[48] Huangjun Zhu, Richard Kueng, Markus Grassl, and David Gross. The Clifford group fails gracefully to be a unitary 4-design, September 2016. arXiv:1609.08172 [quant-ph].

[49] Heinz-Peter Breuer and Francesco Petruccione. *The Theory of Open Quantum Systems*. Oxford University PressOxford, 1 edition, January 2007.

[50] Florentin Reiter and Anders S. Sørensen. Effective operator formalism for open quantum systems. *Physical Review A*, 85(3):032111, March 2012.

[51] Richard P. Feynman. An Operator Calculus Having Applications in Quantum Electrodynamics. *Physical Review*, 84(1):108–128, October 1951.

[52] Roy J. Glauber. Some Notes on Multiple-Boson Processes. *Physical Review*, 84(3):395–400, November 1951.

A

Calculations regarding the Rotating Wave Hamiltonian

In this appendix, we derive both the Hamiltonian in the rotating frame as well as adiabatically remove the buffer mode.

A.1 Deriving the Rotating Wave Hamiltonian

The key idea in the Rotating Wave Approximation (RWA) is that when measuring over a large period time will the effect of the quickly oscillating terms on average be 0. While this approximation will be done on both the time-dependent and time-independent terms is the effect on the time-independent term trivial and this subsection will therefore focus on the time-dependent terms As a reminder is the time-dependent terms are $E_\Sigma \sin\left(\xi \cos\left(\omega_d t\right)\right) \sin\left(\hat{\varphi}\right)$ where $\hat{\varphi} = \sum_p \varphi_p^{ZPF}\left(\hat{p} + \hat{p}^\dagger\right)$. The RWA is done in two steps. First we transform the Hamiltonian into the interaction picture

$$\hat{\mathcal{H}}_{\text{int}}^{(1)} = \hat{R}^\dagger(t)\hat{\mathcal{H}}\hat{R}(t) - i\hbar\hat{R}^\dagger(t)\frac{\mathrm{d}\hat{R}}{\mathrm{d}t} \tag{A.1}$$

with $\hat{R}(t) = e^{-\frac{i}{\hbar}\hat{\mathcal{H}}_0 t}$, and $\hat{\mathcal{H}}_0 = \sum_p \hbar\omega_p \hat{p}^\dagger\hat{p}$ and then we eliminate the quickly oscillating terms through a time-averaging operation [41]. The time-averaging operation is defined as

$$\overline{\hat{O}} = \lim_{T\to\infty}\frac{1}{T}\int_0^T \mathrm{d}t\hat{O}(t). \tag{A.2}$$

For small values of the magnetic flux, *i.e* $\xi \ll 1$, we approximate the time-dependent Hamiltonian $\hat{\mathcal{H}}_{\text{time}}$, as

$$\begin{aligned}\hat{\mathcal{H}}_{\text{time}} &= E_\Sigma \sin\left(\xi\cos\left(\omega_d t\right)\right)\sin\left(\hat{\varphi}\right) \\ &\approx E_\Sigma\left(\frac{\left(8\xi - \xi^3\right)}{8}\cos\left(\omega_d t\right) - \frac{\xi^3}{24}\cos\left(3\omega_d t\right)\right)\sin\left(\hat{\varphi}\right).\end{aligned} \tag{A.3}$$

Utilizing $\hat{R}^\dagger(t)\hat{R}(t) = 1$ is it possible to expand the sine term and apply the operators inside the function. In other words

$$\begin{aligned}\hat{R}^\dagger(t)\sin\left(\hat{\varphi}\right)\hat{R}(t) =& \hat{R}^\dagger(t)\hat{\varphi}\hat{R}(t) - \frac{\hat{R}^\dagger(t)\hat{\varphi}\hat{R}(t)\hat{R}^\dagger(t)\hat{\varphi}\hat{R}(t)\hat{R}^\dagger(t)\hat{\varphi}\hat{R}(t)}{3!}\\ &+ \mathcal{O}\left(\left(\hat{R}^\dagger(t)\hat{\varphi}\hat{R}(t)\right)^5\right)\\ =& \sin\left(\hat{R}^\dagger(t)\hat{\varphi}\hat{R}(t)\right)\end{aligned} \tag{A.4}$$

with $\hat{R}^\dagger(t)\hat{a}_1\hat{R}(t) = \hat{a}_1 e^{-i\omega_{a_1}t}$ and similar for $\hat{b}$ and $\hat{a}_2$. Furthermore, expanding $\sin(x+y+z)$ as

$$\begin{aligned}\sin\left(x+y+z\right) =& \sin(x)\cos(y)\cos(z) + \cos(x)\sin(y)\cos(z)\\ &+ \cos(x)\cos(y)\sin(z) - \sin(x)\sin(y)\sin(z)\end{aligned} \tag{A.5}$$

and rewriting $\sin(x) = \frac{1}{2i}\left(e^{ix} - e^{-ix}\right)$, and $\cos(x) = \frac{1}{2}\left(e^{ix} + e^{-ix}\right)$, can we use the bosonic commutation relations $\left[\hat{a}_n, \hat{a}_m^\dagger\right] = \delta_{nm}$ to obtain

$$e^{i\varphi_{a_1}^{ZPF}\left(\hat{a}_1 e^{-i\omega_{a_1}t} + \hat{a}_1^\dagger e^{i\omega_{a_1}t}\right)} = e^{-\frac{\left(\varphi_{a_1}^{ZPF}\right)^2}{2}} \sum_{n,m} \frac{\left(i\varphi_{a_1}^{ZPF}\right)^{n+m}}{n!m!} e^{i(n-m)\omega_{a_1}t} \hat{a}_1^{\dagger^n} \hat{a}_1^m \tag{A.6}$$

which we can use to treat each mode on their own. For instance working through mode a_1, we get

$$\sin\left(\varphi_{a_1}^{ZPF}\left(\hat{a}_1 e^{-i\omega_{a_1}t} + \hat{a}_1^\dagger e^{i\omega_{a_1}t}\right)\right) = e^{-\frac{\left(\varphi_{a_1}^{ZPF}\right)^2}{2}} \sum_{n,m} \mathcal{S}_{n,m}^{a_1} e^{i(n-m)\omega_{a_1}t} \hat{a}_1^{\dagger^n} \hat{a}_1^m \tag{A.7}$$

where

$$\mathcal{S}_{n,m}^{a_1} = \frac{i^{n+m-1}}{2} \frac{\left(\varphi_{a_1}^{ZPF}\right)^{n+m} - \left(-\varphi_{a_1}^{ZPF}\right)^{n+m}}{n!m!}. \tag{A.8}$$

Note that by applying the drive $\omega_d = 2\omega_{a_1} - \omega_b + 2\omega_{a_2}$ and only evaluating the terms expanded in Equation A.3, we get that the only terms surviving the time averaging operation are the terms where $n - m = \pm 2$ or $n - m = \pm 6$. However, since both of these requirements would result in $n + m$ being even, we then get that $\mathcal{S}_{n,m}^{a_1} = 0$. Expanding the cosine function, we obtain

$$\cos\left(\varphi_{a_1}^{ZPF}\left(\hat{a}_1 e^{-i\omega_{a_1}t} + \hat{a}_1^\dagger e^{i\omega_{a_1}t}\right)\right) = e^{-\frac{\left(\varphi_{a_1}^{ZPF}\right)^2}{2}} \sum_{n,m} \mathcal{C}_{n,m}^{a_1} e^{i(n-m)\omega_{a_1}t} \hat{a}_1^{\dagger^n} \hat{a}_1^m \tag{A.9}$$

with

$$\mathcal{C}_{n,m}^{a_1} = \frac{i^{n+m}}{2} \frac{\left(\varphi_{a_1}^{ZPF}\right)^{n+m} + \left(-\varphi_{a_1}^{ZPF}\right)^{n+m}}{n!m!}. \tag{A.10}$$

Which have non-zero terms under the constraint $n - m = \pm 2$ or $n - m = \pm 6$. These terms are

$$\begin{aligned}\cos\left(\varphi_{a_1}^{ZPF}\left(\hat{a}_1 e^{-i\omega_{a_1}t} + \hat{a}_1^\dagger e^{i\omega_{a_1}t}\right)\right)\Big|_{n-m=\pm 2} =& e^{-\frac{\left(\varphi_{a_1}^{ZPF}\right)^2}{2}} \sum_{n=0}^{\infty} \mathcal{C}_{n,n+2}^{a_1} \hat{a}_1^{\dagger^{n+2}} \hat{a}_1^n\\ &+ \text{h.c.}\end{aligned} \tag{A.11}$$

and

$$\cos\left(\varphi_{a_1}^{ZPF}\left(\hat{a}_1 e^{-i\omega_{a_1}t}+\hat{a}_1^\dagger e^{i\omega_{a_1}t}\right)\right)\Big|_{n-m=\pm 6} = e^{-\frac{\left(\varphi_{a_1}^{ZPF}\right)^2}{2}}\sum_{n=0}^{\infty}\mathcal{C}_{n,n+6}^{a_1}\hat{a}_1^{\dagger^{n+6}}\hat{a}_1^{n} + \text{h.c.} \tag{A.12}$$

Similar factors are also obtained for a_2.

By performing the same analysis for the buffer mode, we get that the only terms that survive are when $n-m=\pm 1$ and $n-m=\pm 3$. This time, however, we get that $\mathcal{C}_{n,m}^b = 0$ and the only surviving terms are those from $\sin\left(\varphi_b^{ZPF}\left(\hat{b}e^{-i\omega_b t}+\hat{b}^\dagger e^{i\omega_b t}\right)\right)$. The surviving terms after the RWA is then

$$\sin\left(\varphi_b^{ZPF}\left(\hat{b}e^{-i\omega_b t}+\hat{b}^\dagger e^{i\omega_b t}\right)\right)\Big|_{n-m=\pm 1} = e^{-\frac{\left(\varphi_b^{ZPF}\right)^2}{2}}\sum_{n=0}^{\infty}\mathcal{S}_{n,n+1}^{b}\hat{b}^{\dagger^{n+1}}\hat{b}^{n} + \text{h.c.} \tag{A.13}$$

and

$$\sin\left(\varphi_b^{ZPF}\left(\hat{b}e^{-i\omega_b t}+\hat{b}^\dagger e^{i\omega_b t}\right)\right)\Big|_{n-m=\pm 3} = e^{-\frac{\left(\varphi_b^{ZPF}\right)^2}{2}}\sum_{n=0}^{\infty}\mathcal{S}_{n,n+3}^{b}\hat{b}^{\dagger^{n+3}}\hat{b}^{n} + \text{h.c.} \tag{A.14}$$

If we let the order, o, of the expansion be defined as $o = x + y$ where $\hat{p}^{\dagger^x}\hat{p}^y$ are the creation and annihilation operators for the mode being expanded, and truncate after the fifth order, yields the rotating wave approximation, $\hat{\mathcal{H}}_{\text{RWA}}$, as

$$\begin{aligned}\hat{\mathcal{H}}_{\text{RWA}} = {} & G\hat{a}_1^{\dagger^2}\hat{b}\hat{a}_2^{\dagger^2} - g_{a_1}\hat{a}_1^{\dagger^3}\hat{a}_1\hat{b}\hat{a}_2^{\dagger^2} - g_b\hat{a}_1^{\dagger^2}\hat{b}^\dagger\hat{b}^2\hat{a}_2^{\dagger^2} - g_{a_2}\hat{a}_1^{\dagger^2}\hat{b}\hat{a}_2^{\dagger^3}\hat{a}_2 \\ & + \chi_{a_1a_2}\hat{a}_1^{\dagger^3}\hat{a}_1\hat{b}\hat{a}_2^{\dagger^3}\hat{a}_2 + \chi_{a_1b}\hat{a}_1^{\dagger^3}\hat{a}_1\hat{b}^\dagger\hat{b}^2\hat{a}_2^{\dagger^2} + \chi_{ba_2}\hat{a}_1^{\dagger^2}\hat{b}^\dagger\hat{b}^2\hat{a}_2^{\dagger^3}\hat{a}_2 \\ & + \chi_{bb}\hat{a}_1^{\dagger^2}\hat{b}^{\dagger^2}\hat{b}^3\hat{a}_2^{\dagger^2} - \chi_{a_1bb}\hat{a}_1^{\dagger^3}\hat{a}_1\hat{b}^{\dagger^2}\hat{b}^3\hat{a}_2^{\dagger^2} - \chi_{bba_2}\hat{a}_1^{\dagger^2}\hat{b}^{\dagger^2}\hat{b}^3\hat{a}_2^{\dagger^3}\hat{a}_2 \\ & - \chi_{a_1ba_2}\hat{a}_1^{\dagger^3}\hat{a}_1\hat{b}^\dagger\hat{b}^2\hat{a}_2^{\dagger^3}\hat{a}_2 + \chi_{a_1bba_2}\hat{a}_1^{\dagger^3}\hat{a}_1\hat{b}^{\dagger^2}\hat{b}^3\hat{a}_2^{\dagger^3}\hat{a}_2 + \text{h.c.}\end{aligned} \tag{A.15}$$

where the coefficients in front of each of the operators takes the form

$$\begin{cases}\gamma & = \frac{8\xi-\xi^3}{8}E_\Sigma e^{-\frac{\left|\left|\varphi^{ZPF}\right|\right|^2}{2}}\frac{\left(\varphi_{a_1}^{ZPF}\right)^2\varphi_b^{ZPF}\left(\varphi_{a_2}^{ZPF}\right)^2}{864} \\ G & = 108\gamma \\ g_{a_1} & = 36\left(\varphi_{a_1}^{ZPF}\right)^2\gamma \\ g_b & = 54\left(\varphi_b^{ZPF}\right)^2\gamma \\ g_{a_2} & = 36\left(\varphi_{a_2}^{ZPF}\right)^2\gamma \\ \chi_{a_1a_2} & = 12\left(\varphi_{a_1}^{ZPF}\right)^2\left(\varphi_{a_2}^{ZPF}\right)^2\gamma \\ \chi_{a_1b} & = 18\left(\varphi_{a_1}^{ZPF}\right)^2\left(\varphi_b^{ZPF}\right)^2\gamma \\ \chi_{ba_2} & = 18\left(\varphi_b^{ZPF}\right)^2\left(\varphi_{a_2}^{ZPF}\right)^2\gamma \\ \chi_{bb} & = 9\left(\varphi_b^{ZPF}\right)^4\gamma \\ \chi_{a_1bb} & = 3\left(\varphi_{a_1}^{ZPF}\right)^2\left(\varphi_b^{ZPF}\right)^4\gamma \\ \chi_{bba_2} & = 3\left(\varphi_b^{ZPF}\right)^4\left(\varphi_{a_2}^{ZPF}\right)^2\gamma \\ \chi_{a_1ba_2} & = 6\left(\varphi_{a_1}^{ZPF}\right)^2\left(\varphi_b^{ZPF}\right)^2\left(\varphi_{a_2}^{ZPF}\right)^2\gamma \\ \chi_{a_1bba_2} & = \left(\varphi_{a_1}^{ZPF}\right)^2\left(\varphi_b^{ZPF}\right)^4\left(\varphi_{a_2}^{ZPF}\right)^2\gamma\end{cases} \tag{A.16}$$

with $\left|\left|\varphi^{ZPF}\right|\right|^2 = \left(\varphi^{ZPF}_{a_1}\right)^2 + \left(\varphi^{ZPF}_{b}\right)^2 + \left(\varphi^{ZPF}_{a_2}\right)^2$.

Keeping only the leading term and applying a resonant drive on the buffer mode yields the Hamiltonian $\hat{\mathcal{H}}_{\text{RWA}} = G\hat{a}_1^{\dagger^2}\hat{b}\hat{a}_2^{\dagger^2} + \zeta\hat{b} + \text{h.c.}$.

A.2 Adiabatically Removing the Buffer mode

Our Hamiltonian in the rotating frame is

$$\hat{\mathcal{H}}_{RWA} = G\left(\hat{a}_1^{\dagger^2}\hat{a}_2^{\dagger^2}\hat{b} + \hat{b}^\dagger\hat{a}_2^2\hat{a}_1^2\right) + \zeta^*\hat{b}^\dagger + \zeta\hat{b} \tag{A.17}$$

but this Hamiltonian consists of a buffer mode which is not present in the modes for the pair-coherent state. Ergo, we should try to eliminate the buffer mode.

A general density matrix time-evolves as

$$\dot{\hat{\rho}} = -i\left[\hat{\mathcal{H}}, \hat{\rho}\right] + \sum_k \mathcal{D}[\hat{L}_k]\hat{\rho} \tag{A.18}$$

where $\mathcal{D}$ is the dissipator and $\hat{L}_k$ is a collapse operator [49]. Assuming a large dissipation rate of the buffer mode, κ_b, can we approximate the population in the buffer mode as a two-level system as the population in the buffer mode is highly unlikely to be larger than 1. We can then define $|g\rangle_b = |0\rangle_b$ and $|e\rangle_b = |1\rangle_b$ where $|g\rangle_b$ and $|e\rangle_b$ are the ground and excited state for the buffer mode respectively. Following the method by Reiter and Sørensen [50] can we describe the time-evolution of the state-generating modes with an effective Hamiltonian and effective collapse operator. The effective Hamiltonian is

$$\hat{\mathcal{H}}_{\text{eff}} = -\frac{1}{2}\hat{V}_-\left(\hat{\mathcal{H}}_{NH}^{-1} + \left(\hat{\mathcal{H}}_{NH}^{-1}\right)^\dagger\right)\hat{V}_+ + \hat{\mathcal{H}}_g \tag{A.19}$$

where

$$\hat{\mathcal{H}}_{NH} = \hat{\mathcal{H}}_e - \frac{i}{2}\sum_k \hat{L}_k^\dagger\hat{L}_k \tag{A.20}$$

and the effective collapse operator is

$$\hat{L}^k_{\text{eff}} = \hat{L}_k\hat{\mathcal{H}}_{NH}^{-1}\hat{V}_+. \tag{A.21}$$

Limiting ourselves to the two level system of the buffer mode, can we determine the $\hat{\mathcal{H}}_{e/g}$ and $\hat{V}_{+/-}$ operators to be

$$\begin{cases} \hat{\mathcal{H}}_e = |1\rangle_b\langle 1|\hat{\mathcal{H}}^{RWA}|1\rangle_b\langle 1| = 0 \\ \hat{\mathcal{H}}_g = |0\rangle_b\langle 0|\hat{\mathcal{H}}^{RWA}|0\rangle_b\langle 0| = 0 \\ \hat{V}_+ = |1\rangle_b\langle 1|\hat{\mathcal{H}}^{RWA}|1\rangle_b\langle 0| = \left(G\hat{a}_1^2\hat{a}_2^2 + \zeta^*\right)|0\rangle_b\langle 0| \\ \hat{V}_- = |0\rangle_b\langle 0|\hat{\mathcal{H}}^{RWA}|1\rangle_b\langle 1| = \left(G\hat{a}_1^{\dagger^2}\hat{a}_2^{\dagger^2} + \zeta\right)|0\rangle_b\langle 1|. \end{cases} \tag{A.22}$$

The original collapse operator is $\hat{L} = \sqrt{\kappa_b}\hat{b} \simeq \sqrt{\kappa_b}|0\rangle_b\langle 1|$, where κ_b is the dissipation rate of the lossy buffer mode, and we get the non-Hermitian Hamiltonian $\hat{\mathcal{H}}_{NH}$ to be

$$\hat{\mathcal{H}}_{NH} = -\frac{i\kappa_b}{2}\hat{b}^\dagger\hat{b} \simeq -\frac{i\kappa_b}{2}|1\rangle_b\langle 1| \tag{A.23}$$

and since it is a singular matrix is the inverse straight-forward to calculate as

$$\hat{\mathcal{H}}_{NH}^{(-1)} = \frac{2i}{\kappa_b}|1\rangle_b\langle 1|. \tag{A.24}$$

Using Equations A.19 and A.21 is it also straight-forward to see

$$\begin{cases} \hat{\mathcal{H}}_{\text{eff}} = 0 \\ \hat{L}_{\text{eff}} = \sqrt{\frac{4}{\kappa_b}} i \left(G\hat{a}_1^2\hat{a}_2^2 + \zeta^*\right) \end{cases} \tag{A.25}$$

and we obtain

$$\dot{\hat{\rho}} = \frac{4G^2}{\kappa_b}\mathcal{D}\left[\hat{a}_1^2\hat{a}_2^2 + \frac{\zeta^*}{G}\right]\hat{\rho} \tag{A.26}$$

with the dissipator $\mathcal{D}\left[\hat{A}\right]\hat{\rho} = \hat{A}\hat{\rho}\hat{A}^\dagger - \frac{1}{2}\left\{\hat{A}^\dagger\hat{A}, \hat{\rho}\right\}$. By then expanding the dissipator, can we through some clever algebra obtain

$$\dot{\hat{\rho}} = -i\left[\frac{2Gi}{\kappa_b}\left(\zeta^*\hat{a}_1^2\hat{a}_2^2 - \zeta\hat{a}_1^{\dagger^2}\hat{a}_2^{\dagger^2}\right), \hat{\rho}\right] + \frac{4G^2}{\kappa_b}\mathcal{D}\left[\hat{a}_1^2\hat{a}_2^2\right]\hat{\rho} \tag{A.27}$$

with the effective/reduced Hamiltonian

$$\hat{\mathcal{H}}_0 = -\frac{2G}{\kappa_b} i \left(\zeta^*\hat{a}_1^{\dagger^2}\hat{a}_2^{\dagger^2} - \zeta\hat{a}_1^2\hat{a}_2^2\right). \tag{A.28}$$

B

Construction of Gates

The X-gate can be constructed by applying a charge-line drive to the buffer mode.

The Hamiltonian then becomes

$$\begin{aligned}\hat{\mathcal{H}} &= \hbar\omega_{a_1}\hat{a}_1^\dagger\hat{a}_1 + \hbar\omega_b\hat{b}^\dagger\hat{b} + \hbar\omega_{a_2}\hat{a}_2^\dagger\hat{a}_2 + E_\Sigma\epsilon(t)\sin(\hat{\varphi}) + \hbar\zeta^* e^{i\omega_b t}\hat{b} + \hbar\zeta e^{-i\omega_b t}\hat{b}^\dagger \\ &\quad + \hbar\left(\varepsilon_X(t)^*\hat{b} + \varepsilon_X(t)\hat{b}^\dagger\right)\end{aligned} \tag{B.1}$$

with $\varepsilon_X(t)$ being the strength of the charge line [42]. Note that by applying the charge drive on the buffer mode yields an an effective displacement of the buffer mode which we can calculate by rotating the Hamiltonian into the displacement picture using the displacement operator $\hat{D}(\beta) = e^{\beta^*(t)\hat{b}-\beta(t)\hat{b}^\dagger}$ where $\beta(t)$ is the displacement of the buffer mode [51,52]. The transformed Hamiltonian can then be calculated as

$$\hat{\mathcal{H}}' = \hat{D}^\dagger\hat{\mathcal{H}}\hat{D} - i\hbar\hat{D}^\dagger\frac{\mathrm{d}\hat{D}}{\mathrm{d}t} \tag{B.2}$$

which by using the following relations

$$\begin{cases}\hat{D}^\dagger\frac{\mathrm{d}\hat{D}}{\mathrm{d}t} & = \dot{\beta}^*\hat{b} - \dot{\beta}\hat{b}^\dagger + \frac{1}{2}\left(\dot{\beta}\beta^* - \dot{\beta}^*\beta\right) \\ \hat{D}^\dagger\hat{b}\hat{D} & = \hat{b} - \beta \\ \hat{D}^\dagger\sin(\hat{\varphi})\hat{D} & = \sin\left(\hat{\varphi} - \varphi_b^{ZPF}\left(\beta + \beta^*\right)\right)\end{cases} \tag{B.3}$$

where the dot $(\dot{})$ denotes the time derivative. We then get

$$\begin{aligned}\hat{\mathcal{H}}' &= \hbar\omega_{a_1}\hat{a}_1^\dagger\hat{a}_1 + \hbar\omega_b\left(\hat{b}^\dagger\hat{b} - \beta^*\hat{b} - \beta\hat{b}^\dagger + |\beta|^2\right) + \hbar\omega_{a_2}\hat{a}_2^\dagger\hat{a}_2 \\ &\quad + E_\Sigma\epsilon(t)\sin\left(\hat{\varphi} - \varphi_b^{ZPF}\left(\beta+\beta^*\right)\right) + \hbar\varepsilon_X(t)\left(\hat{b}^\dagger - \beta^*\right) \\ &\quad + \hbar\varepsilon_X^*(t)\left(\hat{b} - \beta\right) - i\hbar\left(\dot{\beta}^*\hat{b} - \dot{\beta}\hat{b}^\dagger\right) - \frac{i\hbar}{2}\left(\dot{\beta}\beta^* - \dot{\beta}^*\beta\right) \\ &\quad + \hbar\zeta^* e^{i\omega_b t}\left(\hat{b} - \beta\right) + \hbar\zeta e^{-i\omega_b t}\left(\hat{b}^\dagger - \beta^*\right)\end{aligned} \tag{B.4}$$

which reduces to a slightly modified version of our Hamiltonian when $\dot{\beta}(t) = -i\omega_b\beta + i\varepsilon_X(t)$. Let $\varepsilon_X(t) = \zeta_X e^{-i\omega_X t}$ then

$$\beta(t) = \frac{\zeta_X}{\omega_b - \omega_X}e^{-i\omega_X t} \tag{B.5}$$

from which it is easy to see

$$\beta(t) + \beta^*(t) = \frac{2\zeta_X}{\omega_b - \omega_X}\cos(\omega_X t). \tag{B.6}$$

Here we have assumed that ζ_X is purely real. Dropping the additional terms, we get the following Hamiltonian

$$\begin{aligned}
\hat{\mathcal{H}}' &= \hbar\omega_{a_1}\hat{a}_1^\dagger\hat{a}_1 + \hbar\omega_b\hat{b}^\dagger\hat{b} + \hbar\omega_{a_2}\hat{a}_2^\dagger\hat{a}_2 + E_\Sigma\epsilon(t)\sin\left(\hat{\varphi} - \varphi_b^{ZPF}\left(\beta(t) + \beta^*(t)\right)\right) \\
&\quad + \hbar\zeta^* e^{i\omega_b t}\hat{b} + \hbar\zeta e^{-i\omega_b t}\hat{b}^\dagger \\
&= \hbar\omega_{a_1}\hat{a}_1^\dagger\hat{a}_1 + \hbar\omega_b\hat{b}^\dagger\hat{b} + \hbar\omega_{a_2}\hat{a}_2^\dagger\hat{a}_2 \\
&\quad + E_\Sigma\epsilon(t)\sin\left(\hat{\varphi}\right)\cos\left(\frac{2\zeta_X\varphi_b^{ZPF}}{\omega_b - \omega_X}\cos(\omega_X t)\right) \\
&\quad - E_\Sigma\epsilon(t)\sin\left(\frac{2\zeta_X\varphi_b^{ZPF}}{\omega_b - \omega_X}\cos(\omega_X t)\right)\cos\left(\hat{\varphi}\right) + \hbar\zeta^* e^{i\omega_b t}\hat{b} + \hbar\zeta e^{-i\omega_b t}\hat{b}^\dagger
\end{aligned} \tag{B.7}$$

which by performing a first order Taylor expansion we get to equal to

$$\begin{aligned}
\hat{\mathcal{H}}' = {} & \hbar\omega_{a_1}\hat{a}_1^\dagger\hat{a}_1 + \hbar\omega_b\hat{b}^\dagger\hat{b} + \hbar\omega_{a_2}\hat{a}_2^\dagger\hat{a}_2 + E_\Sigma\epsilon(t)\sin(\hat{\varphi}) \\
& - \frac{2E_\Sigma\zeta_X\varphi_b^{ZPF}}{\omega_b - \omega_X}\cos(\omega_X t)\epsilon(t)\cos(\hat{\varphi}) + \hbar\zeta^* e^{i\omega_b t}\hat{b} + \hbar\zeta e^{-i\omega_b t}\hat{b}^\dagger
\end{aligned} \tag{B.8}$$

Recall that $\epsilon(t) = \frac{\xi}{2}\left(e^{i\left(2\omega_{a_1} - \omega_b + 2\omega_{a_2}\right)t} + e^{-i\left(2\omega_{a_1} - \omega_b + 2\omega_{a_2}\right)t}\right)$ and that we require the leading order of the X-gate to be $\hat{a}_1^\dagger\hat{a}_2^\dagger + \text{h.c.}$. Then a natural choice of the drive function for the coherent drive of the X-gate is $\varepsilon_X(t) = \zeta_X\cos\left(\left(\omega_{a_1} - \omega_b + \omega_{a_2}\right)t\right)$, and we obtain

$$\epsilon(t)\varepsilon_X(t) = \frac{\xi\zeta_X}{4}\left(e^{i\left(3\omega_{a_1} - 2\omega_b + 3\omega_{a_2}\right)t} + e^{i\left(\omega_{a_1} + \omega_{a_2}\right)t} + \text{h.c.}\right). \tag{B.9}$$

By performing the RWA up to the first correction from the unwanted frequency $\omega_d + \omega_X$ where $\omega_X = \omega_{a_1} - \omega_b + \omega_{a_2}$ we get

$$\begin{aligned}
\hat{\mathcal{H}}_X = {} & g_x\hat{a}_1^\dagger\hat{a}_2^\dagger - g_{X,a_1}\hat{a}_1^{\dagger^2}\hat{a}_1\hat{a}_2^\dagger - g_{X,b}\hat{a}_1^\dagger\hat{b}^\dagger\hat{b}\hat{a}_2^\dagger - g_{X,a_2}\hat{a}_1^\dagger\hat{a}_2^{\dagger^2}\hat{a}_2 \\
& + \chi_{X,bb}\hat{a}_1^\dagger\hat{b}^{\dagger^2}\hat{b}^2\hat{a}_2^\dagger + \chi_{X,a_1a_2}\hat{a}_1^{\dagger^2}\hat{a}_1\hat{a}_2^{\dagger^2}\hat{a}_2 + \chi_{X,a_1b}\hat{a}_1^{\dagger^2}\hat{a}_1\hat{b}^\dagger\hat{b}\hat{a}_2^\dagger \\
& + \chi_{X,ba_2}\hat{a}_1^\dagger\hat{b}^\dagger\hat{b}\hat{a}_2^{\dagger^2}\hat{a}_2 + \chi_{X,a_1a_1}\hat{a}_1^{\dagger^3}\hat{a}_1^2\hat{a}_2^\dagger + \chi_{X,a_2a_2}\hat{a}_1^\dagger\hat{a}_2^{\dagger^3}\hat{a}_2^2 \\
& - \chi_{X,bbb}\hat{a}_1^\dagger\hat{b}^{\dagger^3}\hat{b}^3\hat{a}_2^\dagger - \chi_{X,a_1bb}\hat{a}_1^{\dagger^2}\hat{a}_1\hat{b}^{\dagger^2}\hat{b}^2\hat{a}_2^\dagger - \chi_{X,bba_2}\hat{a}_1^\dagger\hat{b}^{\dagger^2}\hat{b}^2\hat{a}_2^{\dagger^2}\hat{a}_2 \\
& - \chi_{X,a_1ba_2}\hat{a}_1^{\dagger^2}\hat{a}_1\hat{b}^\dagger\hat{b}\hat{a}_2^{\dagger^2}\hat{a}_2 - \chi_{X,a_1a_1b}\hat{a}_1^{\dagger^3}\hat{a}_1^2\hat{b}^\dagger\hat{b}\hat{a}_2^\dagger - \chi_{X,ba_2a_2}\hat{a}_1^\dagger\hat{b}^\dagger\hat{b}\hat{a}_2^{\dagger^3}\hat{a}_2^2 \\
& - \chi_{X,a_1a_1a_2}\hat{a}_1^{\dagger^3}\hat{a}_1^2\hat{a}_2^{\dagger^2}\hat{a}_2 - \chi_{X,a_1a_2a_2}\hat{a}_1^{\dagger^2}\hat{a}_1\hat{a}_2^{\dagger^3}\hat{a}_2^2 - \chi_{X,a_1a_1a_1}\hat{a}_1^{\dagger^4}\hat{a}_1^3\hat{a}_2^\dagger \\
& - \chi_{X,a_2a_2a_2}\hat{a}_1^\dagger\hat{a}_2^{\dagger^4}\hat{a}_2^3 - G_{3X}\hat{a}_1^{\dagger^3}\hat{b}^2\hat{a}_2^{\dagger^3} + \text{h.c.}
\end{aligned} \tag{B.10}$$

with

$$\begin{cases} g_x = \frac{\varphi_{a_1}^{ZPF}\varphi_b^{ZPF}\varphi_{a_2}^{ZPF}}{2\left(\omega_{a_1}+\omega_{a_2}-2\omega_b\right)} E_\Sigma \xi \zeta_X e^{-\frac{\left|\left|\varphi^{ZPF}\right|\right|^2}{2}} \\ g_{X,a_1} = \frac{\left(\varphi_{a_1}^{ZPF}\right)^2}{2} g_x \\ g_{X,b} = \left(\varphi_b^{ZPF}\right)^2 g_x \\ g_{X,a_2} = \frac{\left(\varphi_{a_2}^{ZPF}\right)^2}{2} g_x \\ \chi_{X,bb} = \frac{\left(\varphi_b^{ZPF}\right)^4}{4} g_x \\ \chi_{X,a_1a_2} = \frac{\left(\varphi_{a_1}^{ZPF}\right)^2\left(\varphi_{a_2}^{ZPF}\right)^2}{4} g_x \\ \chi_{X,a_1b} = \frac{\left(\varphi_{a_1}^{ZPF}\right)^2\left(\varphi_b^{ZPF}\right)^2}{2} g_x \\ \chi_{X,ba_2} = \frac{\left(\varphi_b^{ZPF}\right)^2\left(\varphi_{a_2}^{ZPF}\right)^2}{2} g_x \\ \chi_{X,a_1a_1} = \frac{\left(\varphi_{a_1}^{ZPF}\right)^4}{12} g_x \\ \chi_{X,a_2a_2} = \frac{\left(\varphi_{a_2}^{ZPF}\right)^4}{12} g_x \\ \chi_{X,bbb} = \frac{\left(\varphi_b^{ZPF}\right)^6}{36} g_x \\ \chi_{X,a_1bb} = \frac{\left(\varphi_{a_1}^{ZPF}\right)^2\left(\varphi_b^{ZPF}\right)^4}{8} g_x \\ \chi_{X,bba_2} = \frac{\left(\varphi_b^{ZPF}\right)^4\left(\varphi_{a_2}^{ZPF}\right)^2}{8} g_x \\ \chi_{X,a_1ba_2} = \frac{\left(\varphi_{a_1}^{ZPF}\right)^2\left(\varphi_b^{ZPF}\right)^2\left(\varphi_{a_2}^{ZPF}\right)^2}{4} g_x \\ \chi_{X,a_1a_1b} = \frac{\left(\varphi_{a_1}^{ZPF}\right)^4\left(\varphi_b^{ZPF}\right)^2}{12} g_x \\ \chi_{X,ba_2a_2} = \frac{\left(\varphi_b^{ZPF}\right)^2\left(\varphi_{a_2}^{ZPF}\right)^4}{12} g_x \\ \chi_{X,a_1a_1a_2} = \frac{\left(\varphi_{a_1}^{ZPF}\right)^4\left(\varphi_{a_2}^{ZPF}\right)^2}{24} g_x \\ \chi_{X,a_1a_2a_2} = \frac{\left(\varphi_{a_1}^{ZPF}\right)^2\left(\varphi_{a_2}^{ZPF}\right)^4}{24} g_x \\ \chi_{X,a_1a_1a_1} = \frac{\left(\varphi_{a_1}^{ZPF}\right)^6}{144} g_x \\ \chi_{X,a_2a_2a_2} = \frac{\left(\varphi_{a_2}^{ZPF}\right)^6}{144} g_x \\ G_{3X} = \frac{\left(\varphi_{a_1}^{ZPF}\right)^2\left(\varphi_b^{ZPF}\right)^2\left(\varphi_{a_2}^{ZPF}\right)^2}{72} g_x \end{cases} \tag{B.11}$$

Note that the zero-point fluctuations are quite large, and the ideal gate is therefore not enough to properly describe the interaction. Since the gate that stabilizes the pair-cat state is in fifth order with regards to the zero-point fluctuations; we suggest to implement the X-gate to at least seventh order with regards to the zero-point fluctuations whenever simulations are performed.

C

Results for the Induced Joint Two Photon Decay

In this Appendix, we present the figures for the induced joint two photon decay, when the state is initialized in Fock states $|2,0\rangle, |2,2\rangle, |3,1\rangle, |3,2\rangle, |3,3\rangle$, $|4,4\rangle, |5,2\rangle$, $|5,3\rangle, |5,4\rangle, |5,5\rangle, |6,6\rangle, |7,2\rangle, |7,3\rangle, |7,4\rangle, |7,5\rangle$, $|7,6\rangle, |7,7\rangle$, and $|8,8\rangle$ of the state-generating modes.

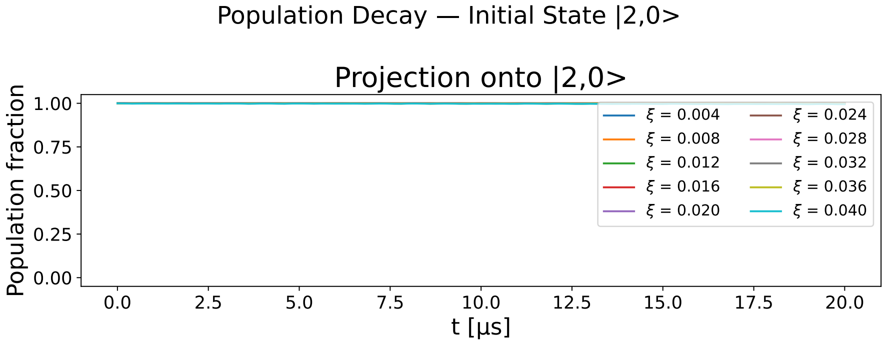

Figure C.1: Population decay of state initialized in $|2,0\rangle$. No decay occur for any pump strength.

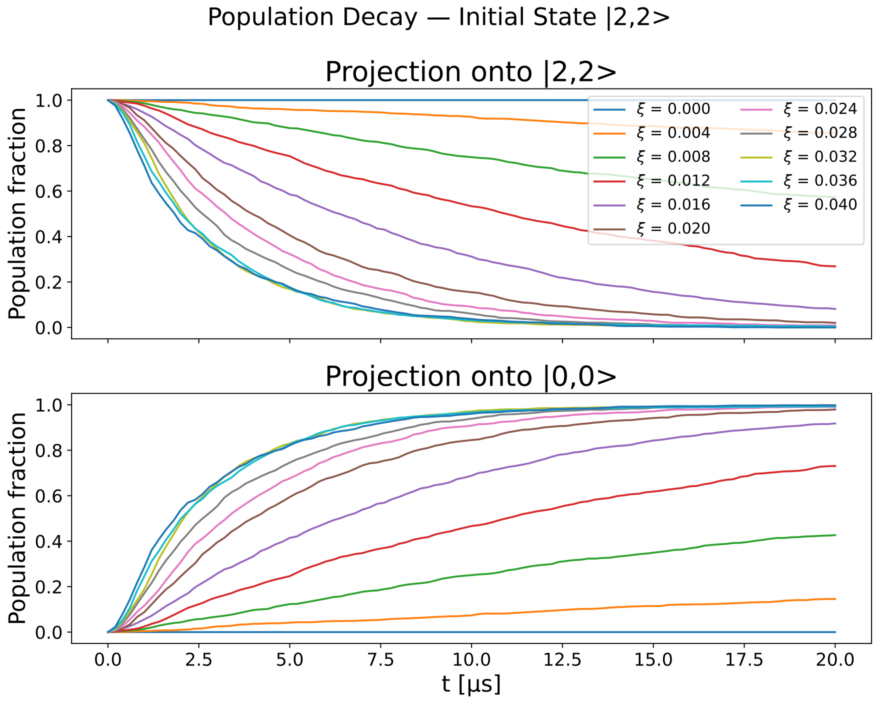

Figure C.2: Population decay of state initialized in $|2,2\rangle$. The decay is quicker for larger pump strengths, and maxes out at $\xi = 0.032$.

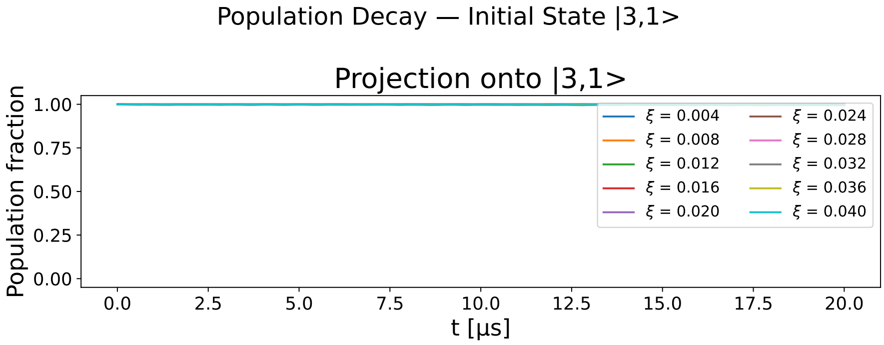

Figure C.3: Population decay of state initialized in $|3,1\rangle$. No decay occur for any pump strength.

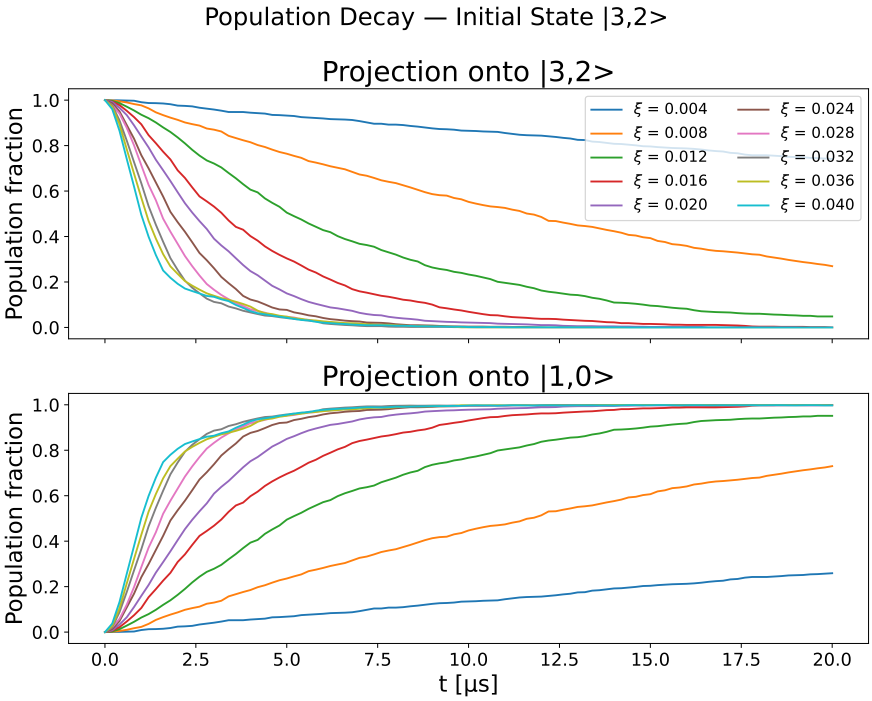

Figure C.4: Population decay of state initialized in $|3,2\rangle$. The population decays into state $|1,0\rangle$ and maxes out at $\xi = 0.032$.

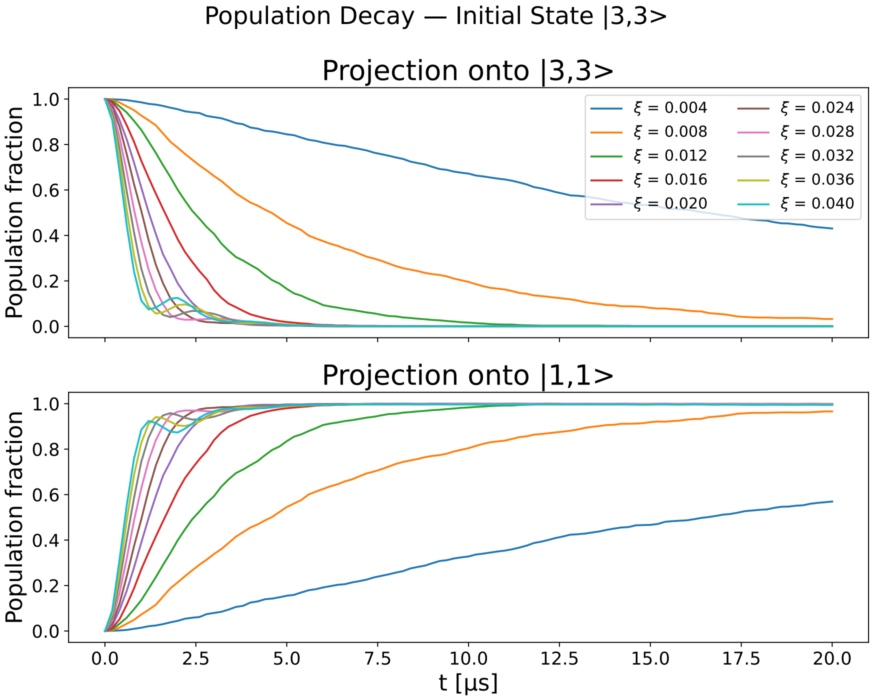

Figure C.5: Population decay of state initialized in $|3,3\rangle$. For larger pump strengths do we observe ”kicks” as the population in $|3,3\rangle$ start to repopulate.

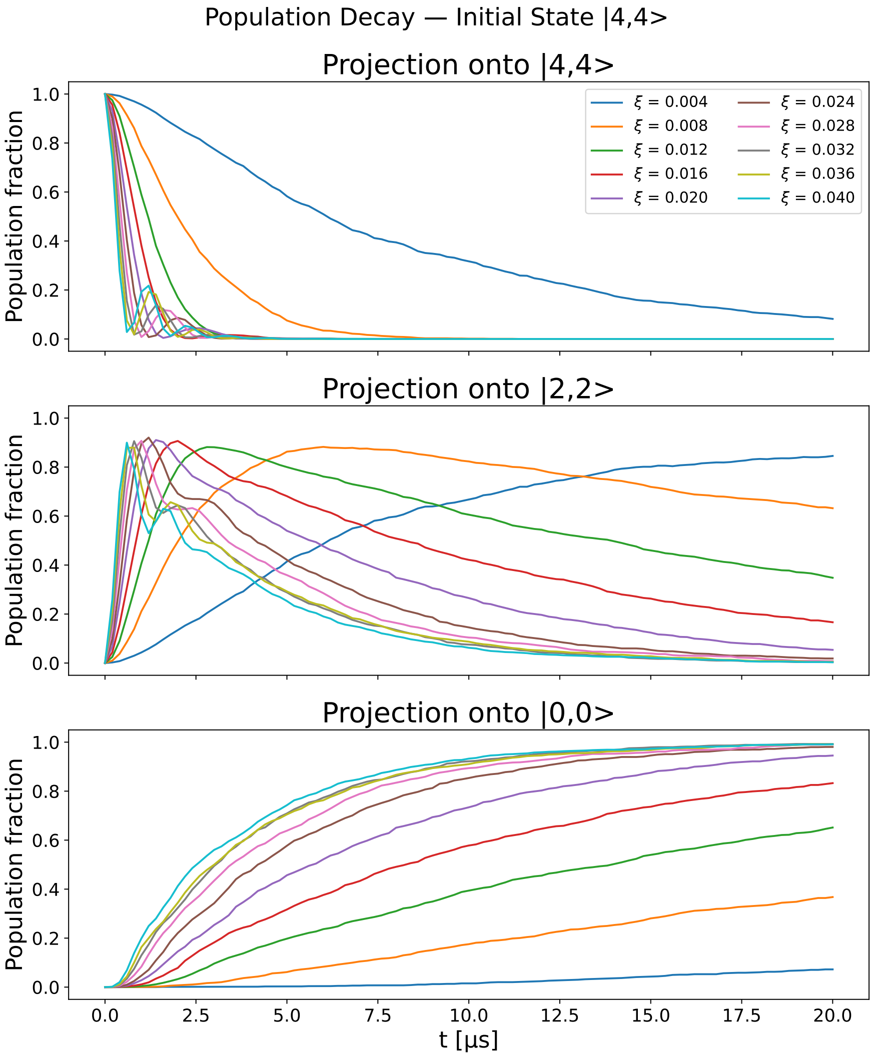

Figure C.6: Population decay of state initialized in $|4,4\rangle$. The decay occurs in two steps, from $|4,4\rangle$ to $|2,2\rangle$ and then $|0,0\rangle$. For larger pump strengths do we observe "kicks" as the population in $|2,2\rangle$ start to repopulate the population in $|4,4\rangle$. No meaningful kicks are observed from $|0,0\rangle$ to $|2,2\rangle$.

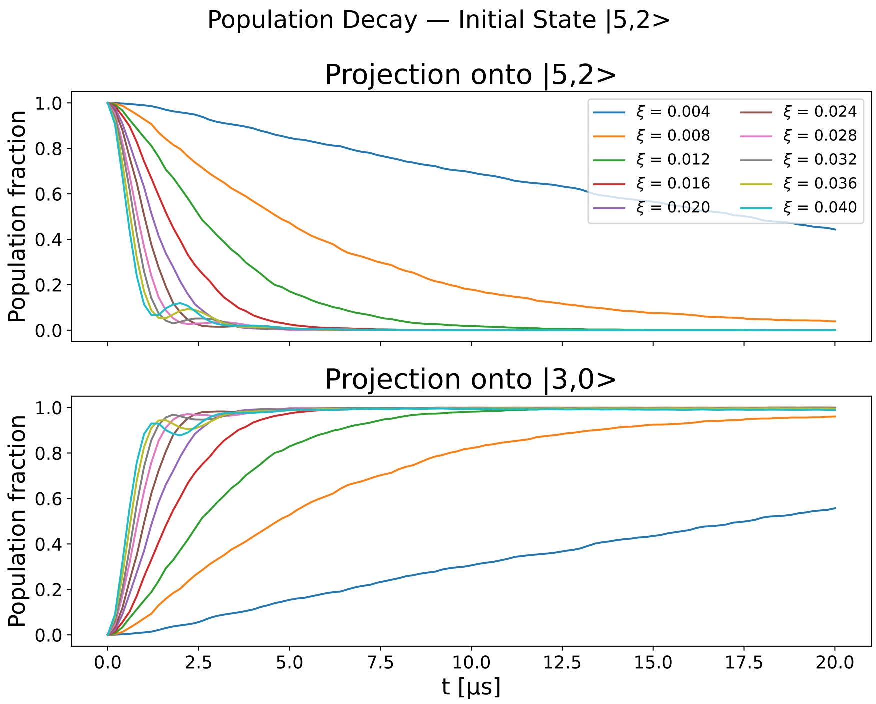

Figure C.7: Population decay of state initialized in $|5,2\rangle$. For larger pump strengths do we observe ”kicks” as the population in $|5,2\rangle$ start to repopulate.

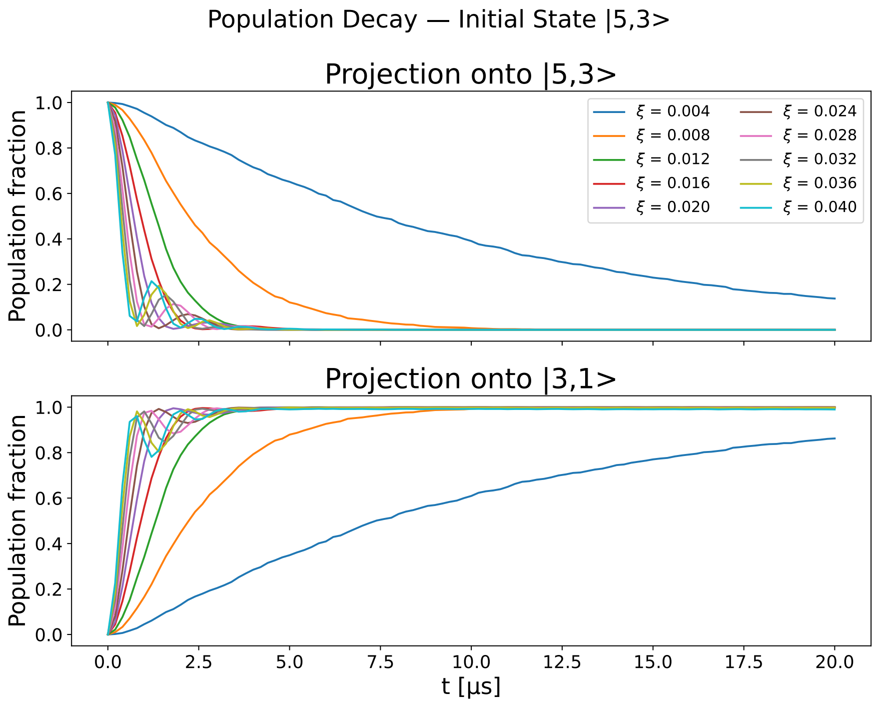

Figure C.8: Population decay of state initialized in $|5,3\rangle$. For larger pump strengths do we observe ”kicks” as the population in $|5,3\rangle$ start to repopulate. These kicks are stronger than for the repopulation of $|5,2\rangle$.

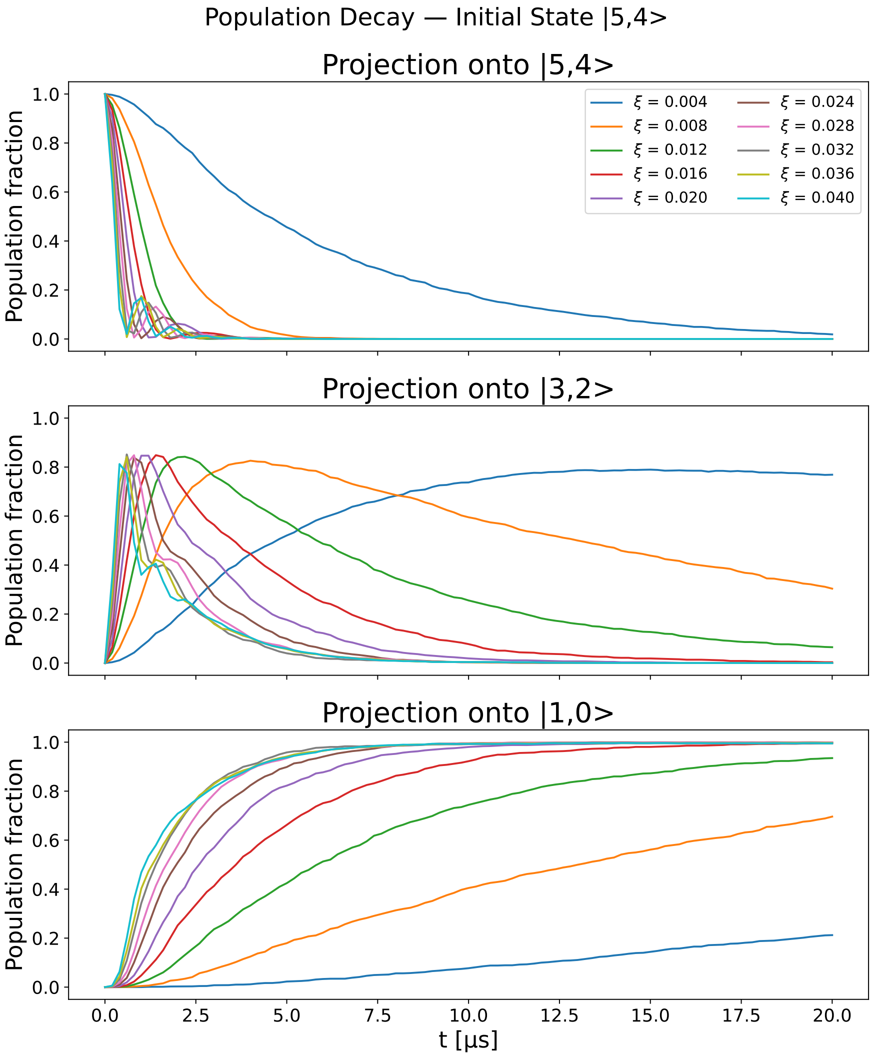

Figure C.9: Population decay of state initialized in $|5,4\rangle$. The decay occurs in two steps, from $|5,4\rangle$ to $|3,2\rangle$ and then from $|3,2\rangle$ to $|1,0\rangle$. For larger pump strengths do we observe ”kicks” as the population in $|3,2\rangle$ start to repopulate the population in $|5,4\rangle$. No meaningful kicks are observed from $|1,0\rangle$ to $|3,2\rangle$.

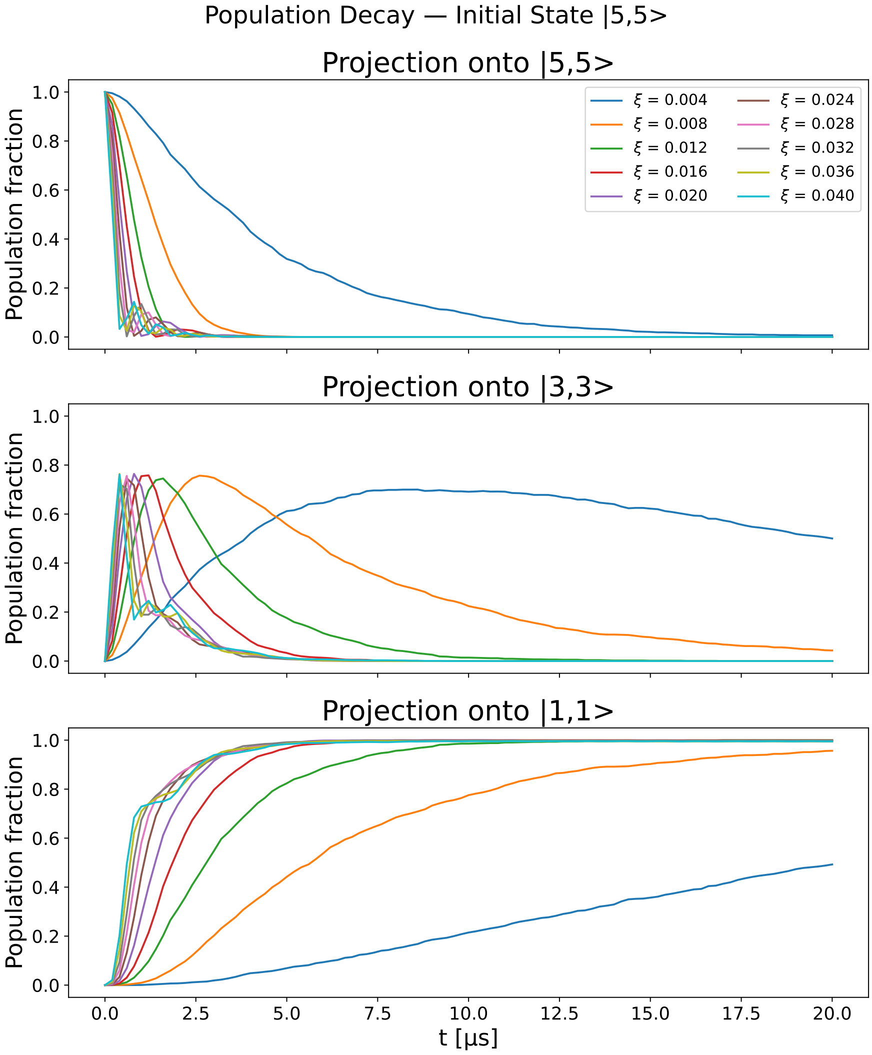

Figure C.10: Population decay of state initialized in $|5,5\rangle$. The decay occurs in two steps, first from $|5,5\rangle$ to $|3,3\rangle$ and then from $|3,3\rangle$ to $|1,1\rangle$. For larger pump strengths do we observe "kicks" as the population in $|3,3\rangle$ start to repopulate the population in $|5,5\rangle$. For the largest pump strength do we also observe repopulation of $|3,3\rangle$ from $|1,1\rangle$.

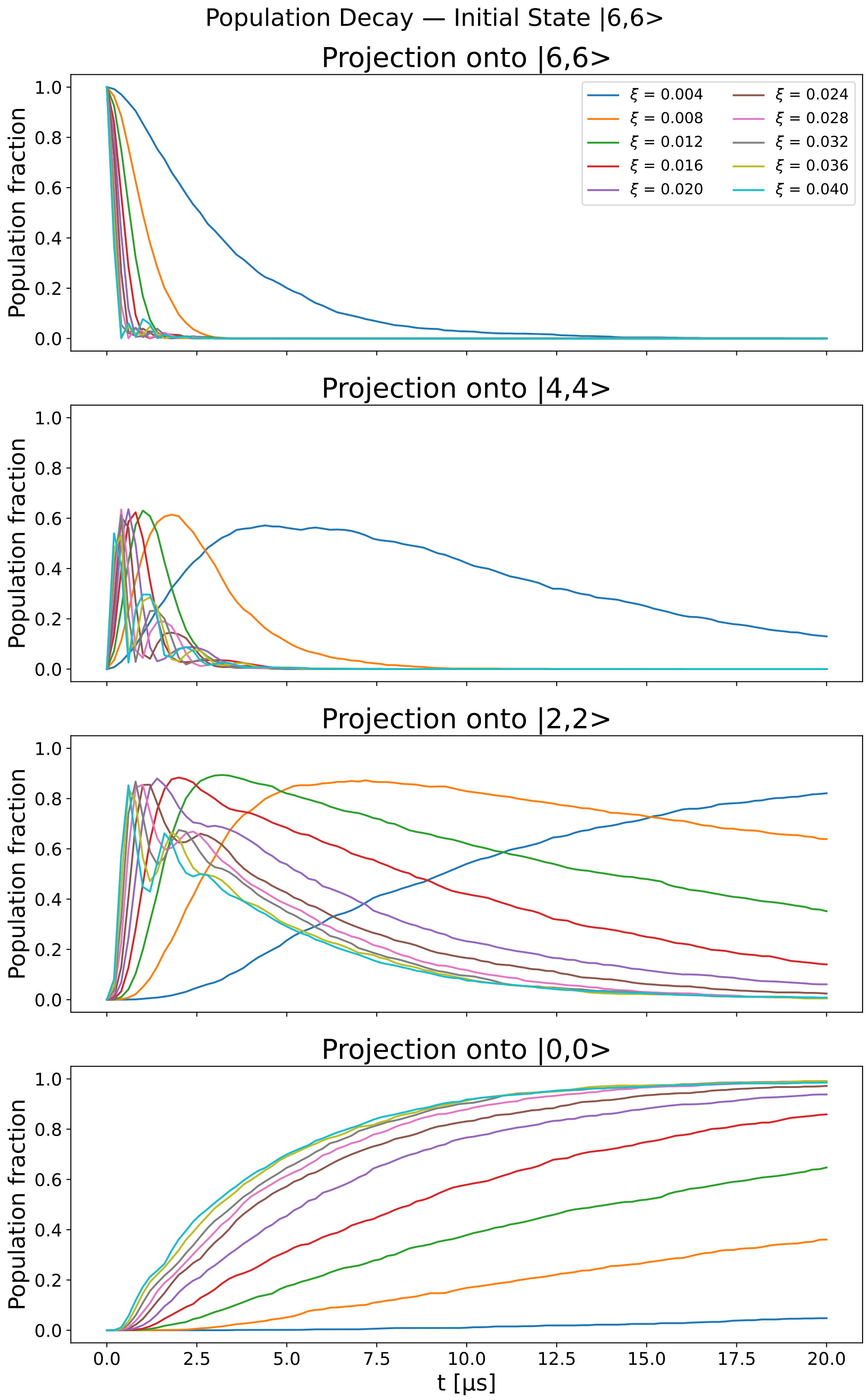

Figure C.11: Population decay of state initialized in $|6,6\rangle$. The decay occurs in three steps, first from $|6,6\rangle$ to $|4,4\rangle$, then from $|4,4\rangle$ to $|2,2\rangle$, and finally from $|2,2\rangle$ to $|0,0\rangle$. For larger pump strengths do we observe "kicks" as the non-vacuum states repopulate. The repopulation for state $|6,6\rangle$ is negligible in comparison to the kicks of $|4,4\rangle$ and $|2,2\rangle$. The repopulation of $|2,2\rangle$ is a consequence of the repopulation of $|4,4\rangle$.

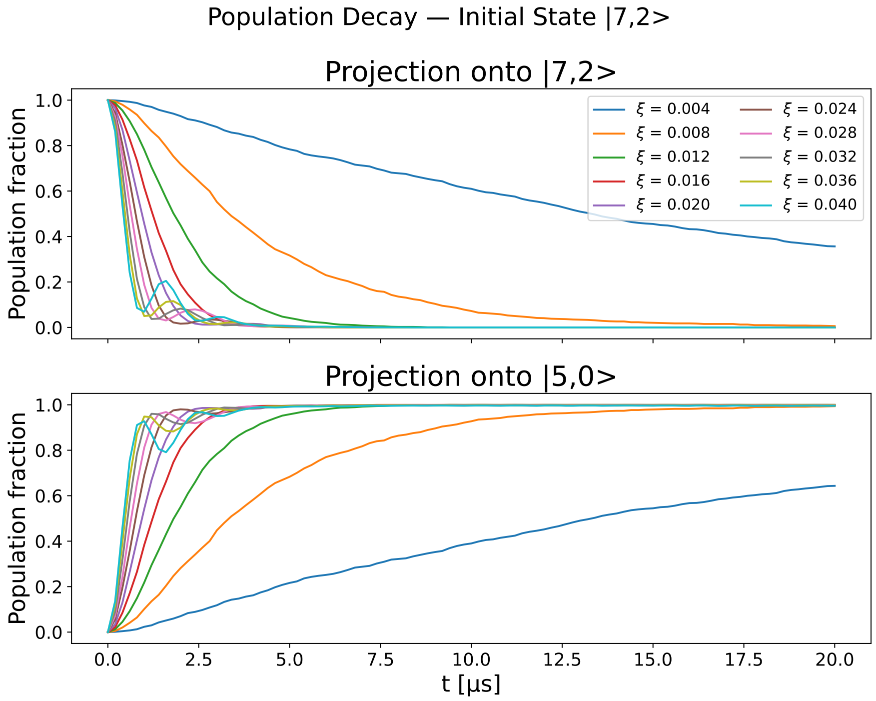

Figure C.12: Population decay of state initialized in $|7,2\rangle$. For larger pump strengths do we observe "kicks" as the population in $|7,2\rangle$ start to repopulate.

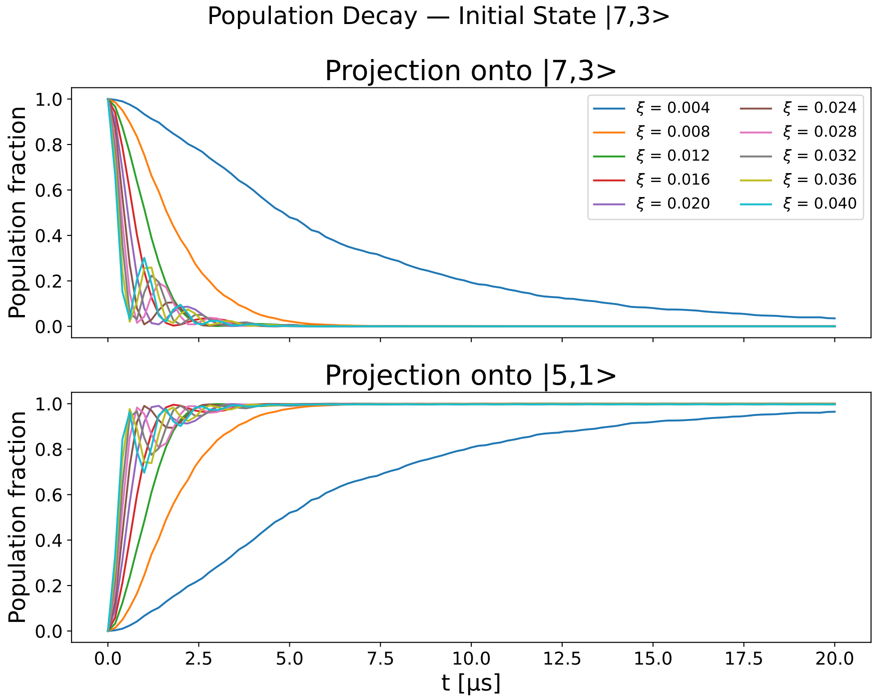

Figure C.13: Population decay of state initialized in $|7,3\rangle$. For larger pump strengths do we observe "kicks" as the population in $|7,3\rangle$ start to repopulate.

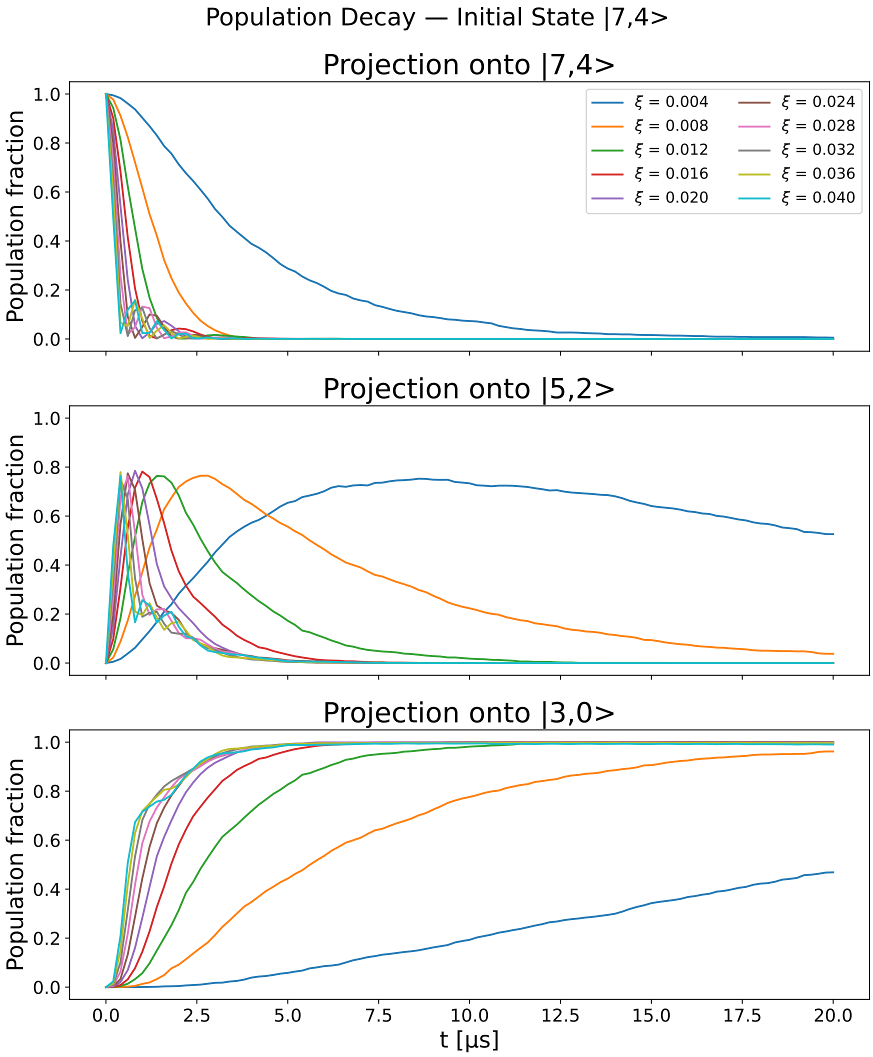

Figure C.14: Population decay of state initialized in $|7,4\rangle$. The decay occurs in two steps, first from $|7,4\rangle$ to $|5,2\rangle$ and then from $|5,2\rangle$ to $|3,0\rangle$. For larger pump strengths do we observe ”kicks” as the population in $|5,2\rangle$ start to repopulate the population in $|7,4\rangle$. For the largest pump strength do we also observe repopulation of $|5,2\rangle$ from $|3,0\rangle$.

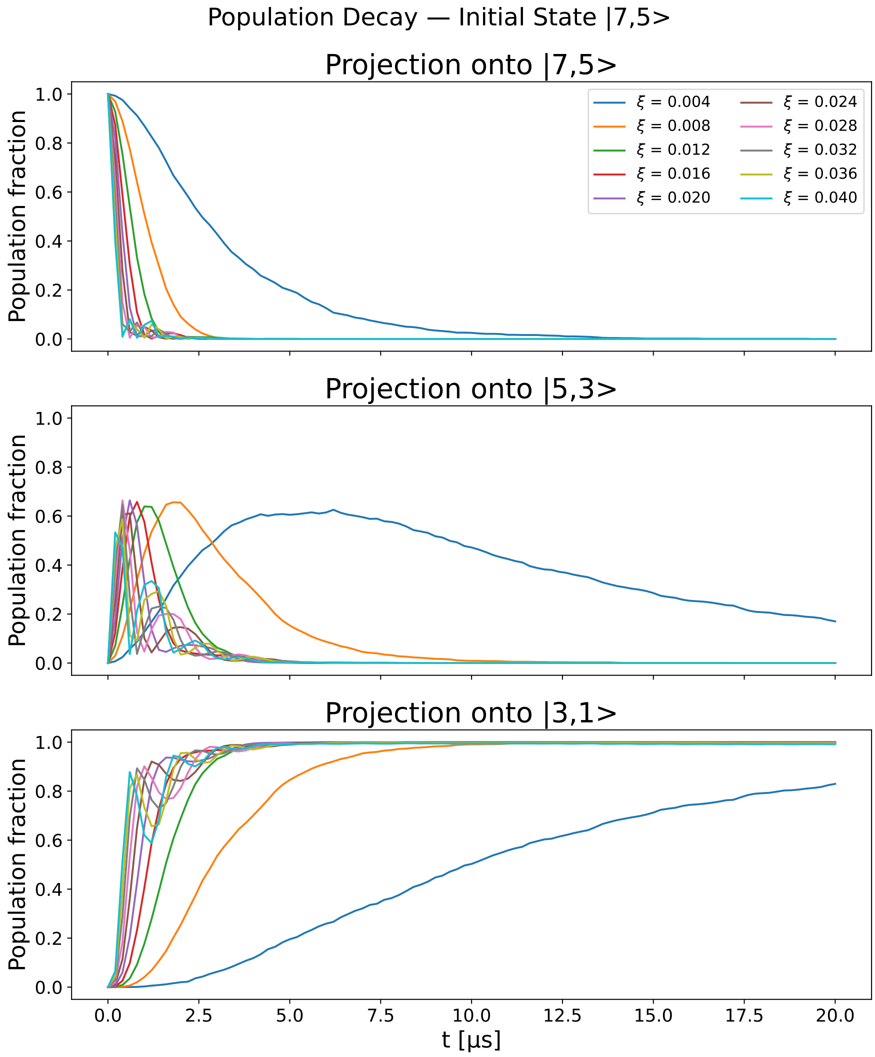

Figure C.15: Population decay of state initialized in $|7,5\rangle$. The decay occurs in two steps, first from $|7,5\rangle$ to $|5,3\rangle$ and then from $|5,3\rangle$ to $|3,1\rangle$. For larger pump strengths do we observe ”kicks” as the population in $|5,3\rangle$ start to repopulate the population in $|7,5\rangle$. For the larger pump strength do we also observe repopulation of $|5,3\rangle$ from $|3,1\rangle$.

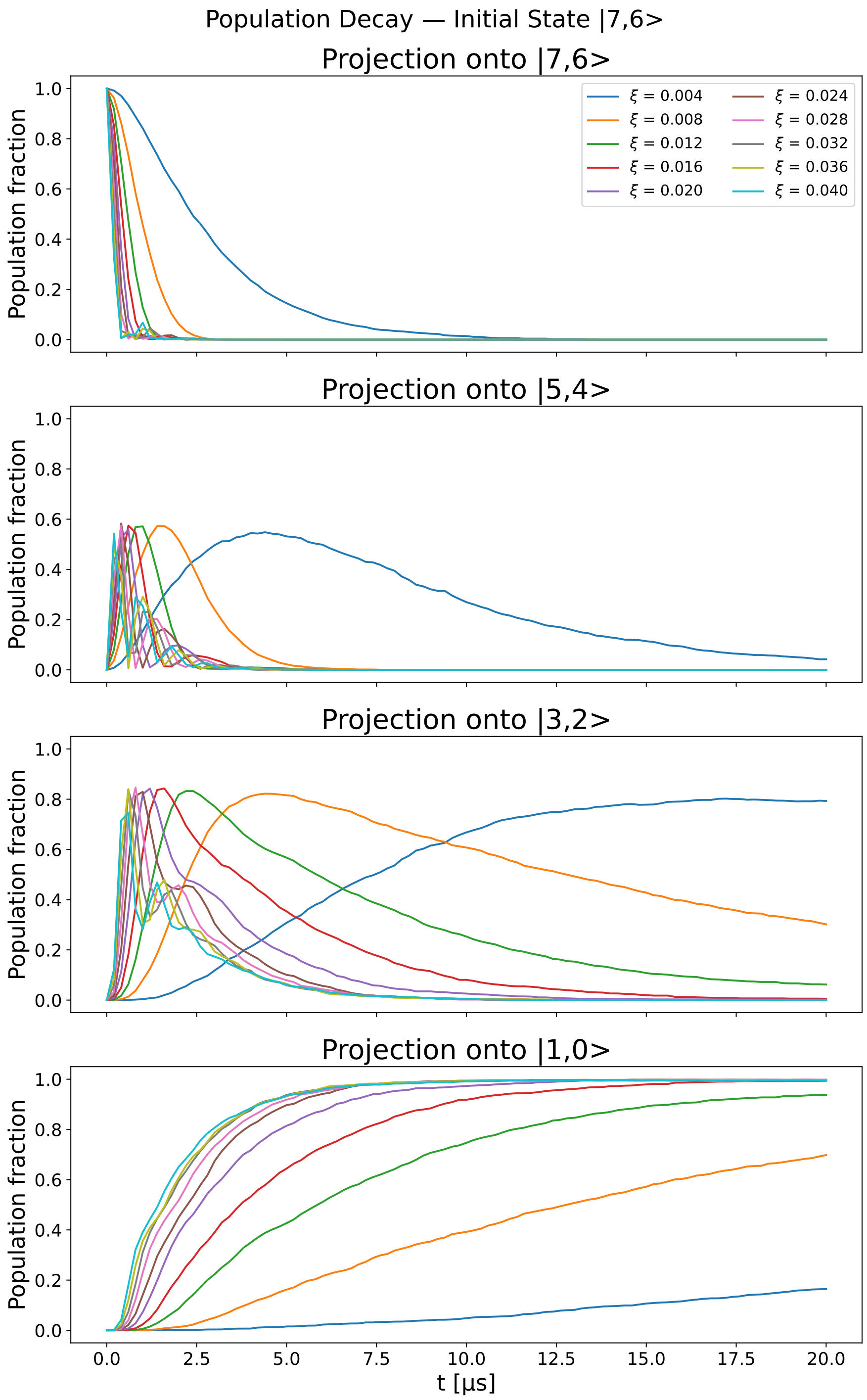

Figure C.16: Population decay of state initialized in $|7,6\rangle$. The decay occurs in three steps, first from $|7,6\rangle$ to $|5,4\rangle$, then from $|5,4\rangle$ to $|3,2\rangle$, and finally from $|3,2\rangle$ to $|1,0\rangle$. For larger pump strengths do we observe "kicks" as the non-vacuum states repopulate. The repopulation for state $|7,6\rangle$ is negligible in comparison to the repopulation of $|5,4\rangle$ and $|3,2\rangle$. The repopulation of $|3,2\rangle$ is a consequence of the repopulation of $|5,4\rangle$ as no kicks can be observed in the projection of $|1,0\rangle$.

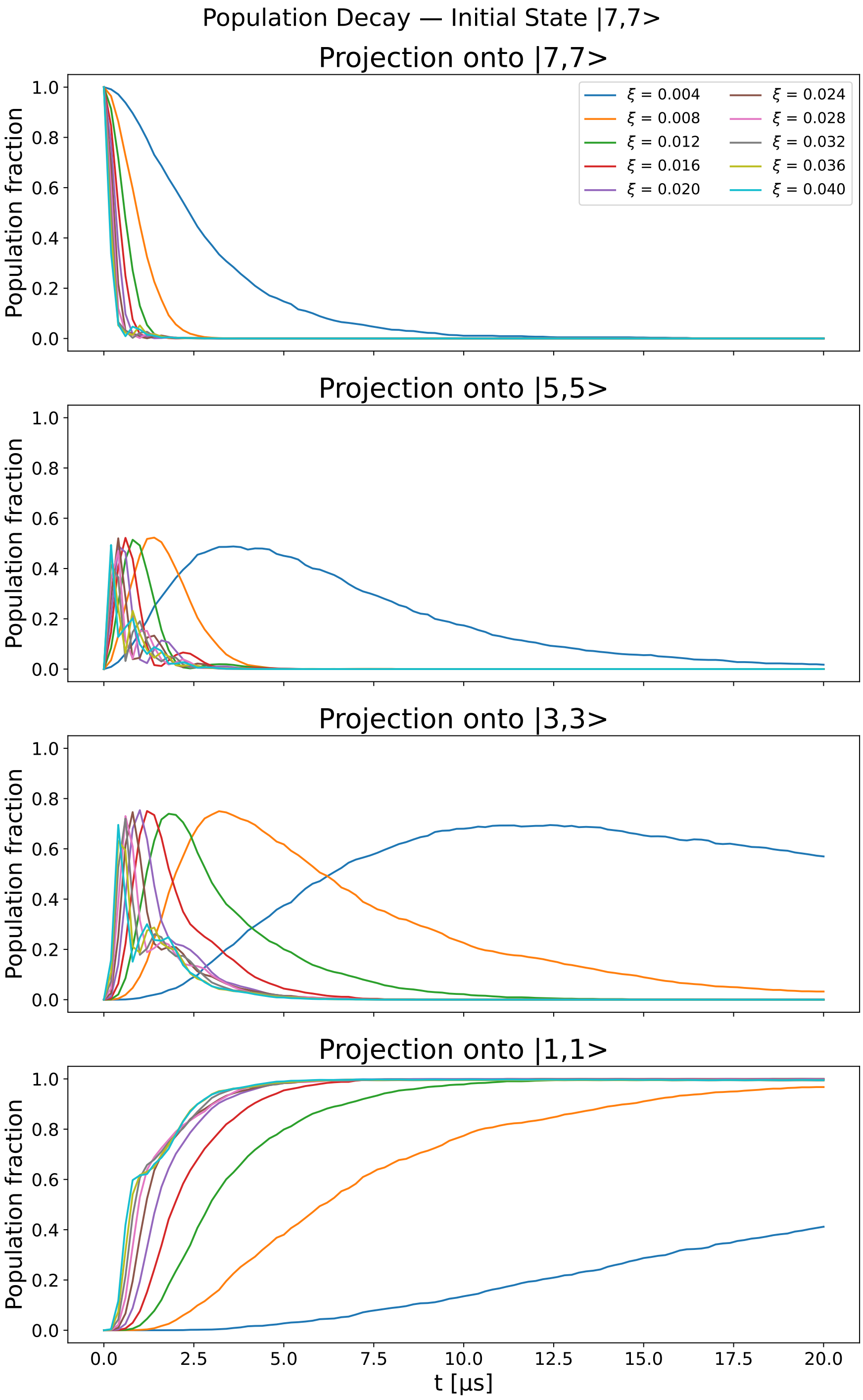

Figure C.17: Population decay of state initialized in $|7,7\rangle$. The decay occurs in three steps, first from $|7,7\rangle$ to $|5,5\rangle$, then from $|5,5\rangle$ to $|3,3\rangle$, and finally from $|3,3\rangle$ to $|1,1\rangle$. For larger pump strengths do we observe "kicks" as the non-vacuum states repopulate. The repopulation for state $|7,7\rangle$ is negligible in comparison to the repopulation of $|5,5\rangle$ and $|3,3\rangle$. The repopulation of $|3,3\rangle$ is a consequence of both the repopulation of $|5,5\rangle$ and repopulation kicks from $|1,1\rangle$.

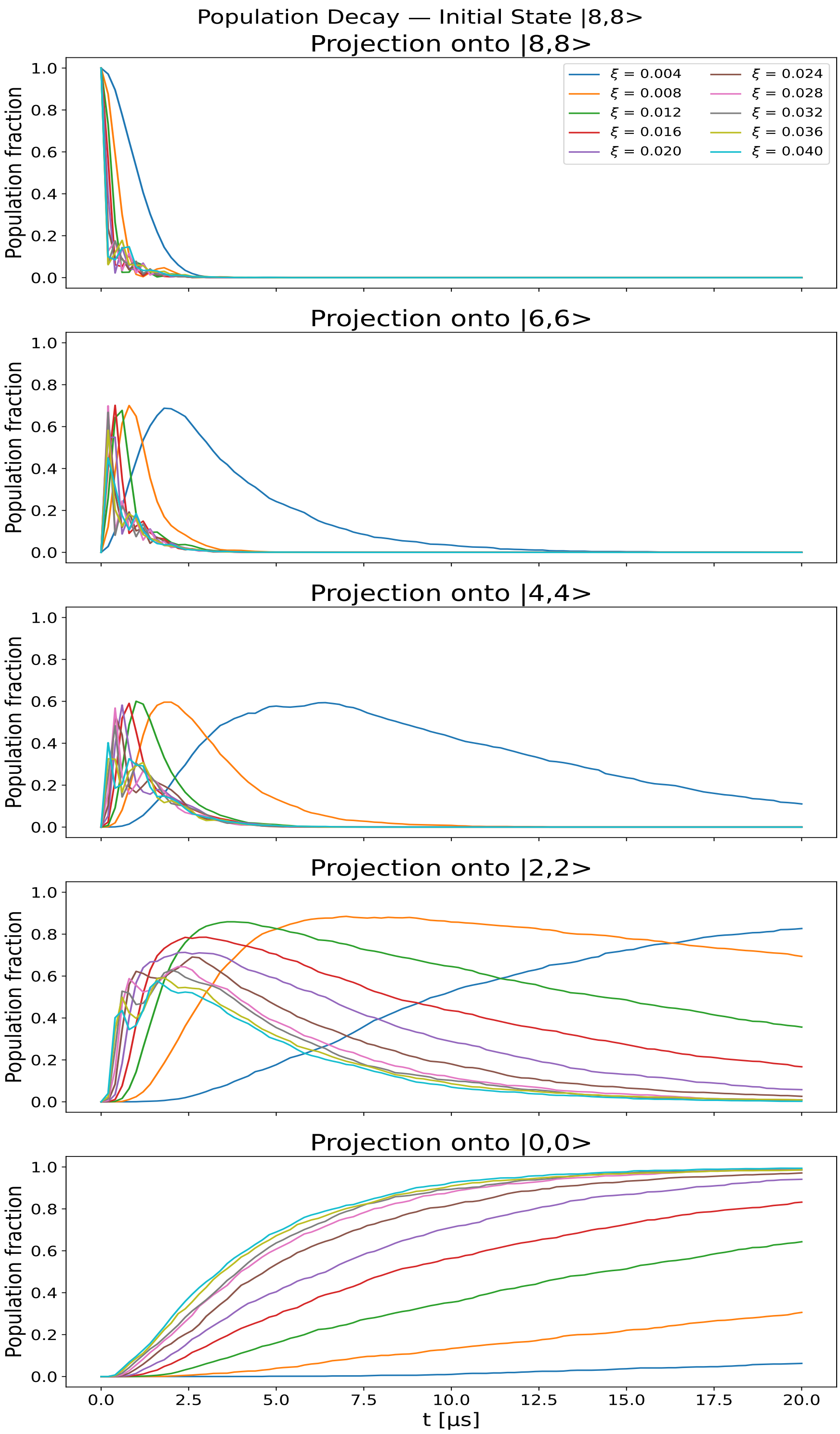

Figure C.18: Population decay of state initialized in $|8,8\rangle$. The decay occurs in four steps, first from $|8,8\rangle$ to $|6,6\rangle$, then from $|6,6\rangle$ to $|4,4\rangle$, and from $|4,4\rangle$ to $|2,2\rangle$. Finally the $|2,2\rangle$ state decays to the $|0,0\rangle$ state. For larger pump strengths do we observe "kicks" as the non-vacuum states repopulate. The largest repopulation occurs for $|4,4\rangle$ as photons a part of the population of $|2,2\rangle$ becomes $|4,4\rangle$, which in turn repopulate $|2,2\rangle$.

DEPARTMENT OF SOME SUBJECT OR TECHNOLOGY
CHALMERS UNIVERSITY OF TECHNOLOGY
Gothenburg, Sweden
www.chalmers.se

CHALMERS
UNIVERSITY OF TECHNOLOGY